AERODYNAMIC DESIGN FOR SWEPT-WING LAMINAR FLOW

A Dissertation

by

MICHAEL JOSEPH BELISLE

Submitted to the Office of Graduate and Professional Studies of
Texas A&M University
in partial fulfillment of the requirements for the degree of

DOCTOR OF PHILOSOPHY

Chair of Committee,   William S. Saric
Committee Members,   Helen L. Reed
    Edward B. White
    Rodney D. W. Bowersox
    Devesh Ranjan
Head of Department,   Rodney D. W. Bowersox

December 2013

Major Subject: Aerospace Engineering

ABSTRACT

This work describes and compares processes for swept-wing laminar flow control (SWLFC) aerodynamic design. It focuses on results obtained during the preliminary outer-mold-line (OML) design of the Subsonic Aircraft Roughness Glove Experiment (SARGE), a natural laminar flow and passive laminar flow control wing glove flight experiment funded by the NASA Environmentally Responsible Aviation initiative. The experiment seeks to raise the technology readiness level of the spanwise-periodic discrete roughness element (DRE) SWLFC technique for transition delay on a swept wing.

Changes to the SARGE project requirements necessitated numerous redesigns that lead to design process insights and reinforced the value of proven methodologies. Optimization-based wing design methods are compared to traditional processes in the context of issues specific to SWLFC design. A refined traditional process incorporates the lessons learned during SARGE design excursions. As 3D effects are often significant at transonic Mach numbers, they should be included in the analysis as soon as practical when allowing for available computational tools.

In the initial experimental feasibility and OML design, Euler computational fluid dynamics was used to produce a series of 2.5D SWLFC airfoils with boundary-layer stability and transition predicted using linear stability theory and the e^N method. Two wing gloves were lofted onto the Gulfstream-III host aircraft wing: TAMU-05-04, a straight loft using the TAMU2D-04 airfoils, and TAMU-06-05, an optimized revision used in the preliminary design review (PDR) of the SARGE experiment conducted in June 2012. The target pressure distribution for the TAMU-06-05 glove was developed using a graphical B-spline method.

The SARGE PDR identified a few issues that need to be addressed in order to ensure a successful experiment, which includes isobar unsweep that adversely affects boundary layer stability for DRE control and potential flow separation at the inboard fairing. Using the refined process, an alternate planform is evaluated as a potential starting point to address these issues and is shown to be feasible.

ACKNOWLEDGMENTS

TABLE OF CONTENTS

LIST OF FIGURES

viii

LIST OF TABLES

NOMENCLATURE

Abbreviations and acronyms

2D	Two dimensional
2.5D	2D analysis with plane-normal velocity component
3D	Three dimensional
AEI	Aerodynamic Efficiency Improvement (AFRL/NGC)
AFRL	Air Force Research Laboratory
ATTAS	Advanced Technologies Testing Aircraft System (German Aerospace Center)
BL	Wing buttock line, measured in inches from aircraft centerline
CAD	Computer-aided design
CC	Complex conjugate
CFD	Computational fluid dynamics
CST	Class-shape transformation
DBL	Direct boundary layer
DDI	Direct Dimensions, Inc.
DFRC	Dryden Flight Research Center (NASA)
DNS	Direct numerical simulations
DOC	Direct operating costs
DRE	Discrete roughness element
DRELFGE	Discrete Roughness Elements Laminar Flow Glove Experiment
ELFIN	European Laminar Flow Investigation
ERA	Environmentally Responsible Aviation
FRL	Flight Research Laboratory (TAMU)
HLFC	Hybrid laminar flow control
KCAS	Knots calibrated airspeed
LaRC	Langley Research Center (NASA)
LFC	Laminar flow control
LST	Linear stability theory
MFR	Mass flow ratio
NASA	National Aeronautics and Space Administration
NGC	Northrop Grumman Corporation
NLF	Natural laminar flow
OML	Outer mold line
PDR	Preliminary design review
PSE	Parabolized stability equations

RMS	Root-mean-square
SARGE	Subsonic Aircraft Roughness Glove Experiment
SCRAT	Subsonic Research Aircraft Testbed
SWIFT	Swept-Wing In-Flight Testing (AFRL/TAMU)
SWLFC	Swept-wing laminar flow control
TAMU	Texas A&M University
TRL	Technology readiness level
TS	Tollmien–Schlichting–Schubauer–Skramstad
VSTFE	Variable Sweep Transition Flight Experiment

Greek symbols

α	Chordwise wavenumber
β	Spanwise wavenumber
Δ	Grid connector spacing constraint
δ_f	Flap deformation in degrees
ε	Thickness ratio of equivalent ellipse
Λ	Sweep angle
λ	Dimensional disturbance wavelength
λ_w	Wing taper ratio, $\lambda_w = c_r/c_t$
λ_1	Control or "killer" wavelength for transition delay using DREs
λ_2	Most-unstable or "target" wavelength for transition delay using DREs
μ	Dynamic viscosity
v	Kinematic viscosity, $v = \mu/\rho$
ϕ	Orr-Sommerfeld disturbance eigenvector, $\phi = v(y)$
Φ	Velocity potential, where $\mathbf{Q} = \nabla \Phi$
ρ	Density
τ_w	Wall shear stress
Θ	Disturbance phase function
θ	Boundary layer momentum thickness
ω	Circular wave frequency
ψ	Angle of wave vector with respect to inviscid streamline

Roman symbols

A	Wave amplitude
AoA	Angle of attack
AoY	Angle of yaw
$\mathcal{R}$	Aspect ratio, $\mathcal{R} = b^2/S$
b	Wing span
c	Wing chord

C_L	Overall lift coefficient, $C_L = L/(qS)$
C_p	Pressure coefficient, $C_p = 2(p/p_\infty - 1)/(\gamma M_\infty^2)$
C_{p_0}	Incompressible pressure coefficient
c_r	Wing root chord
c_t	Wing tip chord
D	Derivative with respect to y, $D = d/dy$
f	Wave frequency (dimensional)
h	Roughness height
k	Total wavenumber, $k^2 = \alpha^2 + \beta^2$
$\mathscr{L}$	Orr-Sommerfeld operator defined in §I.1 (page 7)
l^*	Boundary-layer length scale, $l^* = \sqrt{(v^* x^*)/U_e^*}$
M	Mach number
MAC	Mean aerodynamic chord
N	Smith–van-Ingen N-factor
n	Number of grid nodes on a connector or domain
p_q	Dynamic pressure
p_s	Static pressure
p_T	Total pressure
$\mathbf{Q}$	Velocity vector in global coordinate system
Q	Velocity magnitude
q	Generic flow variable (e.g. u, p) total disturbance or disturbance amplitude per context
Re_c	Reynolds number using chord as characteristic length, $Re_c = \rho U c/\mu$
Re'	Unit Reynolds number (Re_c/c)
Re_θ	Attachment-line momentum thickness Reynolds number
Re_x	Reynolds number using x distance along surface as characteristic length, $Re_x = \rho U x/\mu$
r_{LE}	Leading-edge nose radius (perpendicular to leading edge)
R_q	RMS surface roughness
R_t	Peak-to-peak surface roughness
S	Theoretical planform wing area
T	Total engine thrust
t	Wing thickness
t/c	Wing (airfoil) thickness ratio
T/W	Thrust-to-weight ratio
U, V, W	X, Y, and Z components of velocity, respectively
u, v, w	Local boundary-layer velocity components: u, chordwise; v, normal to surface; w,

	spanwise along surface
v	Velocity vector in boundary-layer coordinates
W	Aircraft weight
W/S	Wing loading
X, Y, Z	Global coordinate system with origin at fuselage nose: *X*, along fuselage centerline; *Y*, along wing span; *Z*, normal to fuselage centerline and wing span
x, y, z	Local surface coordinate system: *x*, normal to leading edge along surface; *y*, normal to surface; *z*, parallel to leading edge along surface
x_t, y_t, z_t	Streamline coordinate system: x_t along stream in direction of flow, y_t normal to stream perpendicular to surface, z_t perpendicular to stream along surface

Subscripts

o	Reference value, typically at neutral stability point
AL	Attachment line
crit	Critical value above which flow is locally supersonic
e	Boundary-layer edge value (in surface local coordinate system)
LE	Leading edge
r, i	Real and imaginary parts (respectively) of a complex variable
t	Boundary-layer value (in streamline coordinate system)
tr	Value at transtion
∞	Freestream value (in global coordinate system)

Superscripts

*	Dimensional quantity
‾	Meanflow quantity
′	Disturbance quantity

CHAPTER I

INTRODUCTION

In the external flow past a fixed-wing aircraft, the effects of friction and viscosity are essentially confined to the thin boundary-layer region near to the aircraft surface. Within the boundary layer, the flow can be essentially classified into two regimes: laminar and turbulent.

The flow past a flat plate parallel to the freestream illustrates the basic process. Assuming the freestream turbulence levels are sufficiently low and the flat plate sufficiently flat (Saric 2008*a*), the boundary layer on the plate will first appear as laminar. Small disturbances, initiated by freestream quantities such as sound and turbulence, enter the boundary layer through the receptivity process (Saric, Reed & Kerschen 2002). These disturbances may grow or decay in space and time. At some chord location along the plate, inevitably some disturbances will grow sufficiently to initiate the transition-to-turbulence process.

The transition process may follow one of a number of different paths towards turbulence as simplified in Morkovin, Reshotko & Herbert (1994). In the cases of interest to aircraft design, the path to transition will follow the classical path "A" in figure I.1, where the growth of primary modes leads to secondary instabilities, breakdown, and eventually turbulence.

The fact that a laminar layer exerts lower shear stress on the surface than a turbulent layer drives the interest in aerodynamic design for laminar flow. The wall shear stress τ_w is approximated in a two-dimensional (2D) Newtonian fluid flow by

$$\tau_w \approx \mu \left.\frac{\partial u}{\partial y}\right|_{y=0},$$

where μ is the dynamic viscosity, u is the fluid velocity parallel to the surface, y is the coordinate normal to the surface, and normal velocity component v is zero at a non-porous wall. The velocity profile for a 2D laminar boundary layer on a flat plate in zero pressure gradient can be calculated by a similarity solution of the asymptotic boundary-layer equations, as identified by one of L. Prandtl's early students, Blasius (1908). Using the Blasius velocity profile to calculate wall shear stress leads to the following expression for the laminar skin friction coefficient:

$$C_{f,\text{laminar}} = \frac{2\tau_w}{\rho\, U^2} = \frac{0.664}{\sqrt{Re_x}},$$

Forcing environmental disturbances
amplitude — — — — — — — — — →

Receptivity

A   E

Transient growth

B   C   D

Primary modes   Bypass

Secondary mechanisms

Breakdown
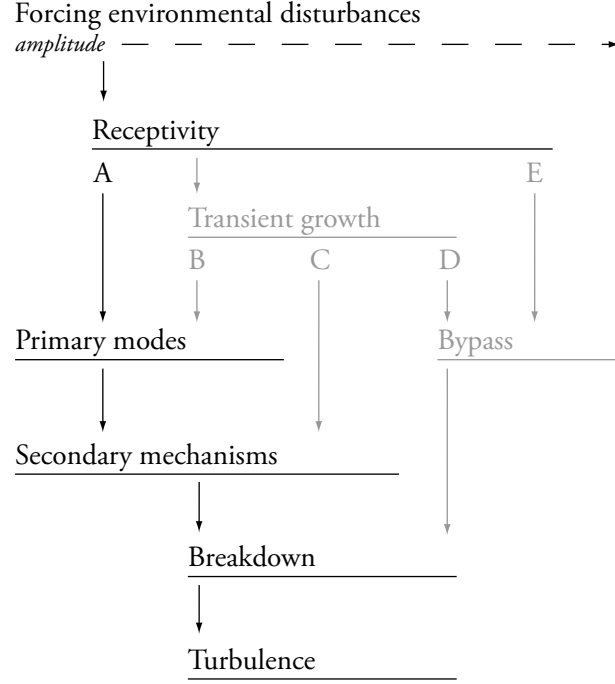
Turbulence

FIGURE I.1. Simplified view of paths to turbulence in wall layers. This dissertation focuses on the highlighted classical path "A" characteristic of transition in the low-disturbance flight environment. Adapted from Morkovin, Reshotko & Herbert (1994).

where

$$Re_x = \frac{\rho U x}{\mu},$$

ρ is the fluid density, U the freestream velocity, and x the distance from the flat plate leading edge. The skin friction coefficient for the turbulent boundary layer can be reasonably approximated using a simple power law (White 2006) due to Prandtl:

$$C_{f,\text{turbulent}} = \frac{0.027}{Re_x^{1/7}}.$$

When integrating these two skin friction coefficients for a flat plate of chord Reynolds number $Re_c = 20 \times 10^6$, similar to a typical Re_c for a small business jet, one arrives at order-of-magnitude reduction in skin friction for a laminar boundary layer when compared to a turbulent one. Hence, it is sometimes common in preliminary analyses to treat laminar drag as negligible in comparison to turbulent drag; in reality, the efficiency depends on the specific case. 90% efficiency is representative for laminar extents achievable on business jet and narrow body jet airliners of interest in this dissertation.

Consider now inclining the flat plate, which imposes a slight increasing (decelerating) pressure

gradient. Due to the effects of this gradient, τ_w will decrease when traversing downstream. In the neighborhood of $\tau_w = 0$, the boundary layer can be assumed to "separate" and a triple-deck structure appears with characteristic recirculation in the region below the separated boundary layer. On an airplane wing, early boundary-layer separation can result in increased drag. In more drastic cases, boundary-layer separation can also lead to aircraft stall with potentially drastic consequences. Laminar flow wing designs are more prone to this sort of separation, leading to use of vortex generators to fix the transition location in some wing designs: an attached, turbulent boundary layer is typically preferable to a separated laminar one.

The goal of this research is to advance the understanding of laminar flow design to towards the elusive realization of practical laminar flow on production aircraft. Despite decades of theoretical, computational, and experimental research into transition delay on aircraft, operational laminar flow aircraft is generally limited to general-aviation-scale aircraft: low sweep, low Reynolds number, low Mach number. Laminar flow efforts to date have largely concentrated on two broad approaches: natural laminar flow (NLF), a passive technique where laminar flow is maintained by tailoring the pressure gradient using geometry shaping; or active laminar flow control (LFC) techniques such as suction and hybrid laminar flow control (HLFC).

In the transonic range where modern medium- to long-range transport aircraft operate, low sweep angles are usually avoided due to increased wave drag. This is especially a concern for larger aircraft where reducing the drag divergence Mach number through thinning the wing is a structural challenge. Strut-braced, high-aspect ratio wings such as those of Pfenninger (1987) may be an option, but could be limited by operational concerns such as ground maneuverability. For active techniques, hardware such as plumbing, bleed air, and compressors necessary for the suction system add a level of complexity to an aircraft design that often fails to survive a cost-benefit analysis to "buy" its way into an operational system.

This work focuses on passive swept wing laminar flow control (SWLFC). SWLFC concerns the application of NLF design to wings having leading wing sweep $\Lambda_{\mathrm{LE}} > 20°$. SWLFC is as attractive alternative when considering the limitations of the prevailing approaches (§I.3.3), but has comparatively lower technology readiness level (TRL) as defined by Sadin, Povinelli & Rosen (1989) and Mankins (1995).

Complicating things further is the fact that many fundamental transition processes remain to be understood. Most basic among these open questions is a universal transition criterion: even in the simplest case on a flat plate, there is still no theory than can predict the location of transition (Saric, Reed & White 2003). SWLFC is more challenging still, due to the three-dimensional nature of the flow and the fundamentally nonlinear behavior of the crossflow instability when it triggers transition.

For industrial applications, empirical methods such as the e^N method of Smith & Gamberoni (1956) and Van Ingen (1956) facilitate practical transition estimation in the design stage as long as the correlation is applied in a relevant environment. The technique is reliable for 2D boundary layers,

but not necessarily 3D boundary layers (Reed, Saric & Arnal 1996).

A thoroughly complete of understanding of the physical processes is not necessarily a prerequisite for successful operational application. This is an industry view enthusiastically stated by J. Szodruch, then General Manager for Research & Technology at Airbus Industrie, in his welcome address to the First European Forum on Laminar Flow Control:

> Transition is still an extremely complex phenomena and we know little about it. I think I am right in saying that almost 110 years after the Reynolds experiment, the exact cause of transition in that pipe flow experiment still lacks an explanation. Now, the scientific view is different from the engineering view. Sometimes we don't know why something works but we still apply it—successfully! (Szodruch 1992)

Provided that the obstacles can be overcome and a means to robustly and routinely delay transition achieved in an operational aircraft design, extensive laminar flow promises the single greatest potential for fuel economy increases through airframe technology improvements potentially achievable in the near-term(Green 2008; Collier 2010). In the Piaggio P-180 turboprop aircraft, for example, designing for NLF on the wing increased aerodynamic efficiency by an estimated 10% (Sacco & Piaggio 1996). For medium- to long-range, high-subsonic transports such as a Boeing 737 or 757, applying laminar flow to the wings could translate to similar fuel savings on the order of 5–10% during cruise. A reduction of this magnitude leads to significant reductions in direct operating costs (DOC) for an airline fleet. Robert (1992) calculated that for an airline fleet in the 1990s, a 1% reduction in fleet DOC represents a savings of several million dollars per year. Fuel costs have risen significantly since the 1990s, making the potential gain even more attractive today. When considering the technology cost, Robert (1992) suggests that in the extreme case, up to a 10% reduction in fuel savings may be necessary to cancel out the implementation cost.

Obara & Holmes (1985), Arcara Jr, Bartlett & McCullers (1991), and Robert (1992) estimate that these total drag reductions on the order of 5%–10% are practically achievable as demonstrated by a simple order–of-magnitude drag buildup. On a conventional wing-body-tail transport aircraft, skin friction is responsible for about one-half of the total drag. Induced drag, interference, and other types of drag make up the other half. The primary concern in this research is drag reduction on the wings, which is typically responsible for half of the skin friction drag (one-quarter of the total drag). When considering that laminar drag is about one-tenth that of turbulent drag, a practical estimate of 60%-chord laminar flow on the both the suction (upper) side and 30%-chord laminar flow on the pressure (lower) side of the wing results in an 8% savings in total drag.[*]

This simple analysis considers laminar flow when applied to an existing turbulent configuration. When the design is optimized for laminar flow, the potential savings can be even larger. Assuming

---

[*]Assumptions in this estimate include approximately 90% efficiency for laminar flow and an empirical 80% "crud" factor (Feagin & Morrison 1978) for regions where laminar flow is impractical (e.g. very near the wing tips, fuselage, or from wedges due to the presence of any wing-mounted engines or stores).

laminar flow to meet mission objectives in a design requires a means for transition delay with proven reliability, which in part depends on development of modern design methodologies that increase use of physics-based calculations in design. This dissertation describes one such approach to passive SWLFC aerodynamic design as applied to the wing glove design in a transonic flight experiment that seeks to push SWLFC technology beyond the limits previously demonstrated.

I.1. Linear stability theory

Design for laminar flow requires an appreciation of the linear stability theory (LST) used to calculate the primary stability characteristics of a boundary layer. The development here follows from Mack (1984) and Saric (2008b). Reed, Saric & Arnal (1996) review recent linear results, with particular emphasis on the appropriate application and limitations of linear stability theory as it applies to boundary-layer flows. In this high-level overview, the fluid is viscous, incompressible, and described using Cartesian coordinates. The incompressible theory covers the basic ideas needed to grasp the concepts of laminar flow design using LST, although the calculations in this dissertation are carried out using the viscous, compressible, heat-conducting formulation of LASTRAC (Chang 2003, 2004). Details of the compressible theory may be found in Mack (1984; chapter 9).

LST starts from a steady, unperturbed solution of the nondimensional Navier–Stokes equations ("basic state"):

$$\nabla \cdot \mathbf{v} = 0$$
$$(\mathbf{v} \cdot \nabla)\,\mathbf{v} = -\nabla p + \frac{1}{Re}\nabla^2\mathbf{v}.$$

Here, $\mathbf{v}$ is the velocity vector in boundary-layer coordinates (x^* chordwise along the surface, y^* normal to the surface, and z^* spanwise), p is the pressure, and $Re = \rho^* U_e^* l^*/\mu^*$ is the Reynolds number defined by the of the kinematic viscosity v^*, length scale l^*, and boundary-layer edge velocity U_e^*. In the boundary-layer approximation, $\partial p/\partial y \approx 0$. The length scale does not necessarily need to be specified at this time, although it typically taken as $l^* = \sqrt{v^* x^*/U_\infty^*}$ in boundary-layer calculations. An asterisk denotes dimensional quantities; all other quantities are nondimensional.

In this local formulation, curvature effects are neglected. This is typical of the LST, since including curvature would require inclusion of other terms that are of similar order, such as non-parallel effects. The consequences of including or excluding curvature from the computation has been investigated by numerous authors, including Lin & Reed (1993) Malik & Balakumar (1993), and reviewed by Saric *et al.* (2003). The basic state is assumed to be quasi-parallel; that is, the growth of the boundary layer over a disturbance wavelength λ is small.

The approach in LST superposes small disturbances on basic state to determine if they grow or decay in space ("spatial stability"). If all the perturbations decay, then the flow is termed stable. If at least one perturbation grows, then the flow is unstable. The objective in laminar flow design is to move the flow

towards a more stable state such that transition is delayed to a chord position aft of its "natural" or uncontrolled location. While the crossflow instability on a swept wing exhibits nonlinear phenomena (see §I.2.4), the computational expense of nonlinear computations necessitate that laminar-flow design primarily employ LST computations. Some caveats about the limits of the LST approach are described in §III.1.3.

For many practical applications these assumptions are valid. When they are not valid, or as a check on the design, the parabolized stability equations (PSE; Bertolotti, Herbert & Spalart 1992; Bertolotti & Herbert 1991; Herbert 1997; Haynes & Reed 2000) include nonparallel and curvature effects, as well as the capability to include nonlinear effects as well.

The quasi-parallel local flow is described by

$$u = u(y), \quad v = 0, \quad w = w(y), \quad T = T(y).$$

The disturbances are superposed on the basic state using total disturbances of the form

$$q(x, y, z, t) = \bar{q}(y) + q'(x, y, z, t)$$

where q is a generic flow quantity (i.e., a velocity component or pressure), an overbar indicates the meanflow quantity, prime denotes the typically weak, superposed disturbance. Seperately, q and $\bar{q}$ satisfy the complete Navier–Stokes equations while the disturbance quantities q' do not. When substituting the total disturbance into the Navier–Stokes equations, the basic state vanishes identically leaving only the disturbance equations. In LST, the equations are linearized by neglecting products of disturbances.

The linear disturbance equations have coefficients that are functions of y only. It is possible to solve the equations by separation of variables through the use of normal modes:

$$q' = q(y)e^{i\Theta} + \text{CC},$$

where q is now the amplitude of the disturbance, CC stands for complex conjugate, and $\Theta(x, z, t)$ is a generic phase function whose derivatives

$$\frac{\partial \Theta}{\partial x} = \alpha, \qquad \frac{\partial \Theta}{\partial z} = \beta, \qquad \frac{\partial \Theta}{\partial t} = -\omega$$

give the chordwise wavenumber α, spanwise wavenumber β, and frequency ω. Since the quasi-parallel assumption neglects variations in disturbances and boundary layer length scale with x, the normal mode may be simplified to

$$q' = q_0(y)e^{i(\alpha x + \beta z - \omega t)} + \text{CC}$$

Substitution of this normal mode into the disturbance equations results in the Orr-Sommerfeld equation $\mathscr{L}(\phi)$ derived independently by Orr (1907) and Sommerfeld (1908) (after considerable

manipulation):

$$\mathscr{L}(\phi) = (D^2 - k^2)^2 \phi - iR\left[(\alpha U_e + \beta W_e - \omega)(D^2 - k^2)\phi - (\alpha D^2 U_e + \beta D^2 W_e)\phi\right] = 0$$

with boundary conditions

$$\phi(0) = D\phi(0) = 0$$
$$\phi(y \to \infty) \to 0$$

and where $\phi = v$, $D = d/dy$, and $k^2 = \alpha^2 + \beta^2$.

The growth rates are computed at each chordwise station and integrated over a specified interval $x = [x_0, x_1]$ in order to determine the total growth. Generally, the spanwise growth β_i is an unknown. If the flow is essentially spanwise uniform as assumed in this document, then $\beta_i \approx 0$. The Smith–van-Ingen N-factor is the total amplification for a particular wave from location x_0 to x_1:

$$N = \ln\left(\frac{A}{A_0}\right) = \int_{x_0}^{x_1} \sigma dx$$

where $\sigma = -\alpha_i$ is the disturbance growth rate and A/A_0 is the ratio of the final and initial disturbance amplitudes. Various strategies for the integration of the N-factor exist as described in Arnal, Casalis & Houdeville (2008a). The method employed here is the "envelope of envelopes" method, where the integrations are performed by tracking the growth of waves with a given dimensional frequency f, and a constant value of β, λ, or ψ (where ψ is the wave angle of the wave vector with respect to the inviscid streamline). This method differs from the computationally cheaper "envelope" method, which integrates the growth of the most unstable disturbance at each location. The envelope method typically results in unphysically high N-factors, although it commonly implemented for transition prediction in rapid design codes such as XFOIL (Drela 1989) because of the speed and simplicity of the computation. Transition estimates from such codes should be used with discretion except in the simplest cases.

I.2. Swept-wing instability mechanisms

Modern high-subsonic transport aircraft typically have wings sweeps in the range $\Lambda_{\mathrm{LE}} \approx [25°, 35°]$ in order to reduce wave drag at transonic speeds. At these sweep angles, the boundary layer is three-dimensional, characterized by a crossflow velocity component normal to the inviscid streamline. Saric & Reed (2004) discuss the many practical challenges that remain for passive SWLFC to be applied to operational aircraft.

Four basic types of instabilities have been identified for three-dimensional flow on a swept wing: attachment line, streamwise, centrifugal, and crossflow (Saric *et al.* 2003). Engineering application and control of the first three mechanisms are sufficiently well understood such that they do not present
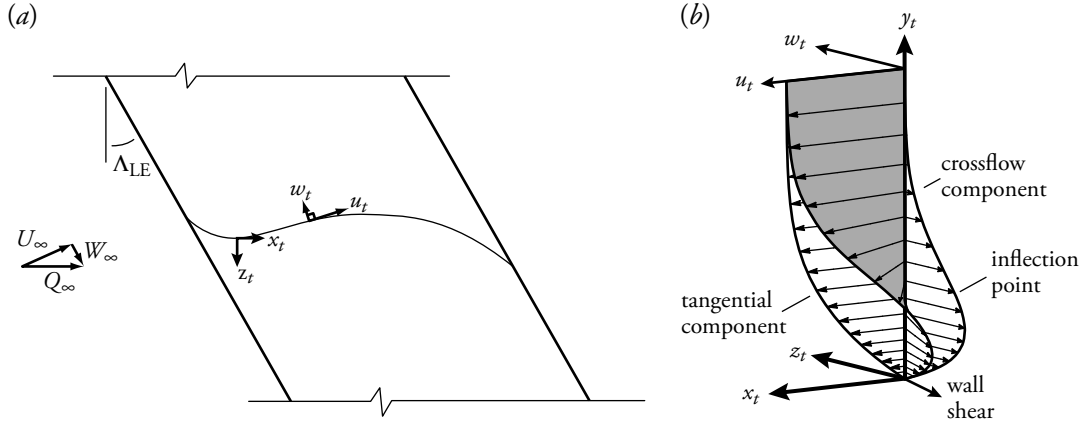
FIGURE I.2. (*a*) Swept wing inviscid streamline (after Reed & Saric 1989) and (*b*) 3D boundary-layer profile in a swept-wing flow (after Saric *et al.* 2003). Not to scale.

a significant obstacle to SWLFC (Joslin 1998). For wings of relatively low sweep, i.e. approximately $\Lambda_{LE} \leq 20°$, crossflow is not an issue. For wings of higher sweep, the presence of crossflow necessitates design compromises to adequately control all of these sometimes competing instabilities.

In the inviscid region of a swept-wing flow, the combination of sweep and pressure gradient deflects the streamlines at the boundary-layer edge as shown in figure I.2(*a*). Inside the boundary layer, the streamwise velocity is reduced, but the pressure is unchanged (following from the approximation $dp/dy \approx 0$). The balance between centripetal acceleration and pressure gradient in the inviscid region does not exist inside the boundary layer, producing the crossflow profile in figure I.2(*b*).

For the streamwise velocity profile, the flow velocity u_t is zero at the wall and accelerates to the edge value U_e at the boundary-layer edge, resulting in stability behavior analogous to the TS wave in the 2D case (where TS stands for Tollmien 1931, 1936; Schlichting 1932, 1933, 1950*a,b*; Schubauer & Skramstad 1948).

The crossflow velocity profile is characteristically different. For crossflow, the flow velocity w_t is zero at both the wall and at the freestream. Additionally, the derivative w_t' is zero at the boundary edge in order to merge smoothly with the freestream. These boundary conditions requires an inflection point, the source of an invsicid stability that differs fundamentally from the viscous streamwise instability.

Control of the stationary crossflow instability poses the greatest challenge to practical SWLFC on transport aircraft (Saric & Reed 2004). In general, attachment line and curvature instabilities are controllable using well-established design strategies. The streamwise instability is controllable by imposing a favorable pressure gradient $dp/dx < 0$. Unfortunately, a favorable gradient has a destabilizing effect on crossflow. The SWLFC technique studied here represents a compromise where a favorable pressure gradient is used to stabilize the streamwise instability while the inherent destabilization of crossflow is mitigated using the discrete roughness element (DRE) technique described

in §I.3.3.

I.2.1. *Curvature instability*

The shear flow over a concave surface is subject to a centrifugal instability known as the Görtler instability (Saric 1994). In the case of a wing, concave geometry is most commonly employed near the trailing edge on the pressure side. Since the interest here is to obtain laminar flow to at most $(x/c)_{tr} = 0.60$, presence of the instability in this region should not be a concern.

Some airfoils, like the Pfenninger airfoil (after Pfenninger, Reed & Dagenhart 1979) shown in figure I.3, may have concave geometry near the leading edge. For a swept wing having $\Lambda_{LE} \geq 20°$, appreciable crossflow is present and theoretical and experimental results (Hall 1985; Bassom & Hall 1991; Peerhossaini, Bippes & Steinbach 1990) show that crossflow is the dominant instability. Therefore, curvature instability is not expected to be a concern for the sweep angles $\Lambda_{LE} \geq 30°$ under consideration in this dissertation which have only slight concave curvature, if any at all.

FIGURE I.3. TAMU-002T-80 airfoil cross-section. Concave curvature near leading edge, in addition to the trailing edge, is a characteristic of a Pfenninger airfoil.

I.2.2. *Attachment-line instability*

The attachment line is part of the dividing stream surface that splits the flow over the upper and lower surfaces of a swept wing, diagrammed in figure I.4 from (Poll 1979). The attachment line flow is analogous to the stagnation point in a 2D Hiemenz flow past a cylinder orientated with its longitudinal axis normal to the freestream. The flow along the attachment line is solely in the span direction. For an infinite swept wing ("2.5D", a 2D analysis with plane-normal component of velocity)at zero angle of attack with free-stream velocity Q_∞, the inviscid velocity along the attachment line is $W_\infty = Q_\infty \sin\Lambda_{LE}$.

On a laminar-flow wing, there are two means through which the presence of turbulent flow in the attachment-line flow may prevent laminar flow elsewhere on the wing (Reed & Saric 1989; Arnal, Perraud & Séraudie 2008*b*):

1. Attachment line contamination, where turbulent disturbances from sources such as the wing-fuselage junction propagate along the attachment line; or
2. Attachment-line instability, where the attachment line may transition due to instability of the underlying flow.

9
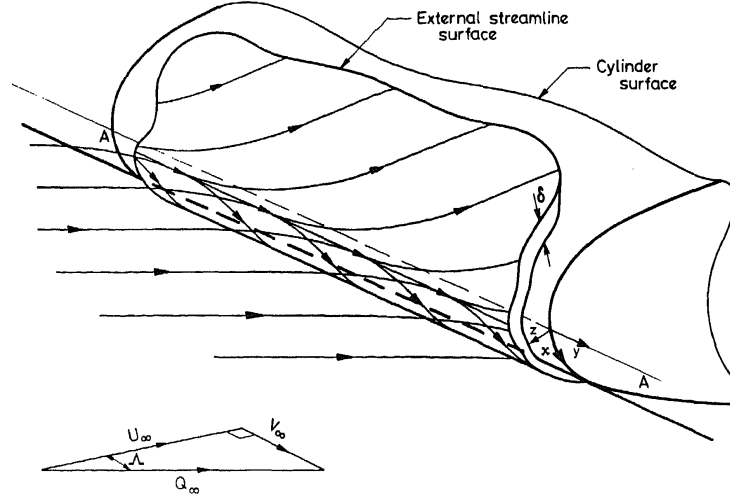
FIGURE I.4. Schematic of flow along the attachment line of a swept wing (Poll 1979; reproduced by kind permission of The Royal Aeronautical Society's *Aeronautical Journal*).

Attachment-line contamination was first observed by Gray (1952) in flight tests of the AW52 laminar flow flying wing aircraft. Pfenninger (1965*a*), who also observed attachment-line transition on the X-21A wing, described the means through which disturbances propagate along the attachment line and suggested strategies for suppression: either by increased suction, decreasing the sweep angle Λ_{LE} or local velocity magnitude W, or by limiting the leading-edge radius r_{LE}.

The stability of the flow along the attachment line is typically correlated using the momentum thickness Reynolds number Re_θ,

$$Re_\theta = \frac{W\theta_{\text{AL}}}{\nu},$$

where W is the local velocity component along the attachment line,

$$\theta_{\text{AL}} = \int_0^\infty \frac{\rho}{\rho_e} \frac{u}{U}\left(1 - \frac{u}{U}\right) dy \quad \text{(White 2006)}$$

is the momentum loss due to the attachment line boundary layer.

Since the velocity profile in the boundary layer may not be known a priori during in the design phase, simplified means for calculating Re_θ have been proposed by a number of authors. This dissertation most commonly uses the approximation of Pfenninger (1965*a*) derived from the potential flow about an "equivalent" ellipse of thickness ratio ε,

$$Re_\theta \approx 0.404 \sqrt{\frac{r_{\text{LE}} Q_\infty \sin^2\Lambda_{\text{LE}}}{(1 + \varepsilon)\nu\cos\Lambda_{\text{LE}}}}.$$

The thickness ratio is conservatively taken to be $\varepsilon = 0$. Cumpsty & Head (1967) and Poll (1979) proposed other approximations, which are typically more cumbersome to calculate. The methods in this dissertation also allow calculation of Re_θ directly using the boundary layer profile along the attachment line.

Pfenninger (1965a) found that for $Re_\theta < 100$, relaminarization of a turbulent attachment line occurs. For an initially laminar attachment-line flow, then Poll (1979) found that propagation of disturbances along the attachment line does not occur for $Re_\theta < 250$. Constraining r_{LE} such that $Re_\theta < 100$ is a conservative approach that addresses both the contamination and the stability problem.

Gaster (1967) demonstrated another means of preventing propagation of disturbances from the wing-fuselage junction through use of a "Gaster bump," a protuberance on the attachment line that forms a stagnation point through which disturbances are unable to propagate. Use of a Gaster bump technically permits the larger $Re_\theta < 250$ constraint to be employed even for a wing joined to a fuselage. Alternatively, the design can incorporate a passive suction patch that bleeds momentum from the attachment line, another technique patented by Gaster (2009).

I.2.3. *Streamwise instability*

The streamwise instability is a viscous instability, sensitive to pressure gradient, freestream sound, and 2D excrescences. In contrast to crossflow, it is relatively insensitive to 3D surface roughness and freestream turbulence. The instability is characterized by 2D waves (propagating approximately normal to the leading edge) as well as 3D waves. The receptivity process generates the initial conditions for these waves. At transonic Mach numbers, some care is necessary in the computation to separate 3D TS from traveling crossflow in order to consistently track one or the other, as there is not necessarily a clear value of ψ that delineates one from the other, as noted by Mack (1979), Malik, Liao, Lee-Rausch, Li, Choudhari & Chang (2011), and Roberts, Reed & Saric (2012). Taking $\psi = 0$ seems to be a popular choice, as is assuming that disturbances propagate in the direction of the local velocity vector (i.e. $\beta = 0$) as typically carried out in this work.

The approach in controlling streamwise instability emphasizes maintaining a favorable pressure gradient as far aft along the wing chord as possible. Furthermore, the design should be substantially limit TS growth rather than be marginal to TS. The growth of TS disturbances can be readily calculated using LST and the expected transition location correlated effectively using the e^N method of Smith & Gamberoni (1956) and Van Ingen (1956).

I.2.4. *Crossflow instability*

The crossflow instability is an inviscid instability that occurs on a swept wing in regions of strong, favorable pressure gradient when there is an inflection point in the boundary layer profile. When nonlinearly saturated, the crossflow instability produces the co-rotating vortex structure shown in
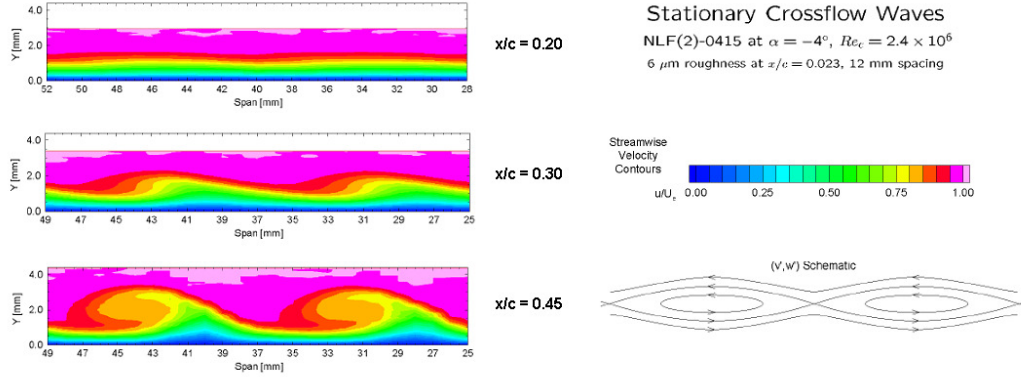
FIGURE I.5. Co-rotating vortex structure characteristic of the crossflow instability in the presence of discrete roughness elements (data from Reibert, Saric, Carrillo & Chapman 1996).

figure I.5, whose axes are aligned to within a few degrees of the invsicid stream direction.

Although stationary crossflow waves are typically weak and the initial growth of disturbances is linear, the small motion of the crossflow wave produces a strong distortion in the streamwise boundary-layer profile. This results in a modification of the basic state and early development of nonlinear effects (Radeztsky, Reibert & Saric 1994; Reibert, Saric, Carrillo & Chapman 1996; Saric, Carrillo & Reibert 1998*b*; Saric 2008*a*). This crossflow vortex structure may have a primary wavelength λ equal to that of the most unstable disturbance. The structure supports harmonics in waveneumber space of the most unstable wavelength ($\lambda/2$, $\lambda/3$, etc.), but not subharmonics with longer wavelengths. This feature of the flow is exploited in §I.3.3 in order to delay transition using a spanwise-periodic array of micron-sized DREs in conjunction with a judiciously designed pressure gradient. The array of DREs are used to strategically excite a relatively shorter wavelength to establish a flow pattern that prevents longer, more unstable wavelengths from growing. The DRE control wavelength saturates nonlinearly without causing transition on its own.

Crossflow exhibits amplified disturbances that are stationary as well as traveling. Although both types are typically present on a swept wing, transition is usually caused by one or the other, but not both. Whether the stationary or traveling wave dominates transition depends on the receptivity process. Stationary waves dominate in low turbulence environments characteristic of flight, while traveling waves dominate in high-turbulence environments (Deyhle & Bippes 1996). Freestream turbulence appears to be the source of traveling crossflow (White & Saric 2005). This dissertation focuses on the design of a flight experiment and therefore principally considers control of stationary crossflow disturbances.

The stationary crossflow instability is sensitive to 3D surface roughness. The specific relationship between surface roughness height and initial amplitude of crossflow disturbances is not yet well understood, a major focus of current receptivity research (Rizzetta, Visbal, Reed & Saric 2010; Hunt &

Saric 2011). Empirical results in flight testing showed that a polished leading edge ($R_q \approx 0.3\ \mu$m RMS) allow transition due to stationary crossflow to occur at LST N-factors as high as $N = 14$, in contrast to a more operationally relevant leading edge ($R_q \approx 3.0\ \mu$m RMS) where transition can be expected to occur at $N = 9$ (Rozendaal 1987; Schrauf 2004; Saric, Carpenter & Reed 2011).

This sensitivity to surface roughness is one of the primary complicating factors in applying the e^N method for transition prediction in swept-wing laminar flow control, as it is not known what value of N corresponds to transition without both quantifying the freestream environment and as well as the measured surface roughness for the leading edge in question.

I.3. Swept-wing laminar flow control

Practical laminar flow control on swept-wing aircraft is an area of persistent research interest. Surveys of recent flight experiments and results include Collier (1993), Joslin (1998), and Braslow (1999), Arnal & Archambaud (2008). Numerous issues are involved, including topics such as the effect of insect and ice accumulation on laminar flow extent (Coleman 1961; Wagner, Maddalon & Fisher 1990; Elsenaar & Haasnoot 1992; Humphreys 1992) and tighter manufacturing tolerances required for laminar flow operation (Braslow, Maddalon, Bartlett, Wagner & Collier 1990; Sacco & Piaggio 1996; Horstmann & Körner 1996).

In principle, the simplest means to achieve laminar flow on an aircraft is to unsweep the wings, say by limiting $\Lambda_{\mathrm{LE}} \leq 20°$. For unswept wings, attachment line and crossflow instabilities would be essentially eliminated, and one could then focus on controlling TS-type transition with a sufficiently favorable pressure gradient as far aft as possible. Unfortunately, wings of low sweep typically suffer from low drag-divergence Mach numbers at transonic speeds, likely outweighing any gain from the application of laminar flow.

The approaches that have attracted the most research interest for SWLFC are NLF, LFC using full-chord suction, and HLFC. In the terminology of Arnal & Archambaud (2008), these three techniques are the "industrial" methods for laminar flow control, which is to say that they have attracted significant flight and wind tunnel testing such that the TRL is relatively high for certain applications. "Research" techniques include passive SWLFC using DREs, as well as wave cancellation, streamwise streaks, and thermal control by wall cooling. Wave cancellation and streamwise streaks are not applicable here, while cooling has practically no effect on crossflow disturbances (Arnal 1994). Heating may be useful for control of attachment line instabilities in the calibration of a laminar-flow "health"-monitoring system (Mavris, Saric, Ran, Belisle, Woodruff & Reed 2010; Reed & Saric 2011).

There has been a wide variety of research conducted towards maturing these approaches in both the US and Europe in the past 50 years. A selection of published laminar extents in relevant flight tests plotted in Figure I.6 as a function of maximum transition Reynolds number $Re_{x,tr}$ versus Λ_{LE}, following data from Wagner, Maddalon, Bartlett & Collier (1988). Research effort is directord towards

the sweep angles and $Re_{x,tr}$ representative of transport aircraft and pushing the demonstrating towards the practically achieveable limit suggested by Henke, Capbern, Davies, Hinsinger & Santana (1996).
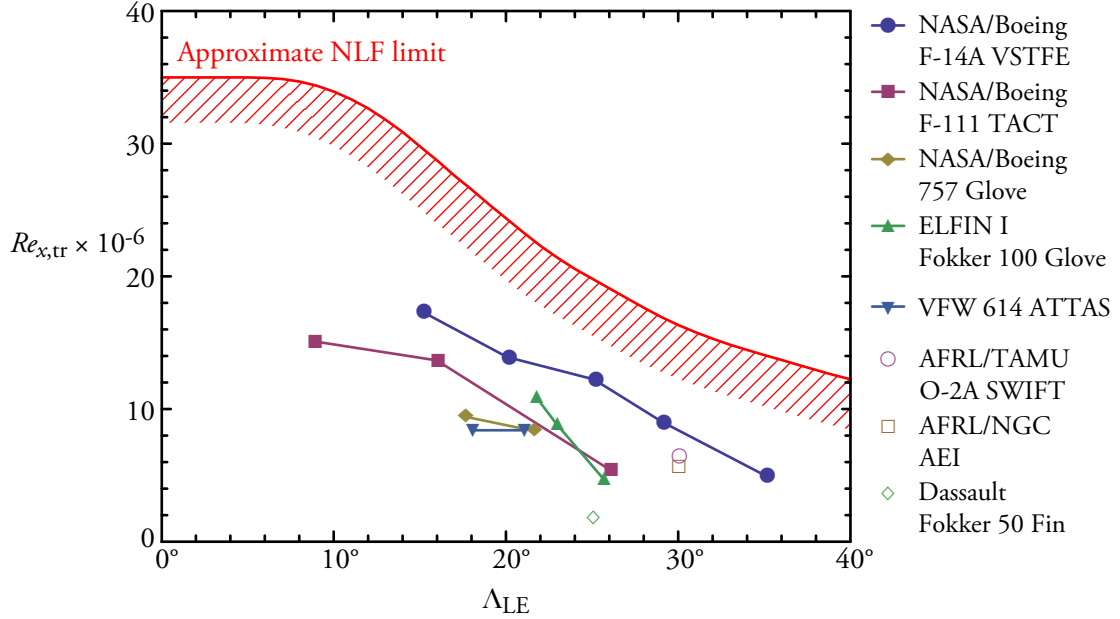
FIGURE I.6. Maximum published NLF extent in recent flight experiments and approximate NLF limit of Henke *et al.* (1996) with data from Wagner *et al.* (1988) and various flight test reports.

Operational NLF aircraft to date are principally low sweep, low Re_c designs, such as the Piaggio P-180. According to Sacco & Piaggio (1996), normal maintenance procedures are sufficient to guarantee NLF performance over the life of the airplane. No significant degradation was noted in fatigue simulations of approximately 60 000 flights nor in actual total life of up to 24 000 hours spread out over five years on operational P-180 aircraft.

This research focuses on raising the TRL of passive SWLFC using DREs, described in §I.3.3, as well as extending NLF to higher Reynolds beyond limits previously demonstrated. In comparison to an active technique like suction LFC, the advantage of DREs include little or no additional maintenance or action required for ongoing operation, nor any impact on weight or engine fuel consumption. DREs are no silver bullet: the practical issues such as "health" monitoring, manufacturing tolerances, and protecting the leading edge from bug strikes apply to the DRE technique just as they do to any other technique. They are also very low TRL. Even so, these challenges are common to many laminar flow approaches and thus do not uniquely disqualify DREs from consideration for further maturation.

I.3.1. *Suction and hybrid laminar flow control*

Suction is an active technique with a robust history of successful flight and wind tunnel demonstration (Joslin 1998; Braslow 1999). In this technique, the boundary-layer mean flow is modified by applying a small amount of suction through slots or perforations in the skin. The pioneering X-21A re-wing flight tests were the first successful, large scale application of the full-chord suction technique (Kosin 1965; Pfenninger 1965*a,b*). The JetStar experiments provided an approximately year-long simulated service study for HLFC (Wagner, Maddalon & Fisher 1990). Boeing (1993) conducted the 757 HLFC glove experiment in the early 1990s; around the same time Airbus A320 executed the HLFC fin program (Henke *et al.* 1996).

Although the suction technique is generally successful and well-tested, there are a number of concerns about reliability and maintenance of the suction system and porous or slotted surfaces, as well as weight and fuel consumption penalties from the suction compressors and plumbing. To this day, no large-scale production aircraft has been manufactured or designed with a suction LFC or HLFC system.

I.3.2. *Natural laminar flow*

The NLF technique relies on shaping of wing flow field through shape modification of the wing outer mold line (OML) exclusively. This technique forms the basis for other techniques such as HLFC and DRE SWLFC. The NLF technique follows from the stability behavior of an inflectional velocity profile. For streamwise instability, an inflection point is avoided by imposing a favorable pressure gradient. At low sweep and in the absence of crossflow, NLF the can theoretically delay transition to $Re_{x,tr} >$ 20 million. Such an approach is applied in the thin-wing, low sweep of the Aerion supersonic business jet concept (Sturdza 2007), a design currently in search of a manufacturer. For crossflow instability, the task is considerably more complex due to the inherent inflection point present in the crossflow boundary layer profile of figure I.2*(b)*.

NLF alone is only useful up to a practical $Re_{x,tr}$ limit that depends on Λ_{LE}. One proposed limit is shown in figure I.6, adapted from Reneaux & Blanchard (1992) and Henke *et al.* (1996). It is evident from figure I.6 that no flight experiment to date has successfully challenged this hypothetical limit. Significant attempts that include $\Lambda_{LE} \geq 20°$ are described in the following sections.

NASA/Boeing F-111/TACT NLF glove. The National Aeronautics and Space Administration (NASA) and Boeing conducted a flight test program on the F-111 Transonic Aircraft Technology (TACT) aircraft in the mid-1980s, reported in Boeing (1984). The experiment surveyed $Re_c =$ [23, 29] million and $M = [0.80, 0.85]$. Measured laminar flow extents, with significant uncertainty due to the indirect measurement technique, on the upper surface ranged from $(x/c)_{tr} = 0.56$ at $\Lambda_{LE} = 9°$ to $(x/c)_{tr} = 0.21$ at $\Lambda_{LE} = 25°$. On the lower surface, the extents ranged from $(x/c)_{tr} = 0.51$ at $\Lambda_{LE} = 9°$ to $(x/c)_{tr} = 0.06$ at $\Lambda_{LE} = 25°$. Because of the limitations in the experimental techniques and lessons learned in the design process, a follow-on experiment with a larger Re_c and M range, as well

as a longer span glove, was recommended.

NASA/Boeing F-14A VSTFE NLF glove. The Variable Sweep Transition Flight Experiment (VSTFE) was a effort carried out by Boeing, NASA Langley Research Center (LaRC), and NASA Dryden Flight Research Center (DFRC) from 1984 to 1987 on a F-14A aircraft using wing gloves on the port and starboard wings (Anderson & Meyer 1990*b*,*a*; Rozendaal 1986). The VSTFE experiment appears to make use of the marginally successful F-111/TACT experience.

Anderson & Meyer (1990*a*) reports flight test results for the first VSTFE glove, a "cleanup" glove installed on the port wing of the test aircraft. The cleanup glove smoothed the surface of the F-14A wing without appreciably altering the pressure distribution. The motivation for this approach comes from the emerging realization in the late 1980s that crossflow transition is influenced by 3D surface roughness. Since the F-14A has a favorable pressure gradient at $M > 0.7$, in principle smoothing the surface would be expected to increase the laminar flow extent when transition is due to crossflow. Indeed, the smooth glove demonstrated $Re_{x,tr}$ ranging from $Re_{x,tr} = 13.7$ million at $\Lambda_{LE} = 15°$ to $Re_{x,tr} = 1.8$ million at $\Lambda_{LE} = 35°$ (Anderson & Meyer 1990*a*; Figure 18). No measurements of the baseline F-14A transition locations were made, so the effect of smoothing the surface on crossflow transition is not known from these data.

The second VSTFE glove, installed on the starboard wing of the F-14A test aircraft, modified the pressure distribution in addition to smoothing the surface. The flight test results of this phase of the VSTFE study are covered in Anderson & Meyer (1990*b*). This glove had an airfoil shape designed for laminar flow at $\Lambda_{LE} = 20°$and flight tested at sweeps ranging from $\Lambda_{LE} = 15° - 30°$. Maximum $Re_{x,tr}$ for this phase of the experiment is included in figure I.6, ranging from $Re_{x,tr} = 18.7$ million at $\Lambda_{LE} = 15°$ to $Re_{x,tr} = 5.0$ million at $\Lambda_{LE} = 35°$, a notable improvement over the smooth glove case (Anderson & Meyer 1990*b*; Figure 19) and the F-111/TACT glove.

Since the VSTFE simply altered the sweep angle for a glove designed at $\Lambda_{LE} = 20°$, these results should not be considered to be the practically achievable limit of maximum $Re_{x,tr}$ using NLF at other sweep angles, even if they are at present the flight-demonstrated limit. This is one motivation for demonstrating NLF using a glove designed at $\Lambda_{LE} = 30$, as described in further detail in chapter II.

Dassault Falcon 50 NLF fin. In France, a joint effort by Dassault Aviation, Aèrospatiale and ONERA-CERT executed a NLF feasibility and flight environment characterization flight test on the Falcon 50 in 1985–1987 (Arnal & Bulgubure 1990; Bulgubure & Arnal 1992; Courty, Bulgubure & Arnal 1993). The NLF test on a fin that replaced part of the vertical stabilizer considered sweep angles of 25 degrees and 35 degrees at Re_c of a few million, achieving up to $(x/c)_{tr} = 0.5$. The experiment attempted to validate transition prediction criterion developed by (Arnal, Habiballah & Coustols 1984).

VFW 614/ATTAS NLF glove. The German laminar-flow research program sponsored NLF glove tests on the VFW 614/Advanced Technologies Testing Aircraft System (ATTAS) platform from 1986–1989 in Germany Redeker, Horstmann & Köster (1990); Horstmann, Redeker & Quast (1990);

Schrauf, Herbert & Stuckert (1996). Like in the Falcon 50 experiment, the primary objective included collection of flight test transition data for code calibration. Tests covered the range $M = [0.35, 0.7]$, $Re_c = [12, 30]$ million and $\Lambda_{\text{LE}} = [18°, 24°]$. Tests demonstrated transition due to crossflow, TS, and attachment-line instabilities consistent with predictions. Maximum chord transition was $(x/c)_{\text{tr}} = 0.5$ at $M = 0.35$, $Re_c = 18.5$ million, and $\Lambda_{\text{LE}} = 12°$.

ELFIN F100 NLF glove. Following the Falcon 50 tests and VFW 614/ATTAS tests, the European community and Airbus conducted a follow-on glove test in the European Laminar Flow Investigation (ELFIN) Phase I using a part-span wing glove on the Fokker 100 aircraft from 1990–1992. The objectives of ELFIN I included validation and calibration of existing prediction methods, assessment of the performance of the glove in terms of drag reduction potential, and to establish limits for NLF application (Voogt 1993, 1996).

During the ELFIN glove design process, Dreßler, Hansen, Rill, Horstmann, Rohardt & Wichmann (1992) identified strong three-dimensionality in the glove flowfield, necessitating a design process dependent on 3D Euler calculations rather than a lower-order 2D strip method. They paid significant attention to the fairing airfoils, designing at least five fairing airfoils in addition to three airfoils in the glove test region.

Complete results for the ELFIN I investigation have never been published. From the sparse data that was published, it appears that the results were inconclusive. The investigators encountered significant issues related to glove finishing and the glove required refinishing to achieve design pressure distributions. The maximum published transition extent is $(x/c)_{\text{tr}} = 0.5$ at $M = 0.75$, $\Lambda_{\text{LE}} = 23°$, $Re_c = 22$ million, and $C_\ell = 0.4$ (Voogt 1993), a result exceeded by $Re_{x,tr} = 12$ million achieved at similar conditions in VSTFE (Anderson & Meyer 1990b).

NASA/Boeing 757 NLF glove. NASA LaRC contracted Boeing for a NLF glove experiment on a 757 in order to survey the effects of the engine noise field on laminar flow (Runyan et al. 1990). Complete design information and flight test data is published in Boeing (1988; 1987b; 1987a). The glove test article had design $\Lambda_{\text{LE}} = 21$, $M = 0.8$ at an altitude of 40 000 ft. Tested Mach numbers included $M = [0.63, 0.83]$ and altitude $H = [25 000, 41 000]$ ft, with focus on $M = \{0.8, 0.7\}$ and $H = \{35 000, 39 000\}$ ft.

The 757 NLF glove was designed such that significant laminar flow extents could be achieved on the glove upper and lower surfaces simultaneously. Maximum chordwise laminar flow extent $(x/c)_{\text{tr}} = 0.29$ occurred on the upper surface at $M = 0.825$, $H = 40 761$ ft, $C_\ell = 0.495$ at the design sweep. On the lower surface, the maximum extent $(x/c)_{\text{tr}} = 0.27$ was at reduced sweep with $M = 0.699$, $H = 39 042$ ft, $C_\ell = 0.644$. Laminar extent on the upper surface was limited in the outboard region by a peak in the pressure distribution at about 5% chord, a result not predicted by the transonic analysis program used to design the glove (Runyan et al. 1990).

Engine noise correlated with varying engine power settings showed minimal effect on transition on

the upper surface, where transition was due to crossflow. One the lower surface, increased power settings had a marginal decrease on the TS-dominated transition location.

AFRL/TAMU O-2A SWIFT SWLFC fin. Starting in 2006, Air Force Research Laboratory (AFRL) contracted the Texas A&M University Flight Research Laboratory (TAMU FRL) to conduct an in-flight test of NLF and SWLFC using DREs on a fin mounted on a Cessna O-2A (Carpenter 2009; Saric, Carpenter & Reed 2011). The fin represents a SensorCraft-type wing section with $\Lambda_{LE} = 30°$. The objectives of the experiment included measurements of the free-stream environment in flight to establish its suitability for boundary layers stability and transition measurements and to mature laminarization technology using DREs. Measurements of the freestream environment by Saric *et al.* (2011) showed turbulence intensity $u'/U_\infty = [0.05, 0.06]$, suitably low to expect stationary crossflow disturbances to dominate over travelling (following the wind tunnel results of Deyhle & Bippes 1996).

The test article design includes a removable leading edge, providing the ability to quantify the effect of leading-edge surface roughness on crossflow-dominated transition in the flight environment. Saric *et al.* (2011) describe two representative flights that substantiate the sensitivity of stationary-crossflow dominated transition to surface roughness. The first flight demonstrated $(x/c)_{tr} = 0.8$ at $Re_c = 8.1 \times 10^6$ with a leading edge polished to $R_q = 0.3$ μm RMS (peak-to-peak $R_t = 2.2$ μm). This result corresponded to LST $N = 14$. The second flight at $Re_c = 8.0 \times 10^6$ with a leading edge painted to $R_q = 1.0$ μm RMS ($R_t = 3.8$ μm) showed that transition moved forward to $(x/c)_{tr} = [0.25, 0.30]$, corresponding to $N = 7$. As described in the following section, a flight using DREs at these same conditions delayed transition to $(x/c)_{tr} = 0.60$. Computational analyses on the platform support these results and include Rhodes, Reed, Saric & Carpenter (2010); Rizzetta, Visbal, Reed & Saric (2010); Carpenter, Choudhari, Li, Streett & Chang (2010); Li, Choudhari, Chang, Streett & Carpenter (2011).

AFRL/NGC White Knight I AEI SWLFC fin. In order to substantiate NLF applicability to a high-altitude long-endurance SensorCraft vehicle, AFRL contracted Northrop Grumman (NGC) to conduct the Aerodynamic Efficiency Improvement (AEI) fin test on the White Knight I carrier aircraft. Drake & Solomon (2010) designed a test article that reproduced a section of the SensorCraft flying wing configuration, demonstrating that laminar flow at these conditions could be attained while meeting all of the vehicle requirements. Simultaneous suction- and pressure-side laminar flow was demonstrated at the primary test point $Re_c = 7$ million, typically observed close to the pressure minimum that occurred at $x/c = 0.4$ on the suction side and $x/c = 0.75$ on the pressure side.

I.3.3. *Passive SWLFC using DREs*

On the swept wings of long-range transport aircraft, the preceding sections described the primary options for transition delay. Following the approach of Saric *et al.* (2011), the technologies may be recommended for SWLFC in order from highest TRL to lowest TRL.

The first option, with the longest history of successful flight demonstration, is suction LFC and

HLFC (Braslow 1999). Despite the technology's history of successful demonstration, economic and integration considerations have prevented adoption of suction-type LFC on operation aircraft.

The second approach is to unsweep the leading edge. A wing with low sweep would eliminate attachment line and crossflow instabilities, leaving only streamwise instability to be controlled through NLF design by imposing a sufficiently favorable pressure gradient and curvature instability to be controlled by avoiding concave geometry. This approach has seen success on low-Re_c aircraft such as the P-180 (Sacco & Piaggio 1996) and Global Hawk.

For an aircraft similar in size to the 737 or A320, natural laminar flow may be an option. For a 737, $Re_c = 23.4$ million in typical cruse based on the mean aerodynamic chord $MAC = 3.8$ m (12.5 ft) and $\Lambda_{LE} = 27.2$ (Brady 2013; Boeing 2006). Assuming $(x/c)_{tr} = 0.6$ gives $Re_{x,tr} = 14$ million, the lower end of the approximate limit in figure I.6.

For larger aircraft, achieving laminar flow extents $(x/c)_{tr} < 0.6$ raises economic questions (Robert 1992) and it is prudent to look for technologies to extend the achievable amount of laminar flow. Use of an exceptionally thin wing permits laminar flow and low sweep at supersonic speeds on the Aerion supersonic business jet concept (Sturdza 2007). However, such thin wings raise structural concerns, and thicker wings may suffer from wave drag penalties that offset the gains due to laminar flow.

The third option for transonic swept-wing aircraft is to polish the leading edge. As substantiated by numerous authors including Radeztsky *et al.* (1993), Deyhle & Bippes (1996), and Saric *et al.* (2011), polishing leading edge stabilizes stationary crossflow. A polished leading edge with $R_q = 0.3$ μm RMS can achieve *N*-factors for transition as high as $N = 14$ in flight (Saric *et al.* 2011). According to measurements of leading edge surface roughness by Carpenter (2009), aircraft such as the Gulfstream V may have finishes of this quality. Nevertheless, over the lifespan of a transport aircraft that typically exceeds three or four decades, maintenance of the pristine leading edge is a concern.

After these three options are eliminated, the only remaining passive technique is SWLFC using DREs. However, the TRL of DREs is not high, at most TRL 3 meaning that a proof of concept has been demonstrated in a laboratory, principally experiments of Reibert, Saric, Carrillo & Chapman (1996). These experiments in the Arizona State University Unsteady Wind Tunnel used the NLF(2)-0415 airfoil swept to $\Lambda_{LE} = 45°$. At nominal $Re_c = 2.4$ million (unit $Re' = 0.5$ million/ft) and $AoA = -4°$, sufficient crossflow is generated such that LST predicts to do be the dominant instability that triggers transition.

LST showed the most unstable stationary crossflow disturbance to have wavelength $\lambda_1 = 12$. A spanwise-periodic array of appliqué DREs with height $h = 6$ μm and spacing $\lambda_2 = 12$ mm was used to establish a uniform transition front. An FFT-based power spectral density showed the dominance of the fundamental 12-mm mode, along with the 6-mm harmonic.

Demonstration of the DRE technique for the delay of transition was carried out on the same model and conditions by Saric, Carrillo & Reibert (1998*a,b*). Here, it was found that DRE spacing with $\lambda_2 = 6$ or 8 mm effectively suppressed growth fo the most unstable waves with $\lambda_1 = 9$ or 12 mm.

Following from §I.2.4, the crossflow vortex structure permits subharmonics in wavenumber space of the most unstable wavelength λ, but not superharmonics. The nonlinear nature of the crossflow instability results in nonlinear saturation where the vortex structure can persist without triggering transition. This principle is exploited by judicious shaping of the pressure gradient such that a subcritical wavelength ("killer", by the terminology of Arnal & Archambaud 2008). λ_1 can be strategically excited to establish a baseline structure that prevents longer wavelengths from growing. In particular, the control prevents the most unstable, "target" wavelength λ_2 from growing. The net effect is that transition is delayed. The design philosophy for DRE control is described in §III.1.3.

CHAPTER II

HIGH REYNOLDS NUMBER DRE FLIGHT EXPERIMENT

The Subsonic Aircraft Roughness Glove Experiment (SARGE) is a high Reynolds number SWLFC wing glove experiment. The primary objective of the experiment is to raise the technical readiness level (TRL) of the DRE technique for transition delay on a swept wing at Re_c and Re' representative of transport aircraft such as the Boeing 737. The secondary objective is to demonstrate NLF at conditions exceeding that previously demonstrated by experiments such as those described in §I.3. The experiment is funded by the National Aeronautics and Space Administration Environmentally Responsible Aviation (NASA ERA) initiative. Collier (2010) overviews the larger program.

The SARGE experiment is the logical next step after the experiments described in chapter I. The evolution of the flight experiment is described in detail in a series of conference papers: Belisle, Neale, Reed & Saric (2010); Belisle, Roberts, Tufts, Tucker, Williams, Saric & Reed (2011); Hartshorn, Belisle & Reed (2012); Belisle, Roberts, Williams, Tufts, Tucker, Saric & Reed (2012); Roberts, Reed & Saric (2012). Supporting analysis by NASA personnel include Malik, Liao, Li & Choudhari (2013); Liao, Malik, Lee-Rausch, Li, Nielsen, Buning, Chang & Choudhari (2012); Malik, Liao, Lee-Rausch, Li, Choudhari & Chang (2011); Li, Choudhari, Carpenter, Malik, Chang & Streett (2010). TAMU students published detailed results in a series of theses and dissertations: Neale (2010); Roberts (2012); Williams (2012); Tucker (2012) and this document.

These nine papers, plus three theses and two dissertations, represent over one-thousand pages of documentation on this experiment, a substantial body of work on an experiment that hasn't yet been fabricated. A two-year schedule, shown in figure II.1, developed for the project during the initial planning stages turned out to be an optimistic timeline. As the experiment grew and matured, the experiment went through a number of requirement changes, the number of personnel involved grew, and the actual timeline became much more complicated and the milestones monotonically shifted to the right. The actual schedule from the start of the project in September 2008 through the successful preliminary design review (PDR) conducted at NASA DFRC in June 2012 is in figure II.2.

One downside of publishing regular results before the design is finalized is that many findings in earlier papers are superseded or made irrelevant by later papers, making it difficult to find the salient lessons learned for future work. In a forward to the directions to contributors included the *Journal of General Microbiology* from 1954 to 1974, editors Knight and Standfast provide an admonishment to prospective authors:

> A paper should be written only when a piece of work is rounded off. Authors should not be seduced into writing a series of papers on the same subject seriatim as results come to hand. It is better, for many reasons, to wait until a concise and comprehensive paper can
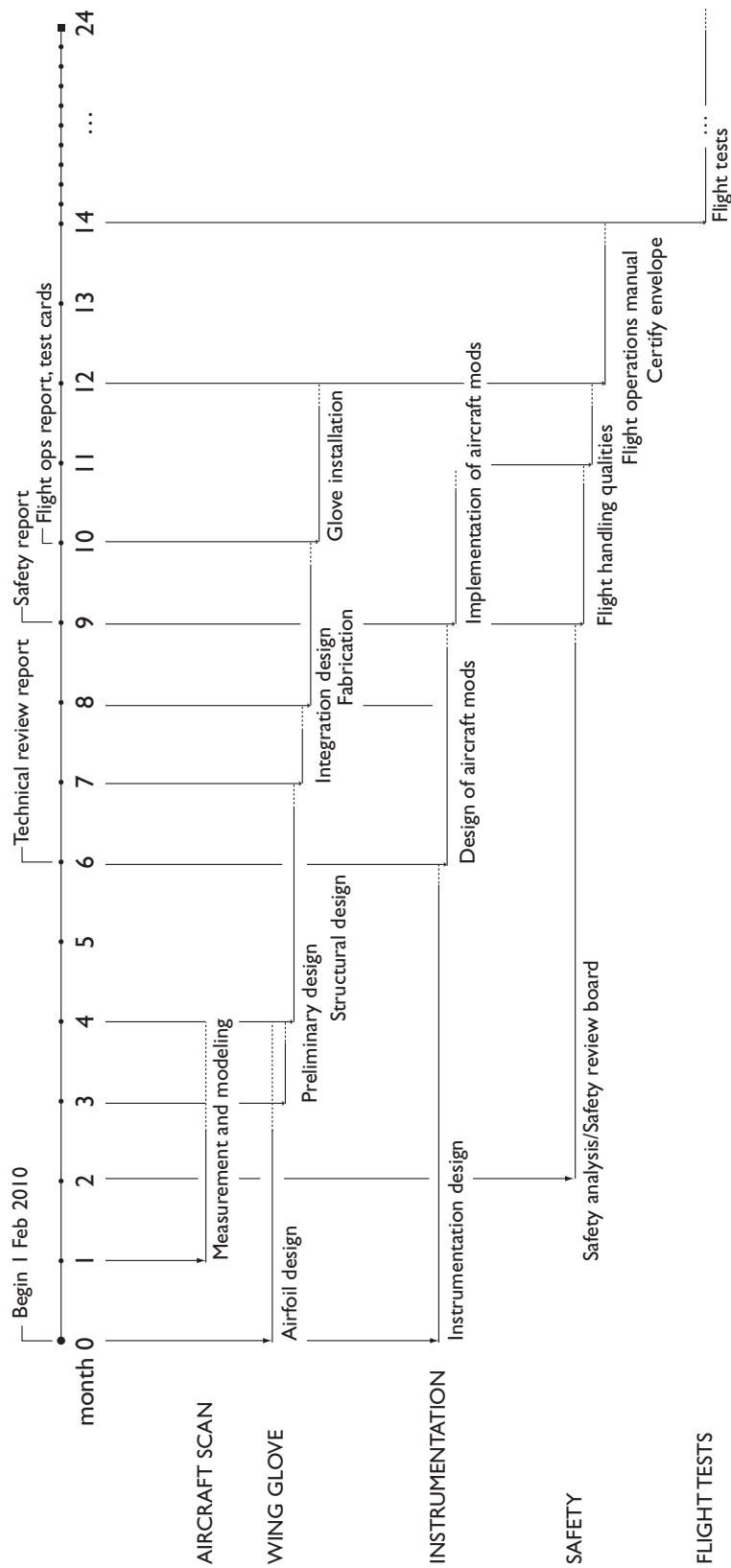
FIGURE II.1. Initial timeline of the SARGE experiment from contract start anticipated in February 2010 through planned completion 24 months later in February 2012.

FIGURE II.2. Actual timeline of the SARGE experiment from contract start in September 2008 through PDR in June 2012.

> be written. (Knight & Standfast 1968)

This is generally good advice. Unfortunately, in a large-scale flight experiment like SARGE, such temptation is hard to resist: students have to graduate and collaborators and project sponsors across the country are eager to see results disseminated to the public (even when those results are intermediate, preliminary, and subject to change).

This chapter reviews the main results during the interval charted in figure II.2.

II.1. Flight experiment feasibility

DREs are a technology intended to extend SWLFC beyond that permitted by NLF design alone (§I.3.3). Despite the efforts in past flight experiments, the conclusive NLF limit in flight has not yet been established, although some have been proposed limits similar to that in figure I.6. In practice, such a limit may never be defined because the amount of achievable laminar flow is circularly influenced by design requirements, which necessarily reflect a compromise between many competing disciplines.

The situations is complicated by the fact that the limit in the flight environment is not one that can be readily studied in wind tunnels, which struggle to maintain a low-disturbance environment characteristic of flight when M exceeds about 0.5. At higher speeds, elevated disturbance levels tend to excite traveling crossflow disturbances rather than stationary ones like in flight, for which DREs are no remedy. Demonstration of SWLFC at high Re_c where they are likely to be required to meet design requirements can only be conducted in flight. Unfortunately, flight experiments at these conditions are expensive.

Efforts to date therefore focus on understanding the behavior and operation of DREs in lower-cost experiments where they are not necessary, but can be used regardless by intentionally operating with elevated levels of stationary crossflow. The philosophy is that if we cannot understand DREs at low Mach number and low Re_c, at conditions where laminar flow could typically be maintained through NLF without DREs, we have little hope of demonstrating them in a cost-effective manner at more challenging, high-Re_c conditions representative of the expected target application.

In order to continue DRE technology maturation towards a TRL 5 demonstration in a relevant environment for transport applications, a follow-on experiment to SWIFT is needed. In Belisle *et al.* (2010), SARGE began by addressing three prerequisite questions:

1. Is it possible to find an aircraft that can be used as a platform for this experiment?
2. Given the aircraft, does a CFD of the aircraft flowfield show that there is no interference from engines and control surfaces that would compromise the experiment?
3. Is it possible to design an airfoil with a representative overall lift coefficient C_L and pressure coefficient C_p distribution that makes DREs feasible?

Assuming the notionally relevant parameters in table II.1, the answer to all of these questions is yes.

H	40 000 ft
M_∞	0.75 (originally 0.80)
Re_c	15–20 million
Re'	1.6 million/ft
t/c	$\approx 10\%$
Λ_{LE}	$\approx 30°$

TABLE II.1. Project design parameters during initial feasibility evaluation.

II.1.1. *Aircraft selection*

In the initial requirements for this experiment the target $Re_c = [15, 22]$ million was representative of a business jet as a logical follow on to $Re_c = [7, 8]$ million in SWIFT on the Cessna O-2A. Belisle *et al.* (2010) evaluated a list of seventy candidate aircraft.

The initial downselect identified business-jet-class aircraft having fuselage mounted engine nacelles, cruise $M \geq 0.8$, service ceiling $H_{\max} \geq 40\,000$ ft, and $\lambda_{\mathrm{LE}} \approx 30°$. Referring to the parameters in table II.1, these aircraft are capable of supporting a glove design with sufficient crossflow growth to ensure transition due to stationary crossflow (as required for DREs to function). Additional emphasis was given to aircraft expected to be available for a dedicated, 6–12 month flight test program. These criteria favored three aircraft: Sabreliner 80 (S80), Gulfstream II (G-II, also G-II/SP, a G-II with Aviation Partners blended winglets), and Gulfstream III (G-III, also G-II/B, a G-II rewinged with the G-III wing). Characteristics of these aircraft are presented in table II.2.

Aircraft	Wing Span (ft)	Wing Sweep ($c/4$)	Max Cruise Speed (Mach)	Max Altitude (ft)
S-80	44.5	28.5°	0.80	45 000
G-II/SP	68.8	25.0°	0.85	43 000
G-III	77.8	27.7°	0.85	45 000

TABLE II.2. Downselected aircraft specifications

The S-80 is a significantly smaller aircraft than the G-II and G-III, which would require mounting the wing glove close to the fuselage in order to achieve the desired Re_c in level flight. The base G-II has a wing with a number of aerodynamic "fixes," such as extensive vortex generators and a mid-semi-span fence. The aircraft dynamic effects of removing these features has potential impacts on the aircraft handling properties which complicate a potential design. The relatively cleaner wing on the G-II/SP made it more appealing than the G-II. Of these three, the G-III has the cleanest wing and its larger

chord is can most suitable for providing a large Reynolds number range, but during these initial phases a G-III was not expected to be available for testing. Thus, initial analyses focused on a G-II/SP aircraft, tail number N949NA, owned by NASA and stored at the Forward Operating Location in El Paso, Texas (figure II.3).

FIGURE II.3. The NASA G-II/SP (N949NA) on a tarmac at the NASA Forward Operating Location in El Paso, TX. (Belisle *et al.* 2010)

II.1.2. *Aircraft suitability*

Establishing the suitability of the N949NA principally focused on answering two questions:

1. What Reynolds numbers are achievable with a modestly sized glove?
2. When including engine effects, is there a suitable flow environment on the wing for placement of a glove?

The first question can be answered using the wing planform and considering what can be achieved at operations below the operating ceiling of $H_{max} = 45\,000$ ft. Shown in the figure II.4 is a modestly sized glove, notionally limited to extend no more than 12 inches in front of the aircraft wing leading edge, with mean aerodynamic chord $MAC \approx 3.6$ m (12 ft). By varying altitude to control Re_c, the G-II at $M = 0.8$ is capable of achieving $Re_c = [15, 20]$ million on this notional glove in the altitude band $H \approx [38\,000, 44\,000]$ ft.
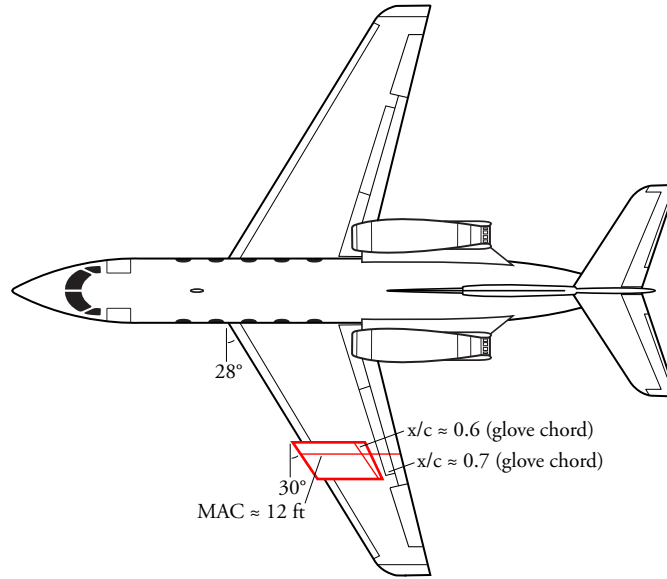
FIGURE II.4. G-II notional glove location plan view (adapted from NASA 1998).

A quantitative answer to the second question requires computational fluid dynamics (CFD) computations on an sufficiently accurate computer-aided design (CAD) model of the aircraft. For the G-II/SP, a readily available model was not available, perhaps due to proprietary limitations. Even if a CAD model was available, it would not be likely to be accurate due to the age of the aircraft.

The most effective means to obtain a model was therefore to perform a laser scan of the exact aircraft under consideration. This scan was performed by Direct Dimensions, Inc (DDI) of Owens Mills, Maryland. To scan the aircraft, the G-II/SP was placed on jacks for the duration of the two-day scan and housed inside an environmentally controlled hangar. DDI used a Surphaser 25 HSX medium-range laser scanner with single-point accuracy of 0.25 mm (0.01 in). Half of the aircraft was scanned, treating a vertical plane through the center of the aircraft as a plane of symmetry. The empennage of the G-II was ignored during the scanning and modeling process since it would not have an effect on the wing flowfield (Rhodes, Reed, Saric & Carpenter 2010) and its elimination results in a significant time and cost reduction.

The laser scanner acquired millions of points that formed a "point cloud" to which DDI fit surfaces, neglecting the complexity of the engine. DDI constructed models with no engines, flow-through nacelles, as well a flat plane nacelle inlet and exit (where a mass flow boundary would be defined in the CFD). Comparison of results of CFD computations on these three cases established the effect of the engine on the wing flow field.

The full details of the CFD computations are covered in Neale (2010). The flow domain is constructed into a manner similar to Rhodes *et al.* (2010), consisting of a sequence of nested domains

(*a*) Freestream volume (structured)   (*b*) Aircraft volume (unstructured)   (*c*) Wing volume (structured)
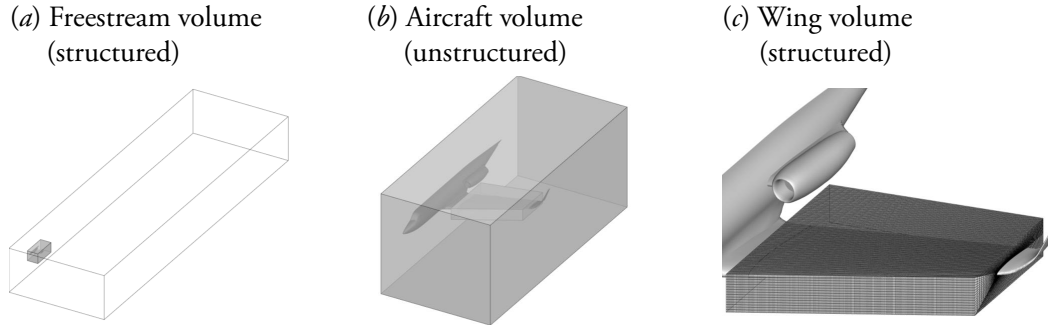
FIGURE II.5. Hybrid structured/unstructured nested computational domain developed by Neale (2010) following the approach in Rhodes *et al.* (2010) (Belisle *et al.* 2010).

from the region of interest near the surface of the wing to the farfield (figure II.5). In order to minimize the overall cell count while maintaining sufficient detail in regions of interest, the domain consists of three nested blocks. The block nearest to the wing is structured. The rest of the aircraft uses unstructured cells to capture complex details of the aircraft without the difficulty of a fully structured grid or complexity of an overset solution. Further away from the aircraft, the farfield block is structured. Grid interfaces (i.e. grid interpolation at the boundaries) connect the structured regions to the unstructured regions.

The three models with different engine configurations are used to isolate the effects of the engines from fuselage or other effects. Aircraft engines typically operate in "spillage" mode, which means that the nacelle does not accept entire flow at the inlet. The "closed" engine model considered the engine inlet and exit to be pressure boundaries with mass entering and leaving the domain, respectively. In the absence of having an engine deck that gives actual engine conditions for a particular flight condition, the pressure at the fan face is varied parametrically to establish a bound for the engine effects. Here, the inlet mass flow ratio (MFR) varies from 0.5 to 0.8, while the outlet pressure is selected such tat the exhaust flow corresponds to sonic flow.

The CFD results showed that engine effects are "accountable" on the G-II wing outboard of approximately 45% semispan. Here, accountable means that the pressure isobars are essentially spanwise uniform (conical), a qualitative criteria since a 3D wing is not expected to be perfectly conical. Principally, the idea is to avoid changes in pressure isobar sweep evident neared to the fuselage due to engine pressure effects, seen in figure II.6.

II.1.3. *Design feasibility*

Design and linear stability evaluation of a family of SWLFC airfoils provided a proof-of-concept justification for the feasibility of a high Re_c DRE flight experiment, summarized in table II.3.

The SWIFT airfoil geometry provided the starting point for the design. Increasing the Mach number
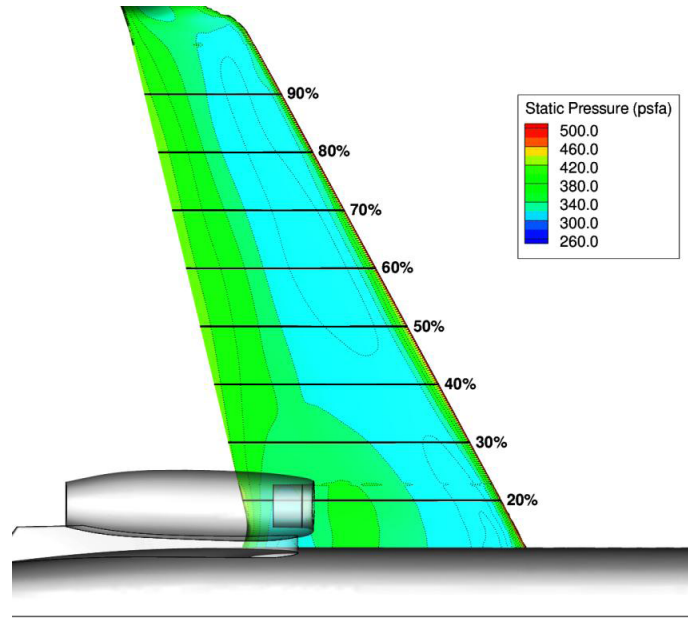
FIGURE II.6. G-II wing pressure isobars computed by Neale (2010). Engine effects in the worst case considered, MFR = 0.5, are accountable (i.e. the flow is reasonably conical) outboard of approximately 45% semispan (from Belisle *et al.* 2010).
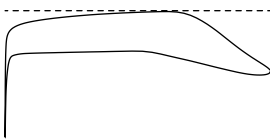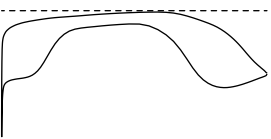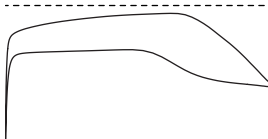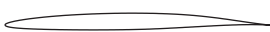
	TAMU-001T-80	TAMU-002P-80	TAMU-003T-75
$\text{-}C_p$ Airfoil			
M	0.80	0.80	0.75
H	40 000 ft	40 000 ft	40 000 ft
Q_∞	236 m/s (459 knots)	236 m/s (459 knots)	221 m/s (430 knots)
c	3.6 m (12 ft)	3.6 m (12 ft)	3.6 m (12 ft)
t/c	6.2%	9.1%	9.3%
r_{LE}	11 mm (0.43 in)	8 mm (0.31 in)	28 mm (1.1 in)
Re_c	18.3 million	18.3 million	17.2 million
Re_θ	52	44	86
C_{ℓ_0}	0.35	0.27	0.37

TABLE II.3. TAMU proof-of-concept airfoil series overview. The dashed line in the $\text{-}C_p$ figures is the critical C_p for sonic flow at the design Mach number.

from $M = 0.3$ in the SWIFT flight test to $M = 0.8$ in the initial phases of the proof-of-concept study first required significant airfoil thinning and additional camber to increase C_ℓ to representative G-II $C_\ell \approx 0.3$ at the target flight condition. The first airfoil in the series, TAMU-001T-75, is designed without regard for thickness constraints of the host G-II wing, showing that it is feasible for a $M = 0.8$ SWLFC airfoil to remain subsonic over its entire surface and achieve representative C_ℓ.

However, the limitations of the host aircraft requires thickness to be added in order to facilitate mounting on the G-II wing, approximately $t/c = 0.60$ at the prospective mounting location. Adopting the approach of Pfenninger *et al.* (1979) leads to TAMU-002P-80. Even with this approach, achieving the desired $C_\ell = 0.5$ while avoiding supersonic flow over the upper surface of the airfoil is difficult.

These two findings in the initial airfoil design guided the decision to scale the operational Mach number to 0.75, which reduced the critical C_p to -0.59 at $M = 0.75$ from -0.43 at $M = 0.80$. This led to TAMU-003T-75, a 9.3% thick airfoil that remains subsonic from design range $AoA = [-1, 1]$, corresponding respectively to $C_\ell = [0.25, 0.49]$. This airfoil is the focus in further feasibility analyses.

Linear stability at the $AoA = 0°$ design condition suggested large extents of laminar flow are achievable without the introduction of DRE control (table II.4). Here, stationary crossflow transition is assumed at $N = 9$ for an operational level of leading edge roughness; $N = 14$ for a polished leading edge wasn't attained under any condition. TS is less than $N = 7$ for all conditions. Transition due to TS is assumed to occur at the pressure minimum due to the adverse pressure gradient. This is noted in the table by a transition value greater-than-or-equal the location of the pressure minimum.

		Suction side		Pressure side	
AoA	C_ℓ	$(x/c)_{tr}$	$Re_{x,tr} \times 10^{-6}$	$(x/c)_{tr}$	$Re_{x,tr} \times 10^{-6}$
$-1.0°$	0.25	0.23	4.0	≥ 0.04	≥ 0.7
$-0.5°$	0.31	0.38	6.5	≥ 0.44	≥ 7.6
$0.0°$	0.37	≥ 0.59	≥ 10.1	≥ 0.44	≥ 7.6
$0.5°$	0.43	≥ 0.59	≥ 10.1	≥ 0.44	≥ 7.6
$1.0°$	0.49	≥ 0.59	≥ 10.1	0.06	1.0

TABLE II.4. Predicted transition locations on TAMU-003T-75 at $Re_c = 17.2$ million, $M = 0.75$ using LST e^N method with assumed stationary crossflow transition at $N = 9$.

These promising proof-of-concept transition results motivated another change in the experimental requirements: increasing the design chord Reynolds number range to $Re_c = [18, 22]$ million for NLF, and $Re_c = [22, 30]$ million for DRE control.

II.1.4. *Independent verification and nonlinear analysis*

Li, Choudhari, Carpenter, Malik, Chang & Streett (2010) independently performed a computational assessment of the TAMU-003T-75 airfoil. They focused on the off-design condition $AoA = -1^\circ$ in order to ensure sufficient stationary crossflow growth for their nonlinear PSE and secondary instability analysis methods. Their LST results at this condition verify those by TAMU in Belisle *et al.* (2010) described in the previous section.

Nonlinear PSE and secondary instability computations notionally support the use of DRE control with $\lambda_1 = 2.67$ mm and $\lambda_1 = 4$ mm wavelengths, showed an expected decrease in the most unstable $\lambda_2 = 8$ mm wavelength growth with increasing control amplitude input. These wavelengths are in agreement with the candidate wavelengths selected from LST.

These results are qualitative in nature, as the initial amplitudes for control and target wavelengths are arbitrarily chosen. This is a necessity in nonlinear PSE analysis of the crossflow instability, owing to both the lack of surface roughness information on a glove that has yet to be built in addition to the lack of a detailed understanding of the receptivity of the boundary layer to 3D surface roughness.

II.2. Subsonic Aircraft Roughness Glove Experiment

The feasibility of an experiment using a G-II aircraft as the reference platform demonstrated extends to the similar G-III. Therefore, NASA DFRC acquired a Gulfstream III aircraft with the intent for SARGE to be one of the first experiments flown on the new platform. The aircraft was assigned NASA tail number 804 and christened Subsonic Research Aircraft Testbed (SCRAT).

DFRC received tasking to be principally responsible for the flight operational planning, test article manufacturing design and construction. TAMU was responsible for test article OML design and mission success evaluation, while LaRC provided independent verification of the design as well as overall project authority. This phase of the project started in January 2010 and ran through the successful PDR in June 2012.

II.2.1. *Aircraft description*

SCRAT (figure II.7) is outfitted with a flight-research quality instrumentation system, telemetry, and reconfigurable cabin that allows researchers to monitor progress in real-time without need for a control room. Visible in the figure are the port side of the wing where the glove is intended to be mounted, as well as the IR-transparent window mounted in one of the emergency exit locations (green, just in front of engine).

Key G-III aircraft specifications are listed in table II.5. As with the G-II, DDI laser scanned the aircraft and constructed a CAD model. TAMU simplified some components for analysis, such as the details of the engine hush kit (Roberts 2012).

FIGURE II.7. NASA Gulfstream III SCRAT aircraft in functional test flight shortly after takeoff on June 26, 2012 (Landis 2012).

Wing Span	23.72 m (77 ft 10 in)
Overall Length	25.32 m (83 ft 1 in)
Overall Height	7.43 m (24 ft 4 in)
Gross Wing Area	86.83 m² (934.6 ft²)
Wing Leading Edge Sweep	31.7°
Maximum Takeoff Weight	31 615 kg (69 000 lb)
Long-Range Cruising Mach	0.77
Maximum Cruising Mach	0.85
Maximum Operating Altitude	13 720 m (45 000 ft)

TABLE II.5. G-III/SCRAT specifications.

II.2.2. *Flight experiment requirements*

LaRC, DFRC, and TAMU collaborated on the objective and requirements definition for the ERA Discrete Roughness Elements Laminar Flow Glove Experiment (DRELFGE) task, referred to in this document as SARGE.Complete ERA DRELFGE requirements are provided in appendix A. The top-level objectives and requirements relevant to the experimental design are summarized as follows (Belisle *et al.* 2011):

- For $Re_c \geq 15$ million, demonstrate NLF with $(x/c)_{tr} \geq 0.60$ on the suction side over 14 in of span. Demonstrate simultaneous NLF on the pressure side.
- For $Re_c \geq 22$ million, demonstrate the DRE control that extends laminar flow by at least 50% on the suction side beyond the natural transition location (e.g., if natural transition occurs at $x/c = 0.40$, then DREs will extend transition to $x/c = 0.60$).
- The section lift coefficient requirement for both regimes is $C_\ell \geq 0.5$ based on the local glove chord within the laminar-flow span. Additional requirements are that $\varLambda_{LE} \geq 30°$, $Re' \geq 1.4$ million/ft, and $M \geq 0.72$.
- Since the goal is to demonstrate passive LFC, passive appliqué DREs shall be used, as opposed to other techniques such as plasma actuators or microbubbles. These techniques may be considered in follow-on experiments.
- As crossflow instability is highly sensitive to surface roughness, especially in the leading-edge region, the leading-edge surface roughness shall be varied from approximately 0.3 μm RMS for a polished leading edge to 4 μm RMS for a painted or "operational" leading edge.

II.2.3. *Flight experiment design*

Belisle *et al.* (2011, 2012) describe the design of the flight test experiment; additional details on the flight experiment planning may be found in Tucker (2012) and flight instrumentation in Williams (2012). Following the G-II analysis in §II.1.2, 0.42%–0.58% of the semispan is a suitable location to place the wing glove. This location corresponds to BL198–BL270 In wing buttock line (BL) coordinates measured in inches from the aircraft centerline. The chordwise extent of the glove ends at the rear beam, allowing the pressure to be recovered smoothly before the G-III wing spoiler and flap surfaces. The glove location is notionally shown by a patch of matte black paint in figure II.8. On the pressure side of the wing, the glove truncates near to the leading edge of the host G-III wing. The design considers the potential for laminar flow to continue onto the host aircraft wing. The glove is rendered in figure II.9

The glove planform, shown in figure II.10, assumes the same conical planform as the host G-III wing, giving leading edge sweep for the glove $\varLambda_{LE} = 34.6°$. At all interfaces of the glove with the host wing, the design matches geometry, slope, and curvature. DFRC selected a floated glove design, drawing on experience with a similar structural design in the F-16XL supersonic HLFC experiment (Marshall 2000, 1999; Anders & Fischer 1999). The floated glove design necessitated a 2-inch glove-OML–wing-OML clearance to account for the glove structure and thickness.

FIGURE II.8. Patch on port wing of NASA SCRAT showing notional glove location (Landis 2010).

Belisle *et al.* (2011) describe the science flight envelope shown in figure II.11. The primary test condition is $M = 0.75$, $H = 38\,840$ ft, corresponding to $Re_c = 24.2$ million at the glove midspan section. The design C_p at the midspan corresponds to $AoA_{\text{aircraft}} \approx 3.5°$. The flow over the glove is first supercritical at $M_{\text{crit}} = 0.71$.

The flight test program consists of 36–47 data sorties totaling 74–97 flight hours, as described in Tucker (2012). The initial flights will refine the science envelope to establish the in-flight pressure distribution and *AoA* range. As a single point design, the *AoA* range where both sides of the wing glove can be expected to meet the project laminar flow requirements is narrow, as shown notionally in figure II.12. The difference between the maximum and minimum $AoA \approx [1, 2]°$. The flight conditions are defined in terms of a data band and a tolerance. The data band is the range of values that a particular parameter is considered valid. Within the data band, the tolerance is the range of variation tolerable for a specific points. The predicted data band and tolerances are tabulated in table II.6.

The research instrumentation suite will measure parameters including surface infrared (IR) signatures, static pressures, surface temperatures, boundary layer frequency spectra, and local glove flight conditions (Williams 2012), as shown on the suction side of the glove in figure II.13.

Figure II.9. SARGE wing glove rendering. (Rendered by M. Roberts using Flickr photo 2821470748 by D. Erickson.)
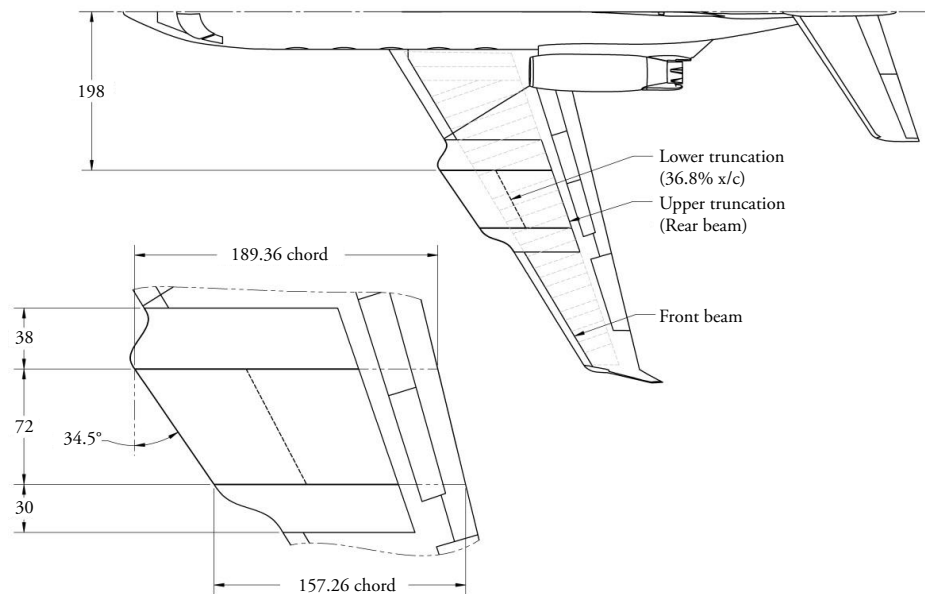
Figure II.10. Planform layout of the TAMU-06-05 wing glove (from Roberts *et al.* 2012). Dimensions are in inches.
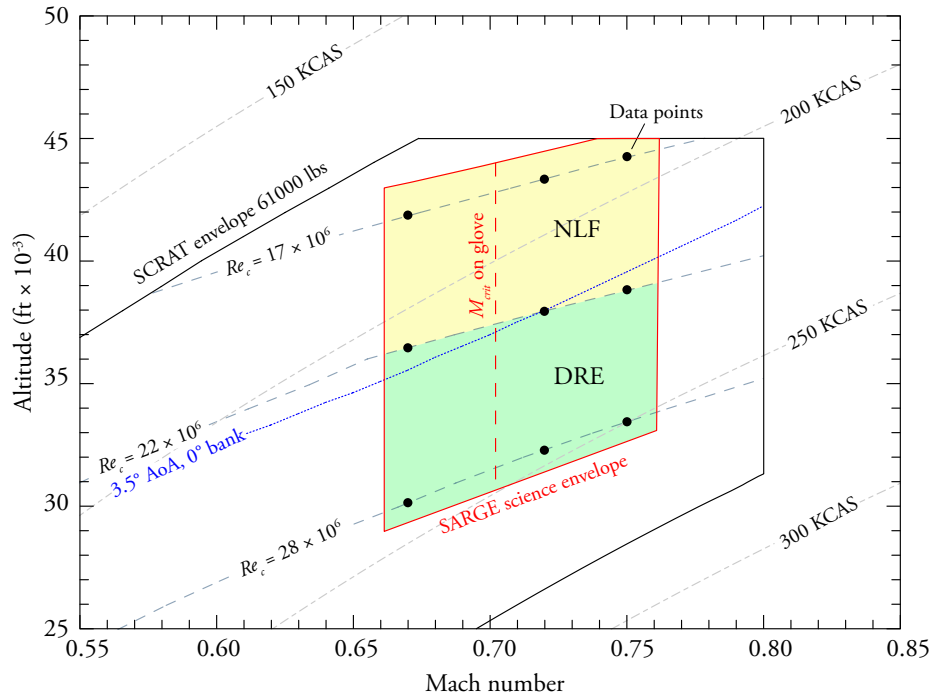
FIGURE II.11. SARGE experimental Mach-altitude science flight envelope (adapted from Belisle *et al.* 2012). Re_c is referenced to midspan glove chord (BL234) and KCAS indicates knots calibrated airspeed.
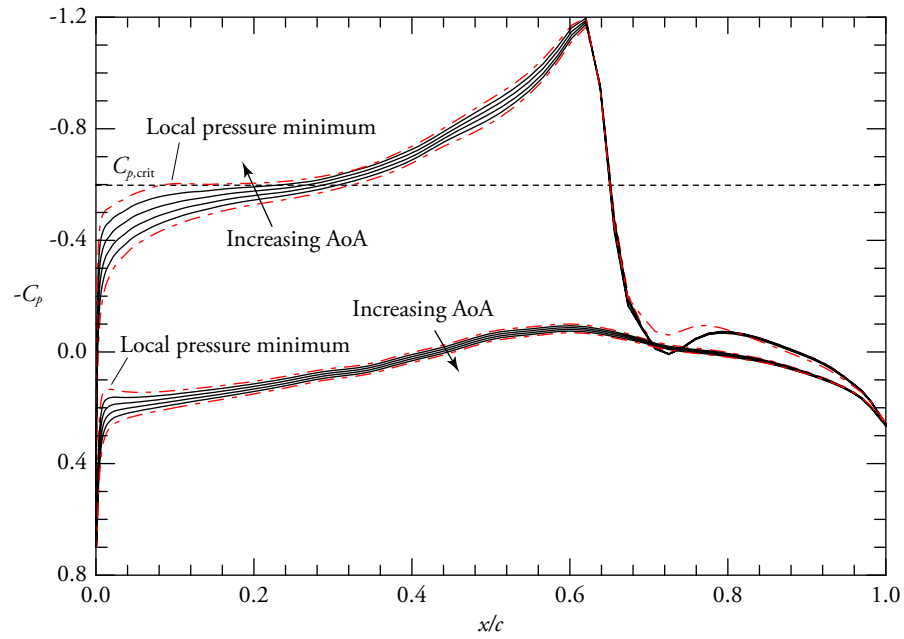
FIGURE II.12. Notional SARGE glove pressure distribution and *AoA* range (Belisle *et al.* 2011).

	Data band	Tolerance
Mach number	subcritical $[0.66, 0.70)$	± 0.01
	supercritical $[0.70, 0.76]$	
Reynolds number	NLF $[15, 30]$ million	$\pm 20\,000$
	DRE $[22, 30]$ million	
Angle of attack	$[AoA_{min}, AoA_{max}]$	$\pm 0.1°$
Angle of sideslip	$[-1°, +1°]$	$\pm 0.1°$

TABLE II.6. SARGE experiment flight parameter data bands and tolerances. The range between AoA_{min} and AoA_{max} is expected to be about 0.5°.
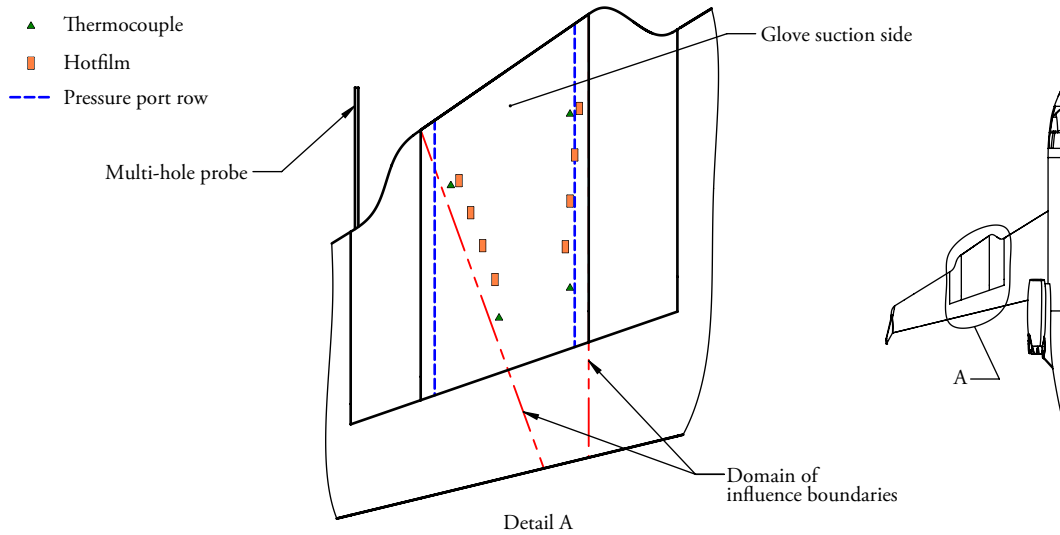
FIGURE II.13. Suction-side SARGE instrumentation; pressure-side instrumentation is similar (from Belisle *et al.* 2011).

IR SIGNATURES. A FLIR 8000 megapixel IR camera will be used to measure IR signatures on the glove surface. It is expected that the difference in adiabatic recovery temperature between laminar flow and turbulent flow will be on the order of 1°C at these flight conditions, sufficient to measure the transition location in level flight (Brandon *et al.* 1990). The camera will be installed inside the cabin and mounted on the port side of the aircraft with a view of the wing glove through a IR-transparent insert constructed to replace one of the emergency exit windows (figure II.7).

GLOVE PRESSURE MEASUREMENTS. Static pressure measurements will be made using two rows of through-surface static ports on the suction side and forward pressure sides of the glove, and strip-a-tubing on the aft pressure side of the G-III wing surface. These streamwise rows are located

approximately 6 inches from the inboard and outboard glove fairings.

SURFACE-MOUNTED INSTRUMENTATION. Surface-mounted thermocouples and uncalibrated hot films are the primary surface diagnostics. The surface-mounted thermocouples will provide boundary conditions for stability computations, in addition to being used a check on the IR thermography. Uncalibrated hot films will provide boundary layer frequency spectra that allow regions of laminar and turbulent flow to be identified.

LOCAL FLOWFIELD CONDITIONS. An air-data boom mounted local to the glove provides the local flowfield conditions in the vicinity of the glove. A 5-hole probe with a conical tip measures AoA, angle of yaw (AoY), total pressure (p_T) and static pressure (p_s). A differential pressure transducer connected to the p_T port at the tip and p_s ring around tube base provides dynamic pressure p_q. These parameters provide the local glove conditions for use in computational analyses.

WING DEFLECTION. DFRC developed a method to measure wing deflection using a single standard camera and a visual rule. The rule can be calibrated on the ground using known, measured deformations to ascertain both the wing deflection and twist in flight.

II.2.4. *Airfoil design and initial loft*

The initial glove loft, TAMU-05-04, is defined by the two airfoils described in table II.7: TAMU2D-04-Bl198 and TAMU2D-04-BL270 at the inboard and outboard extents of the glove, respectively. The initial loft marginally meets the project requirements of §II.2.2.

The flow over the glove is supercritical and exhibits a shock at the aft blending due to 3D effects that don't manifest in the 2.5D analysis. Figure II.14 shows a comparison of the C_p as predicted in both cases.

Transition predictions using LST on the 2.5D airfoils and the mid-span glove (table II.8) show that the initial loft marginally meets the ERA project requirements (§II.2.2).
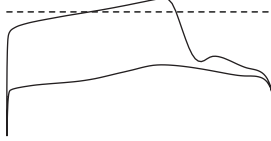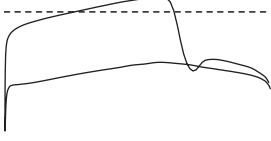
LST results on the gloved configuration suggest that $\lambda_1 = [3, 4]$ mm is a candidate DRE control wavelength to control the most unstable wavelength $\lambda_2 = [8, 10]$ mm.

Pressure isobars for the TAMU-05-04 configuration shown in II.15 exhibit significant spanwise non-uniformity. Such press distributions are not representative of an effective wing design and would be expected to have poor aerodynamic characteristics (Küchemann 1978). In addition, as elaborated in §II.2.6, this unsweeping of the isobars doesn't provide the uniform swept-wing crossflow profiles that are assumed for DREs control. The boundary layer solver, WINGBL2, assumes a locally infinite-swept-wing flow. The transition predictions in table II.4 would be expected to be representative only if spanwise uniformity approximated infinite- or conical-swept-wing flow.

Malik, Liao, Lee-Rausch, Li, Choudhari & Chang (2011) performed a companion assessment using LST and linear PSE analysis. They considered LST TS computations using constant wave angle rather than the constant wavelength computations carried out by TAMU. In the linear PSE analysis, they

	TAMU2D-04-BL198	TAMU2D-04-BL270
C_p		
Airfoil		
M (primary design)	0.75	0.75
Re_c (primary design)	22 million	22 million
c (streamwise)	4.8 m (16 ft)	4.0 m (13 ft)
H (ft)	40, 700	36 800
t/c (streamwise)	8.2%	8.8%
r_{LE}	18 mm @ $AoA_{2D} = 2.6°$	16 mm @ $AoA_{2D} = 2.7°$
Re_θ (Re_c = 30 million)	85	87
C_ℓ	0.50 @ $AoA_{2D} = 2.2°$	0.50 @ $AoA_{2D} = 2.4°$

TABLE II.7. SARGE initial loft airfoil section design summary.
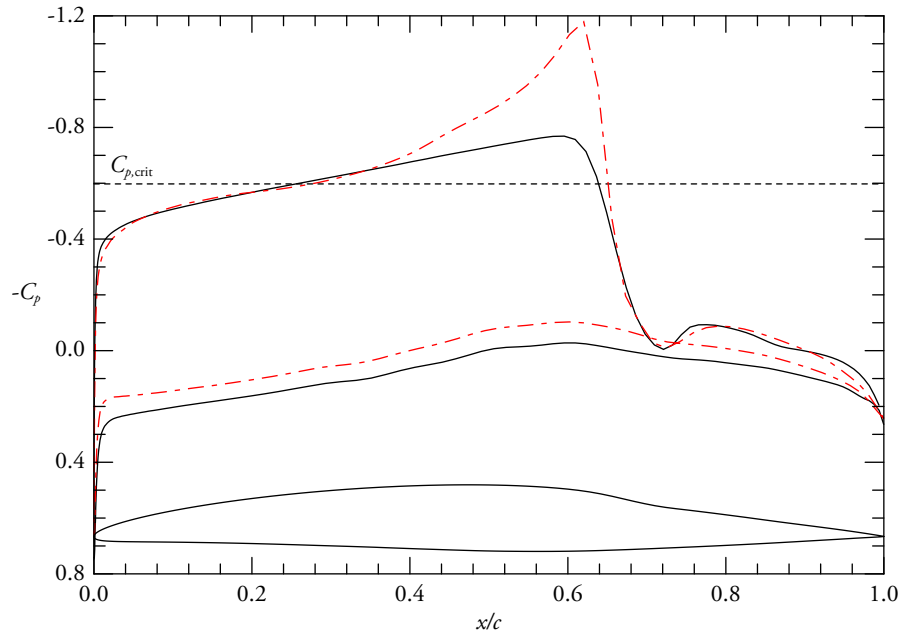
FIGURE II.14.   Infinite-swept-wing airfoil C_p compared to TAMU-05-04 mid-span glove section (BL234) C_p (Belisle *et al.* 2011). Conditions at primary design point, $M = 0.75$, $H = 38840$ ft. Solid line corresponds to 2.5D calculation at $AoA_{2D} = 2.3°$; red, dashed-dot line corresponds to 3D TRANAIR calculation at $AoA_{aircraft} = 3.5°$. Dashed line is critical C_p for $M = 0.75$.

			Suction side		Pressure side	
AoA_{2D}	C_ℓ	$Re_c \times 10^{-6}$	$(x/c)_{\mathrm{tr}}$	$Re_{x,\mathrm{tr}} \times 10^{-6}$	$(x/c)_{\mathrm{tr}}$	$Re_{x,\mathrm{tr}} \times 10^{-6}$
2.2°	0.50	18.0	≥ 0.58	≥ 10.4	0.45	8.1
2.2°	0.50	22.0	0.52	11.4	0.42	9.2
2.2°	0.50	30.0	0.40	12.0	0.36	10.1
2.6°	0.54	18.0	≥ 0.58	≥ 10.4	0.37	6.7
2.6°	0.54	22.0	≥ 0.58	≥ 12.8	0.32	7.0
2.6°	0.54	30.0	≥ 0.58	≥ 17.4	0.20	6.0

TAMU2D-04-BL198 infinite-swept-wing section

TAMU-05-04 lofted glove at BL234

			Suction side		Pressure side	
AoA_{aircraft}	C_ℓ	$Re_c \times 10^{-6}$	$(x/c)_{\mathrm{tr}}$	$Re_{x,\mathrm{tr}} \times 10^{-6}$	$(x/c)_{\mathrm{tr}}$	$Re_{x,\mathrm{tr}} \times 10^{-6}$
3.5°	0.5	17.5	0.49	8.6	0.43	7.5
3.5°	0.5	22.0	0.43	9.5	0.39	8.6
3.5°	0.5	27.5	0.35	9.6	0.34	9.3

TABLE II.8. Predicted transition locations on TAMU2D-04-BL198 and at the TAMU-05-04 midspan. Transition is assumed to occur at $N = 9$ for an operational leading edge finish.
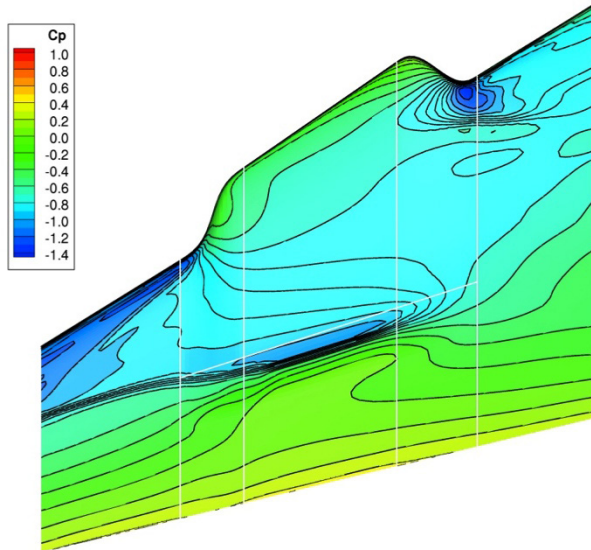
FIGURE II.15. Pressure coefficient contours on the suction side of TAMU-05-04 glove, wing, and fairings (from Belisle *et al.* 2011).

identified that for this specific design, the effect of curvature is substantially more stabilizing than the nonparallel effects. TS is also a concern for wave angles approximately $\psi \geq 20°$. In contrast, the G-II airfoil TAMU-003T-75 curvature and nonparallel effects were comparatively balanced and the design was also more stable to TS overall. TAMU-06-05, the improved design discussed in the next section, addressed this stabilization due to curvature satisfactorily.

Hartshorn (2011) considered the effect of the wing glove asymmetry on aircraft handling qualities and the ability of the aircraft to be trimmed. Nonlinear full potential and Navier-Stokes analyses identified only small, mostly insignificant changes in the aerodynamic forces. This obviates the need for a symmetric "dummy" glove would be required on the starboard wing, which was identified as a potential concern during the early planning phases.

II.2.5. *Shape optimization*

To address the aerodynamic issues of the initial loft that were discussed in the previous section, TAMU and DFRC embarked on a collaboration to develop a method to use inverse C_p matching techniques to optimize the shape of the glove using a fully 3D analysis (Hartshorn *et al.* 2012; Belisle *et al.* 2012). The primary objective in the optimization was to improve the spanwise uniformity of the pressure isobars in order to achieve efficient isobars more representative of conical flow.

The method is implemented in TRANAIR, a nonlinear full potential code originally developed in a collaboration between NASA and Boeing (Samant, Bussoletti, Johnson, Burkhart, Everson, Melvin, Young, Erickson, Madson & Woo 1987) that has been extended with the coupled, integral boundary layer from ISES (Boeing 2007; Drela & Giles 1987*a*,*b*) and a nonlinear elimination method for aerodynamic design optimization that incorporates the NPSOL sequential quadratic programming algorithm for general nonlinear problems (Young, Huffman, Melvin, Hilmes & Johnson 2003; Gill, Murray, Saunders & Wright 1998). TRANAIR provides an appropriate balance of fidelity, solution control, and automation that make it an idea code for use during the design phase.

The process uses optimization techniques to match the target C_p in figure II.16 and follows that used by Bogue & Crist (2008). The geometry is parameterized using the class-shape transformation (CST) of Kulfan (2007). Using the class-shape transformation, an airfoil is represented as the combination of a class function that defines the type of body (say, airfoil-like or fuselage-like) and a shape function that transforms the class into a specific shape. Compared to other options for parameterization the CST is notably more efficient, requiring only 5-10 unknowns for general airfoil shapes, as opposed to dozens for discrete points. Or, when compared to using the control points of a B-spline curve as the parameters the CST is less prone to impractical and unphysical shapes Kulfan & Bussoletti (2006). When optimizing five airfoil sections in 3D, the reduction in the number of parameters is significant.

The resulting design, TAMU-06-05, is much improved over the initial loft, at least to approximately $x/c = 0.3$ as shown in figure II.17. This is the glove design used in the SARGE PDR conducted at DFRC in June 2012.
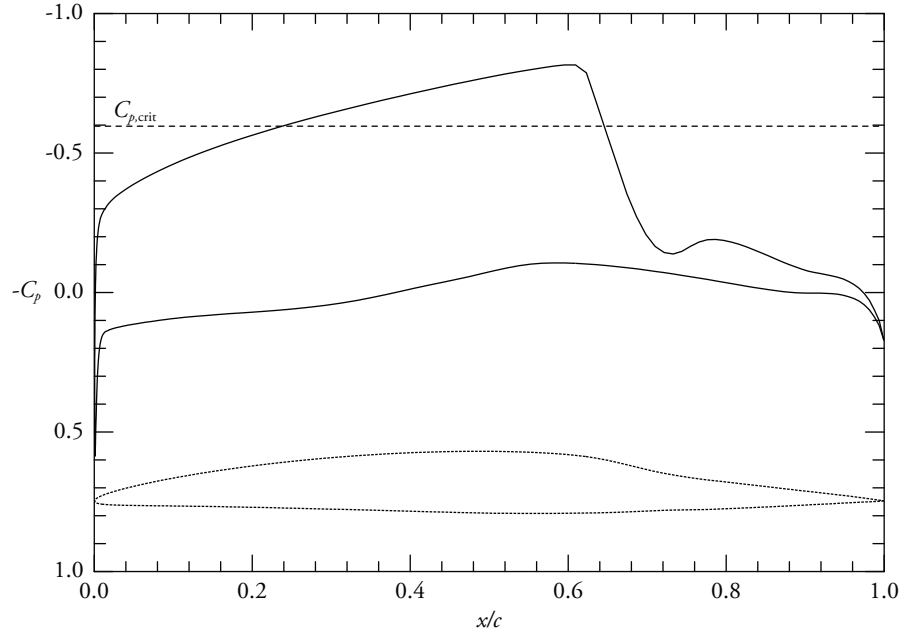
FIGURE II.16. Target C_p used in TAMU-06-05 optimized glove (solid line) along with notional airfoil (dotted line) (Hartshorn *et al.* 2012).
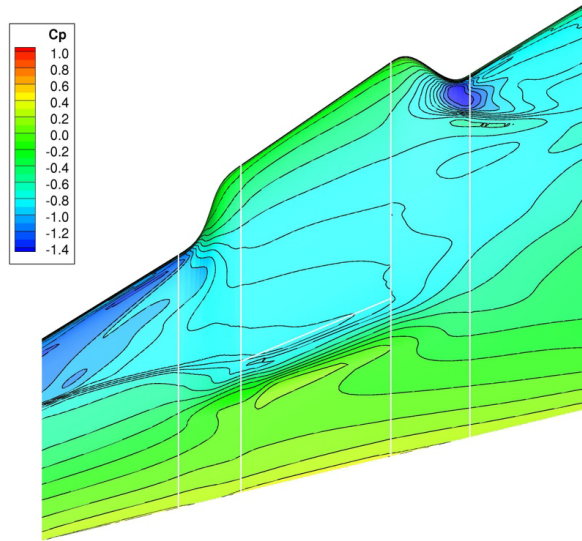

FIGURE II.17. Pressure coefficient contours on the suction side of the optimized TAMU-06-05 glove, wing, and fairings (from Belisle *et al.* 2012).

Belisle, Roberts, Williams, Tufts, Tucker, Saric & Reed (2012) report the final design transition predictions on the target C_p and optimized glove loft, tabulated in table II.9. The apparent agreement is quite good; unfortunately, this agreement is deceptive. Higher-fidelity results in the following section identify issues that necessitate further design refinement.

			TAMU2D-05 target C_p				
			Suction side			Pressure side	
AoA_{2D}	C_ℓ	$Re_c \times 10^{-6}$	$(x/c)_{tr}$	$Re_{x,tr} \times 10^{-6}$		$(x/c)_{tr}$	$Re_{x,tr} \times 10^{-6}$
n/a	0.49	15.0	0.32	5.6		0.40	6.0
n/a	0.49	22.0	0.25	5.5		0.36	7.9
n/a	0.49	30.0	0.18	5.4		0.29	8.7

			TAMU-06-05 lofted glove at BL234				
			Suction side			Pressure side	
$AoA_{aircraft}$	C_ℓ	$Re_c \times 10^{-6}$	$(x/c)_{tr}$	$Re_{x,tr} \times 10^{-6}$		$(x/c)_{tr}$	$Re_{x,tr} \times 10^{-6}$
3.4°	0.51	16.5	0.32	5.3		0.45	7.4
3.4°	0.51	24.2	0.23	5.6		0.38	9.2
3.4°	0.51	27.5	0.20	5.5		0.36	9.9

TABLE II.9. Predicted transition locations on optimization target C_p TAMU2D-05 and at the TAMU-06-05 midspan. Transition is assumed to occur at $N = 9$ for an operational leading edge finish.

II.2.6. *Full-aircraft CFD and linear stability*

A full-aircraft, viscous Navier-Stokes analysis, as carried out by Roberts, Reed & Saric (2012) and Roberts (2012), provides the authoritative assessment of the design and mission success. Although spanwise uniformity was a primary purpose in the optimization process, it is clear that the TAMU-06-05 design significantly fails to achieve a efficient aerodynamic design.

LST results computed out using viscous boundary layer profiles by Roberts *et al.* (2012) and verified by Malik, Liao, Li & Choudhari (2013) demonstrate a particular consequence of this design: the isobar unsweep results in significant discrepancy between the assumption of an infinite swept with made by the WINGBL2 boundary layer solver and the actual case when using viscous profiles. The viscous profiles exhibit substantial crossflow stabilization when compared to the boundary-layer solver results.

This result means the experimental objectives–namely, providing the conditions for a sufficient crossflow growth to demonstrate DRE control–would be unlikely to be met by this design. Since an operational wing would not generally be designed with isobars similar to these, the design is not

representative of practical application. Tufts, Reed & Saric (2013) completed improvements in a follow-on design that address this issue.

Roberts *et al.* (2012) also found that reducing the Mach number results in a pressure coefficient that flattens out significant as the Mach number decreases. This can be expected to destabilize TS, likely resulting in earlier transition at lower Mach, when all other conditions are held constant. If laminar flow demonstration Mach numbers lower than the design were a priority in the experimental program, then a multi-point would likely be necessary.

II.2.7. *Nonlinear PSE and secondary instability analysis*

Malik, Liao, Li & Choudhari (2013) performed nonlinear PSE and secondary instability analysis on the TAMU-06-05 design to qualitatively assess DRE effectiveness. They report that DREs may delay transition by at least 20% and have the potential to stabilize travelling crossflow in addition to stationary.

However, a number of simplifying assumptions limit the amount of faith that can be placed in the results. For instance, the initial amplitudes of the disturbances are unknown and depend substantially on the actual test article and flight environment. The actual conditions will likely result in DREs being substantially more or less effective than predicted by these results.

CHAPTER III

AERODYNAMIC DESIGN FOR SWEPT-WING LAMINAR FLOW

There are a few reasons why the SARGE design described in chapter II reflected an evolutionary process. First, the design requirements changed repeatedly during the course of the design, as shown in figure II.2. Second, as each design was analyzed in detail, shortcomings in the process were identified that required improved methods. Third, by Küchemann (1978), "the impression that design of aircraft is as much an art as a science ... probably corresponds to the real situation."

Following from the last point, there is no widely published process for wing design that is proven on operational aircraft. What methodology does exist in the field is likely to be proprietary and, even within the design departments of a particular manufacturer, is likely to vary appreciably depending on the specific vehicle under consideration or the proclivities of the individual designer responsible for the design.

A few authors have attempted to lay the groundwork for aerodynamic design as applied to general cases. Perhaps the most thourough book on the topic is Küchemann (1978), the culmination of a life's work by the principal aerodynamic designer of the Aérospatiale-BAC Concorde supersonic airliner. Ryle (1970) describes the specific methodology for a parametric design process in use by the Lockheed Georgia Company at the time and is still relevant today, even though the available computational tools today are much more advanced. Obert (2009) is a modern treatment based on course notes by the head of preliminary design at Fokker Aircraft Company and includes much useful data.

None of these works apply aerodynamic design to SWLFC wings specifically, which may be one of the most challenging unsolved problems in aerodynamic design. This chapter describes details of aerodynamic design specific to SWLFC wing design and evaluates a set of design methods available in 2013. Although specific to the design of the SARGE wing glove, the methodology can be extended to more general test article and wing designs.

This chapter first provides an overview of a general design philosophy for SWLFC, then assesses the approaches and processes employed throughout the course of the SARGE design, and finally recommends a process to follow in future designs.

III.1. General design philosophy

In a full-aircraft design, the typical primary (independent) design variables are listed in table III.1 (Ryle 1970). Although these variables have been essentially unchanged for decades (Raymer 2002), with modern computational tools proxy variables are often used for the traditional ones. For example, a traditional carpet plot (e.g., figure III.1) might have shown W as a function of T/W and W/S. If T/W

and W/S are used as inputs, then it is necessary to iterate on W until a value is found that matches the inputs. If the problem is formulated such that W is a function of T and S directly (in addition to the other relevant parameters), then the output W can typically be determined directly with minimal iteration, if any. Modern multidisciplinary optimization tools often will use such an approach to reduce the amount of iteration necessary to analyze a particular design configuration.

Wing loading	W/S
Thrust-to-weight ratio	T/W
Aspect ratio	$A\!R = b^2/S$
Wing sweep	Λ
Wing thickness ratio	t/c
Cruise Mach number	M_{cruise}
Wing taper ratio	$\lambda_w = c_r/c_t$

TABLE III.1. Typical primary aircraft design variables. W is the aircraft weight; T is the total engine thrust; b is the wing span; S is the wing theoretical planform area; t is the average wing thickness; c is the average wing chord; and c_r and c_t are the wing planform root and tip chords, respectively (Ryle 1970).

In the SARGE design, many of these full-aircraft requirements and considerations that complicate a wing design are relaxed due to the specification of the mission as a TRL 5 flight experiment. Mankins (1995) defines TRL 5 as "component and/or breadboard validation in relevant environment," contrasted with TRL 6, "System/subsystem model or prototype demonstration in a relevant environment (ground or space)." The distinction for a wing can be considered one of operational relevance: at TRL 6, a complete test article should be representative of a wing design for an operational aircraft. The Northrop Grumman AEI flight test is an example of a TRL 6 effort, where Drake & Solomon (2010) flight tested a scale model that produced pressure distributions representative of a section of a SensorCraft wing design.

For a TRL 5 demonstration, the emphasis is on the demonstrating the technology in a relevant environment and it is not necessary to include all of the parameters that ensure immediate relevance to an complete aircraft system design. For the purposes of this dissertation, the relevant primary design variables are reduced to the following four variables: Λ_{LE}, M_{design}, t/c, and C_ℓ (where C_ℓ is a proxy for W/S). The secondary design variables are Re_c and Re'. This simplifies the design process significantly by neglecting considerations such as applicability to an operational system or full-vehicle aerodynamic performance at off-design conditions such as takeoff and performance (beyond that required for safe experimental aircraft handling qualities). The objective in this experiment is to demonstrate a physical concept to advance the prospects for passive laminar flow on operational, swept wing aircraft at high
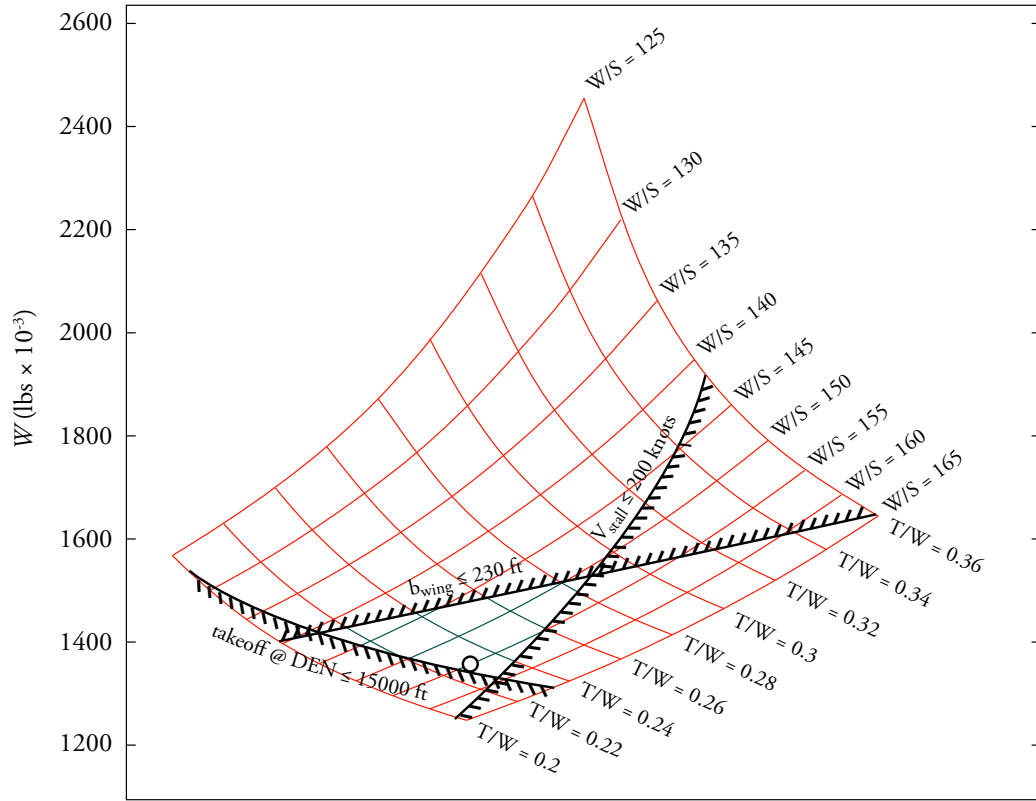
FIGURE III.1. Carpet plot at $A\!\!R = 7$ from an 800-passenger conceptual undergraduate senior project design (from Belisle, Martinez, Baumes, Rose & Salem 2005).

Reynolds numbers.

Even though there is not necessarily a specific operational vehicle at this level of technology maturation, choosing parameters that are notionally relevant to a target application enhances the value of the research. The parameters for SARGE in table III.2 are notionally relevant to a subsonic transport aircraft such as the Boeing 737-600 (Brady 2013; Boeing 2006).

In order to ensure a successful experiment that demonstrates the ability of DREs to delay transition on a swept wing, transition at the design condition must be due to crossflow and not one of the other instabilities present on a swept wing (§I.2). The design first controls or eliminates streamwise and attachment-line stabilities, then focuses on strategically shaping the pressure distribution in order to encourage crossflow growth such that shorter wavelengths grow sufficiently and early enough such that they may be strategically excited in order to control the most unstable wavelength that would naturally trigger transition.

Attachment and streamwise instabilities may be an issue, but can be eliminated through well-established design principles. As shown by Bassom & Hall (1991), Görtler instability is not likely

	ERA DRELFGE Requirements	Boeing 737-600	SARGE TAMU-06-05
Λ_{LE}	$\geq 30°$	$27.2°$	$34.5°$
M	≥ 0.72	0.785 (typical cruise at $H = 35\,000$ ft)	0.75 (max design)
t/c	$\geq 10\%$ (derived)	12.89%	8.5% (average)
$C_\ell \| C_L$	$C_\ell \geq 0.5$	$C_L \approx 0.65$	$C_\ell = 0.5$ (average)
Re_c	≥ 15 million (NLF) ≥ 22 million (DRE)	23.4 million (*MAC*, typical cruise)	$[15,22]$ million (NLF) $[22,30]$ million (DRE)
Re'	≥ 1.4	1.9 million/ft (typical cruise)	$[1.1,2.0]$

TABLE III.2. Design parameter comparison. ERA DRELFGE requirements are from Baumann (2011). Boeing 737-600 data are calculated from Boeing (2006) and Brady (2013).

to be an issue in the presence of appreciable crossflow, i.e. leading-edge sweep angles greater than about 20°and is thus neglected here since concave curvature, if any, is slight in the glove design. Traveling crossflow appears to be of minimal concern in flight (Saric *et al.* 2011); even it if does appear, Malik *et al.* (2013) qualitatively suggest that DREs may act on travelling crossflow as well as stationary, although such an effect remains to be proven experimentally. The design focuses principally on addressing three instability mechanisms believed to be relevant to this case: attachment-line, streamwise, and stationary crossflow.

III.1.1. *Control attachment-line instabilities*

Referring to §I.2.2, attachment-line instabilities are controlled by placing a constraint on the leading-edge radius r such that Re_θ, the attachment-line momentum thickness Reynolds number, is less than 100. Although in principle the inboard fairing acts as a Gaster bump and eliminates attachment-line contamination from the G-III wing and would allow the SARGE to operate at least $Re_\theta < 250$, the more restrictive criteria is conservatively chosen to maintain relevance to a full-wing design and ensure that the attachment line remains fully laminar across the SARGE test section.

III.1.2. *Mitigate streamwise instability*

When considering natural or passive LFC, it inadvisable to work at the margins of streamwise instability (Saric & Reed 2004). Therefore, an airfoil conducive to LFC by DREs should feature uniformly accelerated flow so that TS waves are controlled where the *N*-factors remain well below $N \approx 6$ as opposed to the typical assumption that transition will occur for $N \approx 9$. Consideration should be made to recognize that issues such as manufacturing imperfections and engine noise may excite TS, and hence a generous margin is desirable.

Imposing a sufficiently accelerating pressure gradient, as established using LST computations,

produces a flow that constrains the growth of streamwise instabilities. The pressure gradient should be favorable as far aft as possible, which may be limited due to practical considerations including the following:

1. Pressure recovery before the control surfaces, where transition can be assumed to occur due to gaps between the wing and the control surface;
2. Permissible steepness of the pressure recovery to avoid a recovery shock when the flow is transonic.

The problem of avoiding a recovery shock, which carries with it a drag penalty, becomes more challenging when 3D wing effects are included and as $M \to 1$. J. Koenig of Airbus Industrie notes that for a practical wing design "with current technologies, we don't see any possibility to stretch the area of laminarity any further than 60%" (Gubisch 2011).

In this work, streamwise instability calculations are performed with constant $\beta = 0$ and typically $f = [0.3, 10]$ kHz. Although it would perhaps be advisable to compute streamwise instability using constant $\psi = 0$ rather than constant β (Malik *et al.* 2011), version 2.0 of the LASTRAC code used in this work does not support this computation.

III.1.3. *Encourage crossflow growth and allow for DRE control*

With wing sweep, a favorable pressure gradient naturally excites crossflow instability, a key distinction to be remembered in passive SWLFC design when compared to NLF design at low sweep where crossflow is not an issue. Shaping the pressure gradient reflects a balance between the stabilization or destabilization of these two competing mechanisms. In the DRE approach, the idea is to stabilize streamwise instability using a favorable pressure gradient. If the pressure gradient generates appreciable crossflow growth, then DREs are used to delay transition past the natural, uncontrolled location.

In order for DREs to be an option, the gradient needs to be designed to allow their use; one cannot generally expect to apply DREs to an existing design. Referring to a notional LST N-factor computation in figure III.2, transition is expected to be caused by the most-unstable wavelength, in this expected to be in the range $\lambda_2 = [6, 8]$ mm for $N_{tr} = [9, 14]$.

A candidate control wavelength, $\lambda_1 = 4$ mm, is chosen because it grows to about $N = 6$ by about $x/c = [0.2, 0.3]$ and then decays. This wavelength could potentially be excited strategically to reduce the growth of the longer wavelengths without causing transition on its own. Prospective locations to place the DREs may be downstream of the branch I neutral point (the location where the wavelength first becomes unstable) for λ_1 or λ_2. In this case, the location is $x/c \approx 0.003$ for λ_1 and $x/c \approx 0.008$ for λ_2. In dimensional terms, this represents a difference of as little as 20 mm (0.8 inch) between the two values, which emphasizes the necessity of confidently determining the neutral stability point, as well as maintaining a constant flight condition where the attachment line can be predicted consistently by computations.
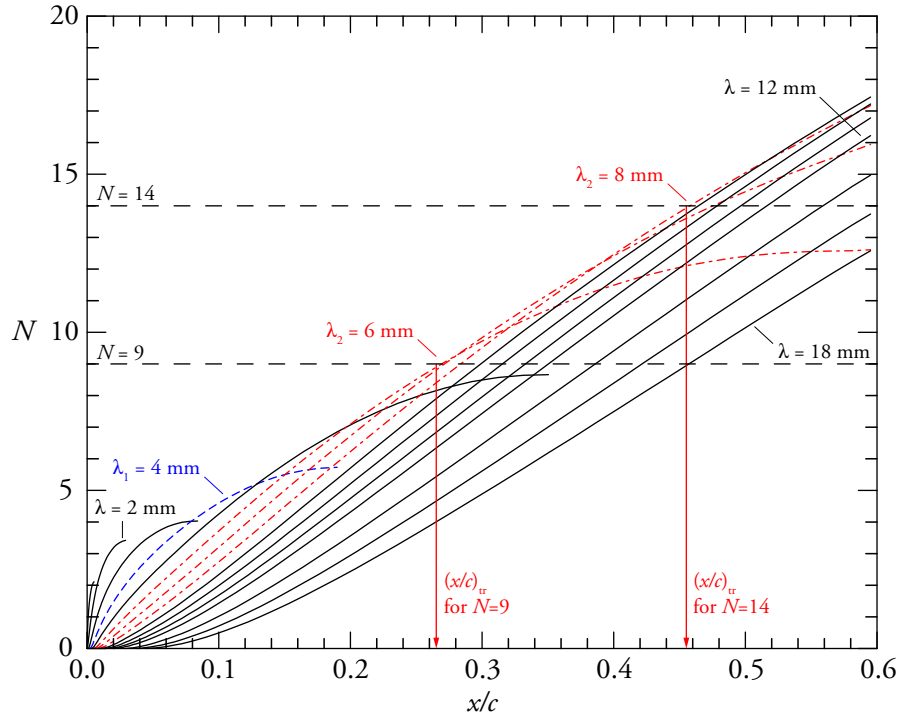
FIGURE III.2. LST N-factors for stationary crossflow ($f = 0$) at $M = 0.75$, $Re_c = 22$ million ($c = 4.4$ m, $H = 43\,610$ ft) calculated on target C_p described in §II.2.5. Dashed-dot red line refers to most unstable wavelengths λ_2 for range of expected critical N factors that might trigger transition. Dashed blue line refers to candidate DRE control wavelength (λ_2).

III.1.4. *Aerodynamic properties and other constraints*

It is impractical to specify generic aerodynamic aims that are generally applicable to all laminar flow designs, as aerodynamic design goals generally do not exist independently of mission requirements and non-aerodynamic constraints. As noted by Küchemann (1978), one can only specify aims when a specific design study is carried out.

The aerodynamic aims here are therefore specific to the SARGE wing glove design. First, the final design must fulfill meet all of the project requirements specific in appendix A. However, these requirement do not address aerodynamic design consideration. As noted, it is not necessary in SARGE to consider all the issues that would be required were it to be a wing design for an operational aircraft. Minimimal consideration (beyond that required for safe flight qualities) is given to issues such off-design conditions, takeoff and landing, and pitching moments that often drive a full aircraft wing design.

Before $C_\ell = 0.5$ became a requirement, the design sought to avoid supersonic flow entirely. In 2.5D airfoil design with a modest $C_\ell \geq 0.3$ at $M = 0.75$, this was not such a concern for approximately $t/c < 0.09$, which seemed to be feasible with a modest glove extension ahead of the G-III wing. When

the lift requirement increased, this objective became more of a challenge within practical structural and aerodynamic limits. When lofted into a 3D wing glove and the totality of 3D effects were considered, a supercritical airfoil appeared to be unavoidable. Practically, supercritical flow should not be concern, as Anderson (2011) notes that most modern transonic transport aircraft wings today are supercritical. Supercritical wings are generally considered to an effective configuration choice when compared to a comparatively thinner, subcritical airfoil. Mack (1979) demonstrates that local regions of supersonic flow are not a concern for laminar flow stability on a swept wing design.

If the design is supercritical, then a recovery shock should be avoided or minimized, since an issue like a transient shock could change the circulation and hence the properties of the upstream flowfield. Unfortunately, 2.5D analysis of isolated wing buttline cuts cannot be expected to accurately calculate the shock strength or location for the glove when lofted into a 3D glove. In addition, the grid needs to be refined in the vicinity of the expected shock in order to capture it accurately. TRANAIR (§III.2.1) includes automated adaptive gridding to substantially reduce or eliminate the grid refinement iteration that would be necessary if a grid were generated by rote.

III.2.   Design process overview

Broadly, there are two design processes applicable to the SARGE wing glove:

1. A "traditional" wing design process, i.e. choosing an appropriate number of buttline cuts and designer-directed iteration between a higher-order and lower-order geometry modification and analyses
2. Optimization by specification of a target pressure distribution that should be achieved across the span of the test section

The traditional wing design process in figure III.3(*a*) is a simplified representation of a process similar to that of Ryle (1970). This process was followed for the initial phases of the design up to the release of the TAMU-05-04 configuration. The optimization process (figure III.3*b*) took this initial glove configuration and attempted to improve the spanwise uniformity and match a consistent 2.5D pressure distribution across the entire span of the wing glove, including full aircraft effects such as the engine pressure field.

The basic tenets of the two processes are similar. In either case, the starting point in the process is a 2.5D infinite swept airfoil design. The host aircraft wing, along with conditions selected to be representative of the target high-subsonic transport aircraft, impose basic constraints on the design such as M and t/c. As the wing glove is an inherently 3D problem, specific results from 2.5D computations are of limited utility in demonstrating mission success. These 2.5D calculations principally facilitate the development of feasible laminar flow pressure distributions, provide insight into geometry perturbation sensitivities, and define the buttline cuts for a 3D loft.
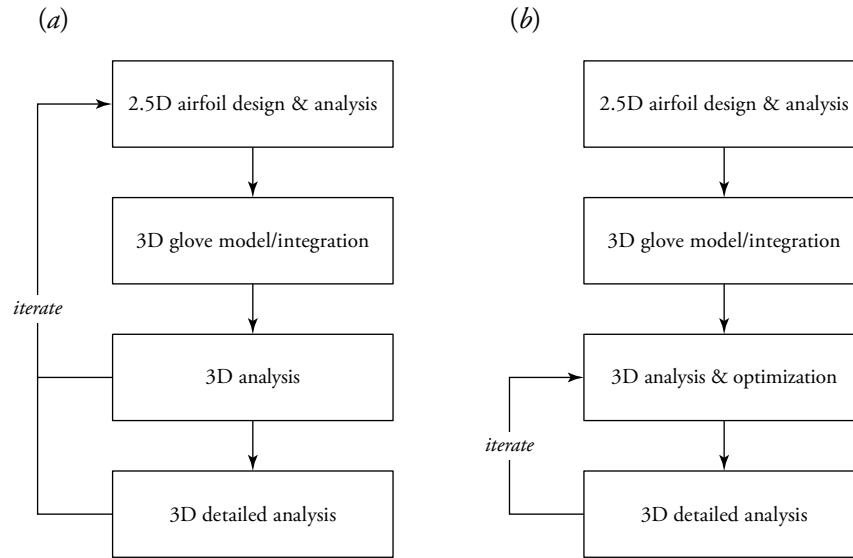
FIGURE III.3. Wing design processes: (*a*) Traditional process; (*b*) 3D optimization process.

One should not define so many spanwise cuts to make the 2.5D design problem impractical, but perhaps one should one not too parsimonious either. Two buttline cuts along with curvature-continuous fairings and the G-III trailing edge geometry defined the TAMU-05-04 loft. In contrast to a design such as the ELFIN F100 NLF glove (§I.3.2) where the glove was defined by a total of eight cuts—three on the inboard fairing, three on the wing glove test section, and three on the outboard fairing—two cuts may have been too few. The optimization process for TAMU-06-05 attempted to match the pressure distribution at least five cuts.

Once the 2.5D design and analysis converges, these buttline cuts are lofted and integrated into the full aircraft configuration. The first 3D analysis establishes a baseline for the design. For boundary layer stability analysis, assuming a locally infinite swept wing permits rapid analysis of basic boundary layer stability characteristics much in the same manner as the 2.5D calculations. Due to inherent limitations of the 2.5D analysis, most likely this initial 3D analysis will identify areas needing improvement. Progressing to 3D detailed analysis (fully viscous boundary layers) would be wasteful on the first iteration.

In the traditional process, an iteration returns back to modify the initial geometry, with corresponding 2.5D calculations if necessary. Once new cuts are decided upon, the cuts are lofted into a new 3D glove an the 3D analyses repeated. Once the design converges using the basic 3D methods, a initial detailed analysis with fully-viscous boundary layers (Roberts 2012) is performed to identify potential 3D and viscous effects that the basic analysis doesn't capture. If issues are noted, then the process returns again to the beginning by modifying the buttline cuts and relofting.

The optimization process modifies the traditional process by automating the process of modifying the geometry after the initial loft. A design tool such as TRANAIR is used to perturb the geometry towards the minimization of an objective function, as developed for SARGE by (Hartshorn *et al.* 2012). The objective function was to match a target pressure distribution C_p across the wing glove. The target pressure distribution may be developed much in same manner as a 2.5 airfoil by omitting the determination of a physical airfoil corresponding to a given C_p (§III.4). As with the traditional process, once the design reaches a certain level of maturity, a detailed analysis is performed. If the detailed analysis identifies issues with the design, the iteration loop returns to 3D analysis and optimization.

III.2.1. *Freestream*

Küchemann (1978) posits three levels of fidelity in computing a flow solution:

1. Obtaining accurate numerical solutions of the complete equations
2. Simplification of the equations
3. Linearization of the equations for small perturbations

Note the first necessarily always involves assumptions: the "complete" equations are never really solved. The Navier-Stokes equations as commonly solved in fluid mechanics, for instance, are possible only by assuming a continuum flow and neglecting various physical processes (e.g., intermolecular forces) that are insignificant for typical application to aircraft design. The third item, linearization, is useful in the present design for the solution of stability equations and geometry manipulation, but of limited utility as a meanflow solution for the reasons described in §III.3.1.

In principle, it is possible to solve the full Navier-Stokes equations directly using the Direct Numerical Simulation (DNS) approach. Such an approach would calculate transition and turbulence directly and would give the most accurate results given the current theoretical state. Although DNS is playing an increasingly important role in transition investigation (Reed 2008), current computational technology limits the practical applicability of this approach beyond Reynolds numbers of a few million. DNS on a complete aircraft configuration is currently out of the question. DNS also requires specification of initial conditions, which may not be fully determined without a completed design and measurements of the flow environment. Hence, even with the initial assumptions that form the Navier-Stokes solution, a DNS solution is impractical.

Judicious simplifications render design and analysis practicable. A starting point for a 3D wing design is to assume that a section far from the wing root or tip represents a conical flow, which in this work is further constrained to the infinite swept wing as previously described. This is a reasonable assumption for a laminar flow design, which often benefit from high aspect ratio wings by reducing the local Re_c for a given wing loading. Additionally, DREs to date have only been demonstrated on infinite swept wings and some risk reduction is achieved by constraining their application to this case.

In a short-span wing glove like that under consideration here, 3D effects can be expected to be significant. 2.5D calculations are useful only in the sense that they permit rapid iteration to narrow the design space that needs to be considered in 3D, where computations are more complex and time-consuming. In the SARGE design, the full-aircraft, viscous computations exhibited features that did not manifest in isolated 2.5D computations. The initial glove loft produce spanwise isobar nonuniformities. The design marginally met the requirements at the midspan location only—if one assumes locally infinite swept wing flow and uses a direct boundary layer (DBL) method to calculate the boundary layer profiles as described below. As shown by Roberts *et al.* (2012) and Liao *et al.* (2012), this assumption is not valid for this case, even after the design was improved through optimization efforts in Hartshorn *et al.* (2012) and Belisle *et al.* (2012).

Care must be taken to remember the limitations of the simplified methods and report results appropriately. Perhaps due to ingrained habits, some researchers (some covered in §I.3) have used approximations such as linearized potential codes and isolated 2D computations exclusively in the design process. For laminar flow design, such lower-order methods are largely unsuitable when used in isolation. When such a design progresses to wind tunnel or flight test or analysis using higher-order methods, surprises are common when an assumption of the method is violated by the actual situation.

Assuming 2013 computational methods and technology, the SWLFC design process recognizes that the authoritative computational check on the design is a viscous, full-aircraft Navier-Stokes solution with sufficient resolution in the laminar boundary layer to extract boundary-layer profiles directly from the Navier-Stokes solution. This solution is labor and computationally intensive, requiring days to weeks to grid the configuration, compute a solution, and fully analyze the results. It is impractical to iterate in a typical design timeline more than a few times with this level of detail, although Liao *et al.* (2012) are striving towards a laminar-flow design methodology that uses such detailed solutions intensively.

Table III.3 summarizes the design tools that were available and suitable for use in the SARGE design, ranks them in order of fidelity, and estimates the amount of time involved in computation a solution. Properly used, the comparatively simpler computations reduce the amount of iteration necessary in the more expensive, higher-fidelity computations. They advance the design towards a workable solution where the assumptions in the methods should become more valid as the aerodynamic design improves and undesirable flow behavior is mitigated.

By iterating primarily with lower-order methods mixed with occasional detailed analysis, the designer can find insights about what can be expected to happen with a particular design change without having to do a complete analysis—even if the solution in the lower-order method isn't strictly correct or useable to establish the maturity of the design in meeting the mission requirements.

Consider LST analysis using a DBL solution as an example, which is the primary approach used in this work. Fundamentally, these analyses can be used to establish which pressure distributions may be conducive to laminar flow. As a strip-wise method, each inner solution at one BL cut is independent of

Method	Configuration time (initial)	Configuration time (iteration)	Computational time (2013)	Example code
2.5D isolated airfoil				
1. Linear-vorticity panel	Seconds	Seconds	Seconds	XFOIL
2. Inviscid Euler	Hours	Minutes	Minutes	FLUENT, FUN3D
3. Full nonlinear potential*	Minutes	Seconds	Seconds	TRANAIR
4. Viscous Navier–Stokes	Hours–Days[†]	Minutes	Minutes–Hours[†]	FLUENT, FUN3D
3D full configuration				
5. Inviscid Euler	Days	Days	Hours	FLUENT, FUN3D
6. Full nonlinear potential*	Days	Hours	Hours	TRANAIR
7. Viscous Navier–Stokes	Days–Weeks[†]	Days	Days	FLUENT, FUN3D

* With automated, adaptive gridding and boundary-layer coupling
[†] Range depends on refinement desired in boundary layer

TABLE III.3. Available flow solution methods and approximate configuration and computation time in 2013, in order of increasing fidelity. Configuration time assumes modification of an existing case.

the solutions at the other BL cuts. For aerodynamic and boundary-layer stability reasons—in addition to consistency with the boundary-layer solution assumptions—spanwise uniform isobars are desirable in the design. If the design has spanwise uniform isobars that approximate infinite swept-wing flow (as in the successor design of Tufts *et al.* 2013), then the stability results using a DBL method should approach those using boundary-layer profiles from the Navier–Stokes solution.

The computations in this work can be broken into two broad categories as in table III.3: infinite swept wing (2.5D) and full-configuration 3D methods as described in the following sections.

INFINITE SWEPT WING. The infinite swept wing or 2.5D assumption results from the fact that the z-momentum equation can be decoupled from the x- and y-momentum equations, as first described by Prandtl (1946). Starting from the steady, incompressible Navier-Stokes equations (§I.1) are formulated normal to the leading edge of an infinite swept wing, changes in the z-direction are assumed to be small compared to changes in the x or y directions (i.e. $\partial/\partial z = \partial^2/\partial z^2 \approx 0$):

$$\frac{\partial u}{\partial x} + \frac{\partial v}{\partial y} = 0$$

$$u\frac{\partial u}{\partial x} + v\frac{\partial u}{\partial y} = -\frac{\partial p}{\partial x} + \frac{1}{Re}\left(\frac{\partial^2 u}{\partial x^2} + \frac{\partial^2 u}{\partial y^2}\right)$$

$$u\frac{\partial v}{\partial x} + v\frac{\partial v}{\partial y} = -\frac{\partial p}{\partial y} + \frac{1}{Re}\left(\frac{\partial^2 v}{\partial x^2} + \frac{\partial^2 v}{\partial y^2}\right)$$

$$u\frac{\partial w}{\partial x} + v\frac{\partial w}{\partial y} = \frac{1}{Re}\left(\frac{\partial^2 w}{\partial x^2} + \frac{\partial^2 w}{\partial y^2}\right)$$

The spanwise velocity w doesn't appear in the continuity and x- and y-momentum equations, so they may be solved for in a two-dimensional calculation independently of the z-momentum equation. Since the pressure is a scalar quantity, the pressure coefficient in the 2.5D calculation is related to the pressure coefficient in 3D by renormalizing with respect to the total mach number instead of the LE-normal component:

$$M_n = M_\infty \cos\Lambda_{\mathrm{LE}}$$

$$C_p = \frac{2}{\gamma M_\infty^2}\left(\frac{p}{p_\infty} - 1\right)$$

$$C_{p,2.5\mathrm{D}} = \frac{2}{\gamma M_n^2}\left(\frac{p}{p_\infty} - 1\right)$$

$$\implies C_p = C_{p,2.5\mathrm{D}}\cos\Lambda_{\mathrm{LE}}^2$$

The coordinate system for 2.5D calculations is shown in figure III.4. The local coordinates for the
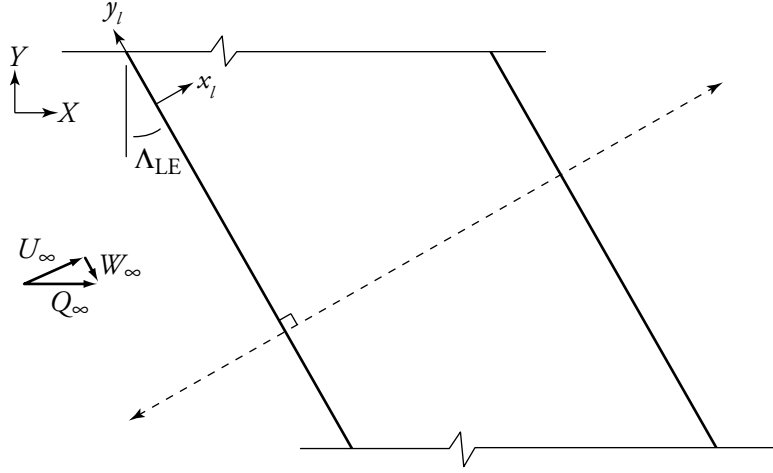
FIGURE III.4. Coordinate system for infinite swept wing calculations. $Z = z_l$ is out of the page for a right-handed coordinate system. Dashed line indicates 2D computational domain.

computation (x_l, y_l, z_l) are related to the global coordinate system (X, Y, Z) by the following relations:

$$x_l = X\cos\Lambda_{\mathrm{LE}} - Y\sin\Lambda_{\mathrm{LE}}$$
$$y_l = X\sin\Lambda_{\mathrm{LE}} + Y\cos\Lambda_{\mathrm{LE}}$$
$$z_l = Z$$

For a given freestream AoA_{aircraft}, the local flow components (u_l, v_l, w_l) for the computational domain (shown by the dashed line in figure III.4) are as follows:

$$u_l = Q_\infty \cos\Lambda_{\mathrm{LE}} \cos AoA_{\mathrm{aircraft}}$$
$$v_l = Q_\infty \sin\Lambda_{\mathrm{LE}} \cos AoA_{\mathrm{aircraft}}$$
$$w_l = Q_\infty \sin AoA_{\mathrm{aircraft}}$$

AoA_{2D} is defined around an axis parallel to the wing leading edge.

As a simple check, figure III.5 show a simple comparison of a 2D, inviscid calculation where the 2D C_p is renormalized to 3D with a 3D periodic calculation. No significant difference is observed in either the C_p or associated LST stability.

This work uses four tools for infinite swept-wing calculations:

1. XFOIL (Drela 1989), an airfoil design code that uses a linear-vorticity panel method with a coupled integral boundary-layer method from ISES Drela & Giles (1987*a*,*b*) and compressibility through the Kármán-Tsien correction (von Kármán 1941; Tsien 1939);

2. TRANAIR (referenced in following section), a nonlinear full potential code coupled with the
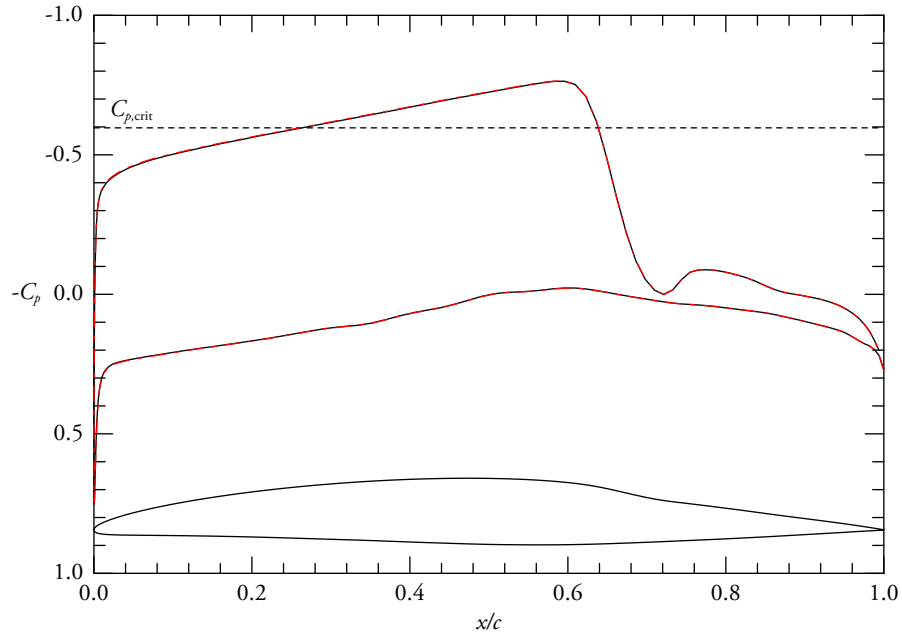
FIGURE III.5. Comparison between inviscid 2.5D and 3D computations at BL234 of TAMU-05-04 at primary design point. Solid line shows FLUENT 3D computation with periodic BCs; red, dashed-dot line shows 2.5D calculation. Dashed line shows critical C_p for $M = 0.75$.

ISES boundary layer model that features automated, adaptive gridding;

3. FLUENT (ANSYS 2010), a 2D or 3D flow modeling suite that includes fully-unstructured methods ranging from inviscid Euler solutions to Navier–Stokes solutions with a range of turbulence models and discretizations;

4. FUN3D (NASA 2013), a 3D fully-unstructured Navier–Stokes code.

3D CALCULATIONS. Full-configuration, 3D computations in this work use the TRANAIR code, a nonlinear full potential code originally developed in collaboration between NASA and Boeing (Samant, Bussoletti, Johnson, Burkhart, Everson, Melvin, Young, Erickson, Madson & Woo 1987). Viscous effects are incorporated by coupling the integral boundary layer model from ISES (Boeing 2007; Drela & Giles 1987a,b). Young, Huffman, Melvin, Hilmes & Johnson (2003) describe the nonlinear elimination method for aerodynamic design optimization, which uses the NPSOL sequential nonlinear programming algorithm (Gill, Murray, Saunders & Wright 1998). Automated, adaptive Cartesian gridding with embedded boundaries simplifies case configuration significantly, which makes TRANAIR suitable for use in design iteration.

The TRANAIR code solves the full, nonlinear potential equation,

$$\nabla \cdot \rho \nabla \Phi = 0,$$

58

which can be derived from the Navier–Stokes equations (§I.1) by defining the potential quantity Φ such that $\mathbf{Q} = \nabla\Phi$. Pressure and density are given by the appropriate isentropic formulas,

$$\rho = \rho_\infty \left[1 + \frac{\gamma - 1}{2} M_\infty^2 \left(1 - \frac{Q^2}{Q_\infty^2} \right) \right]^{1/(\gamma-1)}$$

$$p = p_\infty \left[1 + \frac{\gamma - 1}{2} M_\infty^2 \left(1 - \frac{Q^2}{Q_\infty^2} \right) \right]^{\gamma/(\gamma-1)}$$

The boundary conditions include a far field condition that the perturbation potential tends to zero far from the configuration boundary. The integral boundary layer model is "closely coupled" in the sense that the inviscid potential equations and the viscous equations are combined and solved together. Methods are included to predict transition; in this work, the parameters are configured liberally so that transition is assumed to typically occur only at an adverse pressure gradient.

III.2.2. *Boundary-layer meanflow*

One approach to simplifying the equations is the nested approach, consisting of an outer solution in the freestream and an inner solution in the boundary layer. In the freestream flow as described in the previous section, boundary layer effects are neglected completely (as in invsicid flow in XFOIL or FLUENT), approximated using an integral method (XFOIL or TRANAIR with the coupled ISES integral boundary layer model), or calculated using a grid resolution with insufficient resolution in the boundary layer to extract boundary-layer profiles for stability computations (viscous FLUENT and FUN3D). The expectation in each of these approaches was that the boundary-layer meanflow for stability computations would be calculated separately, using the surface geometry and pressure distribution as boundary conditions for a DBL solver.

This work uses WINGBL2 (Pruett 1994), a spectrally accurate code that solves the boundary layer equations on an infinite swept wing. WINGBL2 includes the effects of streamwise curvature and streamwise pressure gradient in the governing equations and boundary conditions. The boundary-layer equations are formulated for both the attachment-line flow and for the boundary layer, where the latter is solved by marching in the direction perpendicular to the leading edge.

There are a few limitations in this approach when compared to viscous profiles as in Roberts (2012) or Liao *et al.* (2012). First of all, for 3D computations, the DBL method only provides a reasonable approximation to the actual boundary layer if the pressure isobars approximate an infinite swept wing. Second, the boundary-layer effects on the pressure gradient on the outer solution are not directly coupled. Third, the boundary-layer solver is not valid in an adverse pressure gradient. Finally, transition is not computed directly, and thus some iteration between the outer solution, the inner solution, and the stability computation is necessary to obtain a "conclusive" answer about the location of transition for the DBL method.

The python script X2W in §C.1 converts the C_p slices from the outer solution (XFOIL, FLUENT,

FUN3D, or TRANAIR) to input files for WINGBL2.

III.2.3. *Boundary-layer stability*

The bulk of this work uses the LST outlined in §I.1 as implemented in the LASTRAC code, (Chang 2004). LASTRAC is a general purpose, physics-based transition analysis code. LST calculations in LASTRAC use the boundary solution from WINGBL2, which is converted to a LASTRAC meanflow file by W2L (§C.2). The range of unstable frequencies and wavelengths calculated is typically $1 \text{ kHz} \leq f \leq 10 \text{ kHz}$ for a TS wave normal to the leading edge (i.e., zero spanwise wavenumber) and $1 \text{ mm} \leq \lambda \leq 40 \text{ mm}$ for stationary crossflow ($f = 0$). Typical input files are included as a part of X2W in appendix C, §C.1.

III.3. 2.5D airfoil design

As a precursor to 3D design, 2.5D airfoil design provides first-order effects and information about sensitivity to geometry perturbations, as well as buttline cuts for the lofted the wing glove. An overview of the process is given in figure III.6, which was used to develop the airfoils sequenced using the schemata in figure III.7. These airfoils formed the basis for initial feasibility studies as well as configurations up through SARGE TAMU-05-04 configuration, which was used as the input for the optimization process to develop TAMU-06-05.
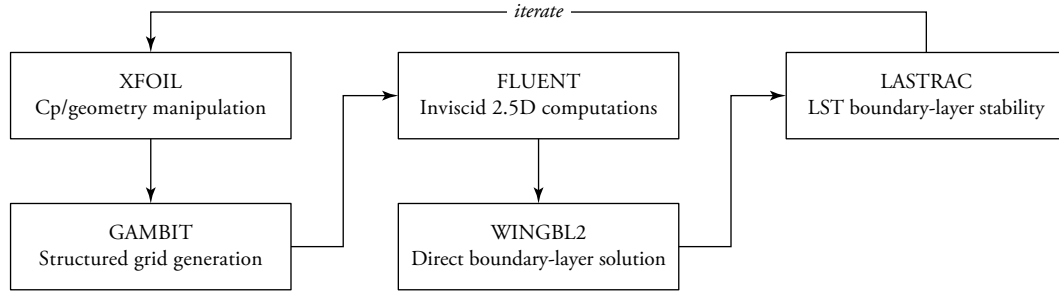
FIGURE III.6. 2.5D airfoil design process flowchart used through TAMU2D-04 airfoil series.

III.3.1. *Geometry manipulation*

Rapid iteration is of prime importance at this preliminary stage in the design. There are two basic approaches to airfoil design: direct geometry manipulation and inverse methods. In the direct geometry method, the geometry is perturbed and followed by a flow solution to determine a pressure distribution.

(*a*) <u>TAMU</u>-<u>000A</u>-<u>00</u>
 1   2 3 4

  1. TAMU · Texas A&M University airfoil section
  2. 000 · Airfoil sequence number
  3. A · Airfoil type
    T = "Traditional"
    P = "Pfenninger"
  4. 00 · Mach number × 10^{-2}

(*b*) <u>TAMU2D</u>-<u>00</u>-<u>BL000</u>-<u>DI</u>-<u>UN</u>
 1   2 3 4 5

  1. TAMU2D · Texas A&M University SARGE 2D airfoil section
  2. 00 · Airfoil sequence number (consecutive from series 1 airfoils)
  3. BL000 · Buttock line for airfoil section, in inches
  4. DI · Section orientation
    SW = streamwise
    NL = normal to glove LE (transformed from SW)
  5. UN · Units
    ND = non-dimensional *x/c* and *y/c*
    IN = inches
    MO = inches (input coordinates for model construction only)

FIGURE III.7. Airfoil naming for TAMU SARGE airfoil BL sections: (*a*) series 1 and (*b*) series 2.

The direct approach is computationally efficient, but since pressure gradient effects are of higher-order importance in laminar flow design when compared to geometry effects, inverse methods are logical. In 2D, invsicid inverse design is straightforward and computationally efficient. The full-inverse method in XFOIL is similar to that of Eppler & Somers (1980), using the physical surface arc-length rather than the non-physical circle plane coordinate system common to mapping methods (Drela 1989).

For the purposes of laminar flow design at high-Re_c and transonic Mach numbers, XFOIL does not generally generate realistic LST growth. Figure III.8 shows an example *AoA* sweep calculation on TAMU-003T-75.

When comparing the C_p at $AoA = 0°$ (figure III.9), the pressure sides are qualitatively similar, while majority of the higher-order effects are observed on the suction side. This is typical that the suction side is more problematic than the pressure side owing to the greater flow acceleration that leads to significant nonlinear effects. This is the reason why Ryle (1970), for example, describes a design methodology that focuses entirely on the suction side distribution, essentially letting the pressure side be designed as an afterthought. For the purposes of this work, since simultaneous demonstration of laminar flow on the suction and pressure sides is a design requirement, it was not possible to ignore the pressure side in this
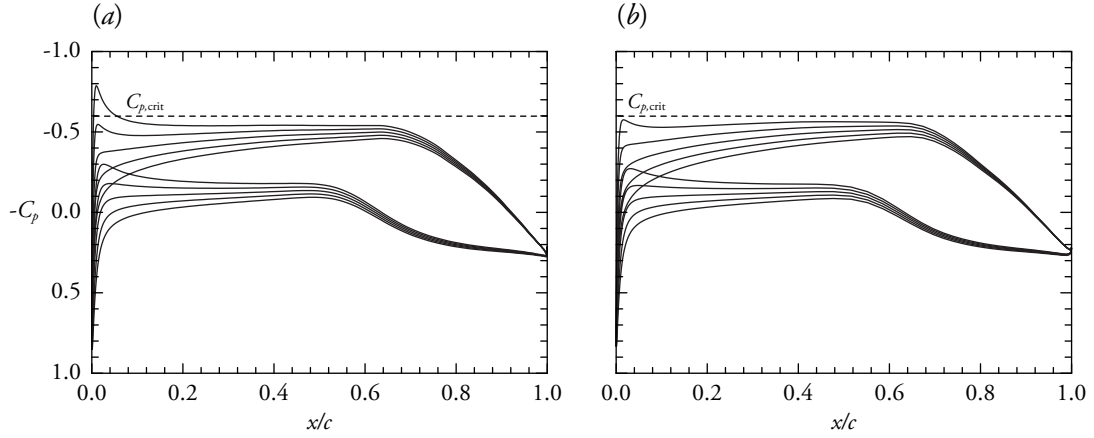
FIGURE III.8. Inviscid C_p results for TAMU-003T-75 for $AoA = [-1°, 1°]$ computed in (*a*) XFOIL and (*b*) FLUENT at $M = 0.75$. Dashed line shows critical $C_{p,\text{crit}} = -0.59$ at $M = 0.75$.
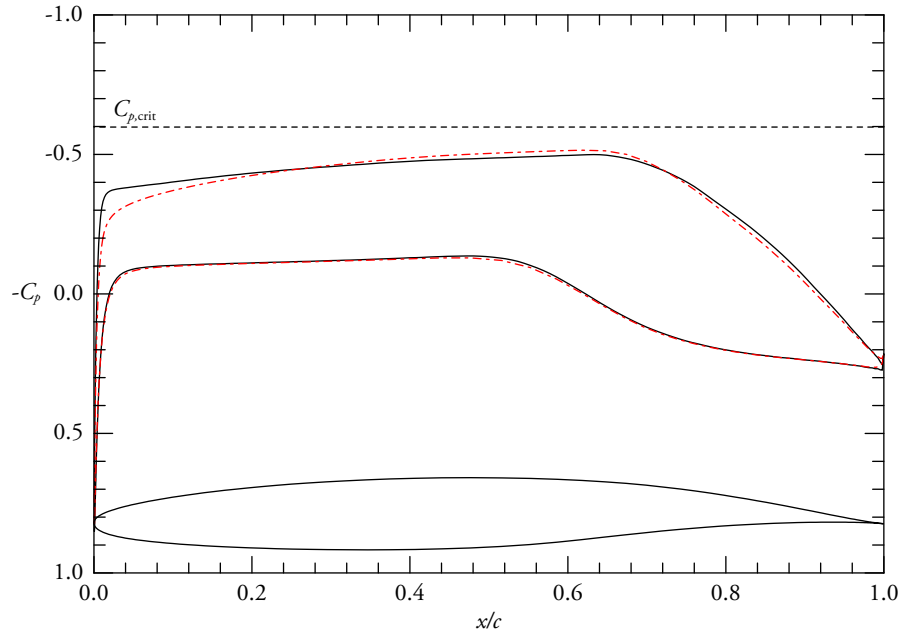
FIGURE III.9. Inviscid C_p results for TAMU-003T-75 for $AoA = 0°$ computed in XFOIL (solid line) and FLUENT (red dashed-dot line) at $M = 0.75$. Dashed line shows critical $C_{p,\text{crit}} = -0.59$ at $M = 0.75$.

manner, nor is there any reasonable reason to do so using current computational methods.

As mentioned previously, XFOIL is a linear-vorticity panel code with compressibility incorporated through the Kármán-Tsien correction, given in the following form by Anderson (2003), where C_{p_0} is

the incompressible C_p:

$$C_p = \frac{C_{p_0}}{\sqrt{1 - M_\infty^2} + [M_\infty^2/(1 + \sqrt{1 - M_\infty^2})](C_{p_0}/2)}$$

Like other compressibility corrections such as the Prandtl-Glauert and Laintone (1951) transformations, this transformation is strictly valid only for small perturbations around $C_p = 0$ and the accuracy is reduced as $M_\infty \to 1$. Since this design is near-sonic or transonic at all stages of development, this correction is an imperfect approximation, as substantiated in appendix B.

LST N-factors for stationary crossflow are shown in figure III.10. As expected from inspection of the C_p in figure III.9, the stability differences on the pressure side are negligible, while the differences on the suction side are significant.

Despite these issues, XFOIL is a usable tool for airfoil manipulation and the zero-order pressure effects are useful to get a sense of qualitative sensitivity for a given geometry change. Within the narrow range of designs considered, after some practice it is possible to sketch a C_p in XFOIL that will give the desired profile when that geometry is solved in an inviscid Euler computation.

In the wing glove design, the unchangeable host wing geometry needs to be considered and held fixed. Figure III.11 shows the development of TAMU2D-04-BL198. The geometry is fixed for approximately $x/c > 0.75$ on the suction side of the wing and $x/c > 0.38$ on the pressure side for this airfoil; the region of the glove that may be varied is delimited by square brackets in the figure. The actual value is fixed to the host wing wing: the location of the aft spar on the upper surface and selection of ideal point for smooth blending on the lower surface. On the upper surface, an ERA requirement requires that the of outer mold line (OML) glove test section be offset from the G-III OML by 50.8 mm (2.0 inches) to $x/c = 0.6$ on the suction side in order to allow for subsurface instrumentation and the floating glove structure below.

There are two ways that the glove geometry is varied without affecting the fixed regions. One is to use the mixed-inverse routine in XFOIL, which allows a section of the wing to be marked off to limit the extent of geometry manipulation. The mixed-inverse is an iterative method, unlike the full-inverse method previously described, and hence it is not assured that the range of permitted geometry modifications are physically able to produce every conceivable pressure distribution when considering the parts left unchanged.

The second method, which can be used in conjunction with the full-inverse routine in XFOIL, is to modify the glove without any geometry constraints and then use a Mathematica routine to smoothing blend the airfoils in a manner that maintains curvature continuity at the glove and wing OML junctions. This method leads to an iterative process to develop a smooth transition.
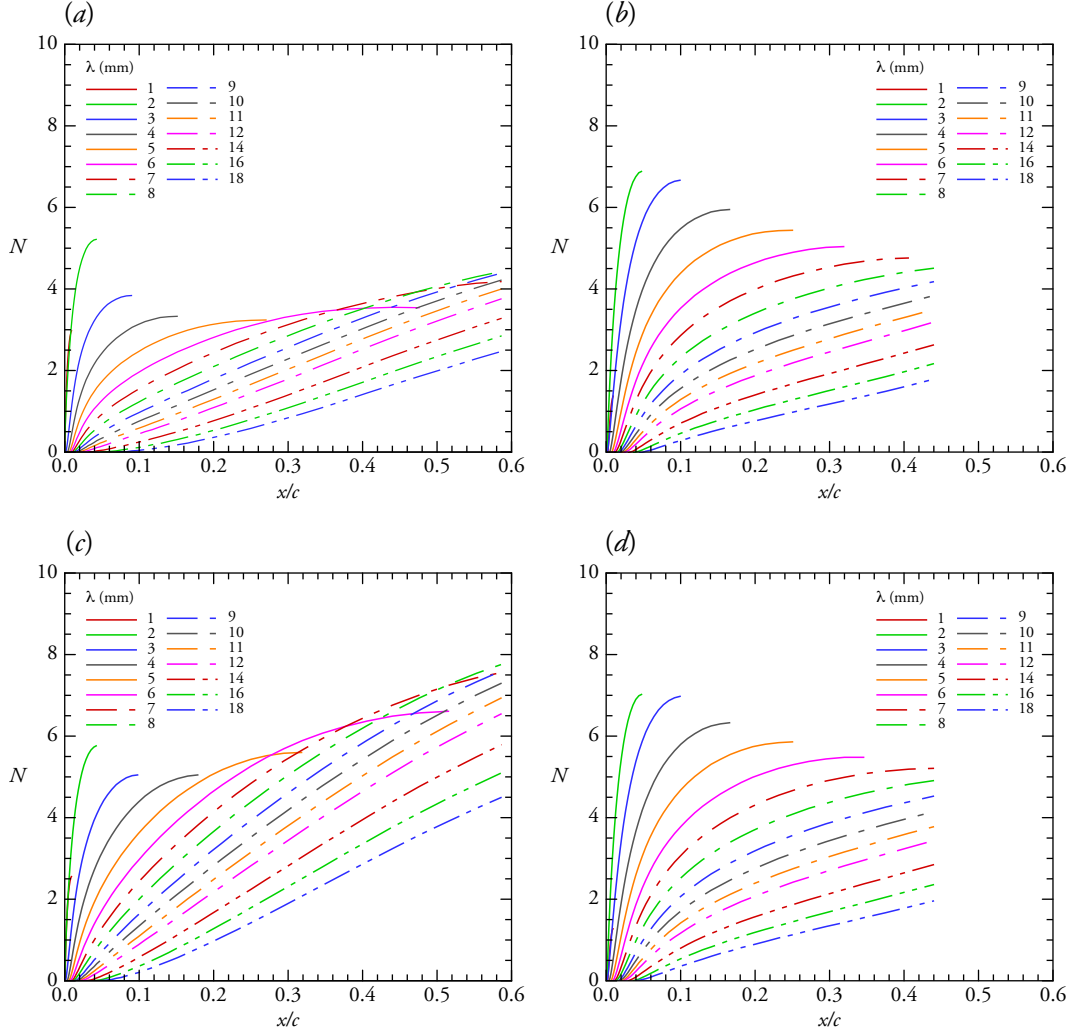
FIGURE III.10. Comparison of 2.5D LST stationary crossflow N-factors on TAMU-003T-75 at $M = 0.75$, $Re_c = 17.3 \times 10^6$. (*a*) XFOIL, suction-side; (*b*) XFOIL, pressure side; (*c*) FLUENT, suction side; (*b*) FLUENT, pressure side.
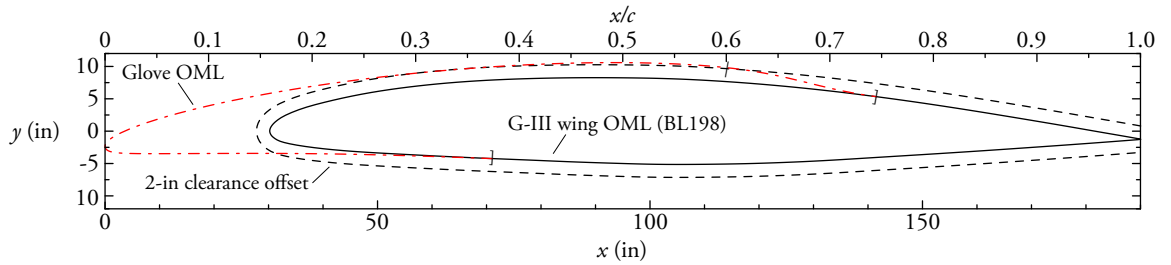
FIGURE III.11. TAMU2D-04-BL198 glove OML. Brackets show limit of glove OML to be designed. Single line at $x/c = 0.6$ shows aft requirement for 2-inch clearance on suction side.

III.3.2. *Euler and Navier-Stokes calculations*

For higher-fidelity computations of the airfoil pressure distribution, the choices available in the work are full nonlinear potential with coupled viscous effects in TRANAIR and invsicid Euler or viscous Navier–Stokes in FLUENT or FUN3D. TRANAIR was licensed at TAMU close to the release of the TAMU-06-05 design, and hence was not available for much of this work.

When choosing between inviscid computations and viscous computations for design, the driving concern is a tradeoff between time and accuracy, both that spent in grid generation and solution. The bulk of the surface pressure distribution is established by inviscid effects. A viscous computation will capture effects such as accurate behavior around the trailing edge, which can have significant effect on the circulation and hence the overall circulation, and effects of geometrical imperfections on the boundary layer. A viscous solution will also capture the influence of shocks more realistically. However, a viscous solution requires a more refined grid for an accurate solution, especially localized in areas such as the aforementioned trailing edge and imperfections.

For initial analysis purposes, the problem is simplified by inviscid analysis in FLUENT or FUN3D or first-order inclusion of viscous effects through coupling of an integral boundary layer model in TRANAIR. The TAMU and TAMU2D were design with sharp trailing edges (rather than a physical, finite radius), which can be expected to minimize discrepancy between the circulation in a viscous and inviscid solution. However, the physical geometry has a trailing edge with finite radius. In a viscous computation, there's no significant advantage gained by simplifying the trailing edge.

Figure III.12 shows the 2D invsicid mesh typically used in this work, as applied to TAMU2D-003T-75. This mesh is generated using GAMBIT for use in FLUENT or FUN3D. The structured C-mesh has a conic farfield and is nondimensionalized by the airfoil chord. The grid extends 40 chord lengths aft of the airfoil leading edge, 25 chords forward, and 40 chord lengths in above and below. There are 125 points on each of the upper and lower airfoil surfaces with an initial off-body length of $\Delta y_0 = 0.0001$. The grid contains in total 49 470 points and 49 000 cells. FLUENT is a dimensional code, so this nondimensionalization is only valid in an inviscid computation where terms that depend on Re are neglected; in a viscous computation, the boundary layer effect would be improperly scaled. The results of a grid independence study on this mesh are included in appendix B.

Figure III.13 shows an unstructured O-mesh on the same airfoil as constructed using Pointwise (Pointwise 2013). This grid is refined for viscous computations in FUN3D. The farfield is a circle of radius $60c$ comprising 49 nodes and centered on the airfoil leading edge. There are 401 points on the upper surface of the airfoil and 301 points on the lower surface, locally clustered around the leading edge, trailing edge, and upper-surface blending. Anisotropic cells with an initial off-body spacing of $\Delta y_0 = 1 \times 10^{-5}$ and growth rate 1.06 form the boundary layer mesh, which merge smoothly with the freestream mesh. The grid has 59 358 nodes and 117 967 cells.

The significance of viscous effects on boundary layer stability is established by comparing the pressure distributions and boundary-layer stability on four cases. Three cases are computed in FUN3D: 2.5D
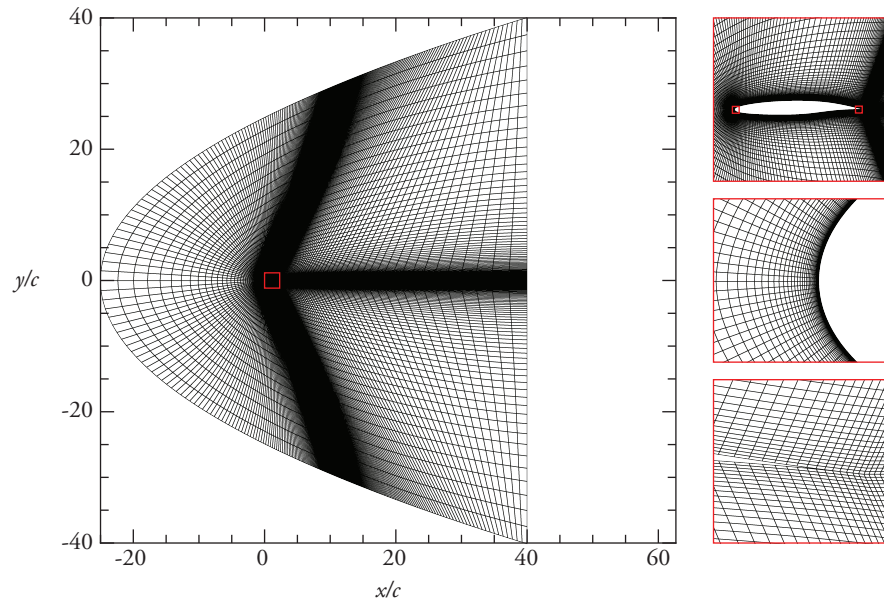
FIGURE III.12. Structured C-mesh used in invsicid FLUENT and FUN3D computations, shown applied to TAMU-003T-75.
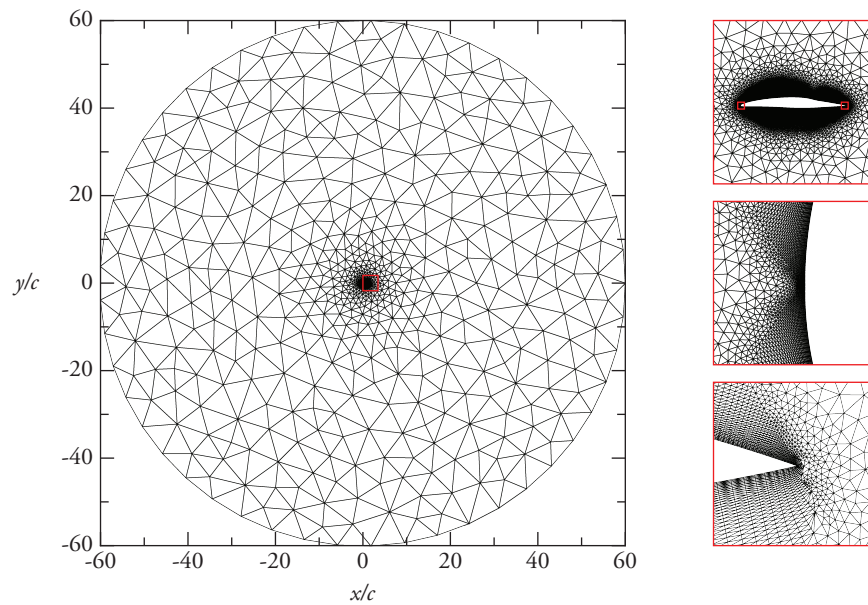
FIGURE III.13. Unstructured O-mesh used in viscous FUN3D computations, shown applied to TAMU2D-04-BL198.

inviscid computation on the grid in figure III.12, 2.5D and 3D (periodic) viscous computations on the mesh in figure III.13. A fourth case is computed in 2D TRANAIR with boundary-layer coupling.

In the viscous FUN3D and TRANAIR cases, transition is set at $x/c = 0.62$. In FUN3D, this is accomplished by solving the full Navier-Stokes equations upstream of a specified transition location on the airfoil upper and lower surfaces and the incorporating the k–ω SST turbulence model downstream. FUN3D calculates the distance for each node from the upper and lower surfaces and determines the appropriate model to use for a particular node using a surface distance calculation and choses the appropriate model based on the closest surface. The resulting computational regions are shown in figure III.14.
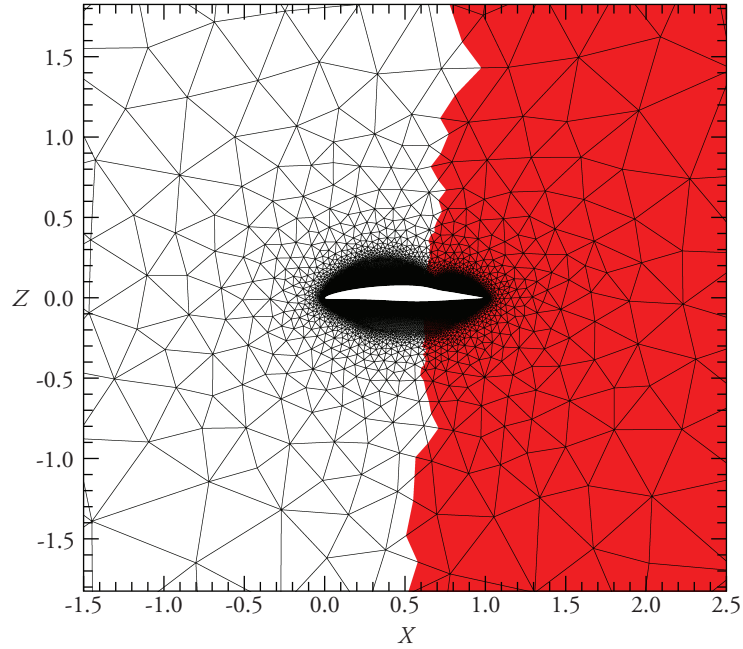
FIGURE III.14. Laminar-turbulent transition imposed in FUN3D. White region shows nodes where full Navier-Stokes equations are solved, while red region shows nodes where k–ω SST turbulent model is incorporated.

Figure III.15 shows the pressure distributions calculated for the four cases. Qualitatively, the pressures are similar. In all cases, the lower surface shows only slight discrepancies between the calculations. This is as expected from the fact that nonlinear effects are typically more pronounced on the suction side for a cambered wing.

On the suction side, the viscous computations each produce a suction peak slightly aft of the inviscid location. The location is within approximately one node of the invsicid computation, so this may be due

to grid refinement and not a significant viscous effect. The viscous effects increase the overall pressure slightly, but the gradient is approximately constant. Interestingly, the TRANAIR curve follows the inviscid FUN3D solution until $x/c \approx 0.2$, where it becomes slightly more favorable and switches to follow the FUN3D viscous curves. Slight differences are also observed between the 2.5D and 3D viscous FUN3D curves, principally near the leading edge. The solution is iteration converged, so this may suggest that additional grid convergence is necessary, especially near the leading edge. It is possible the discrepancy is due to coupling of the w component through viscous dissipation in energy equation, which is not accounted for in the justification for a 2D calculation as previously described.
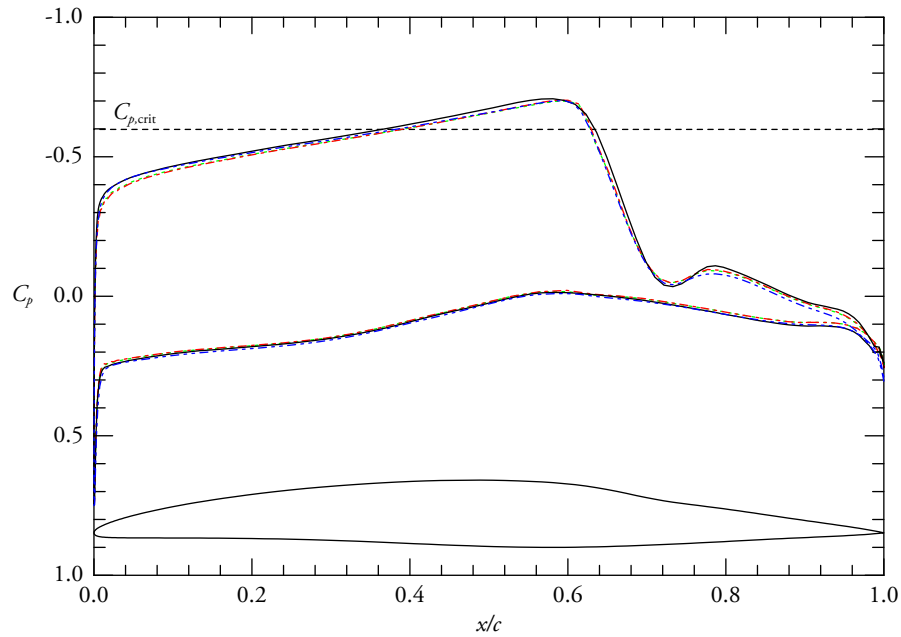
FIGURE III.15. TAMU2D-04-BL198 C_p comparison of inviscid (solid line), 2D (corrected) viscous (red dash-dot line), 3D viscous (green dotted line) C_p using FUN3D and boundary-layer coupled 2D (corrected) TRANAIR (blue dash-dot-dot line).

LST stability behavior (figure III.16) shows greater differences than is visible inspection of C_p, which reiterates the sensitivity of laminar flow design to "small" changes in C_p near the leading edge. On the suction side, The expected transition location for $N = 9$ moves forward by 0.02 from invsicid 2.5D FUN3D (a) to viscous 2.5D FUN3D (c), and then even more slightly forward for 2.5D to 3D viscous FUN3D (e). The growth of small wavelengths is similar for cases except viscous 3D FUN3D, which shows growth larger by about $\varDelta N = 1$ for $\lambda < 4$ mm. The pressure side exhibits no significant differences in transition location, although there are again some small differences up to $\varDelta N = 1$ in the maximum N-factor for small wavelengths.
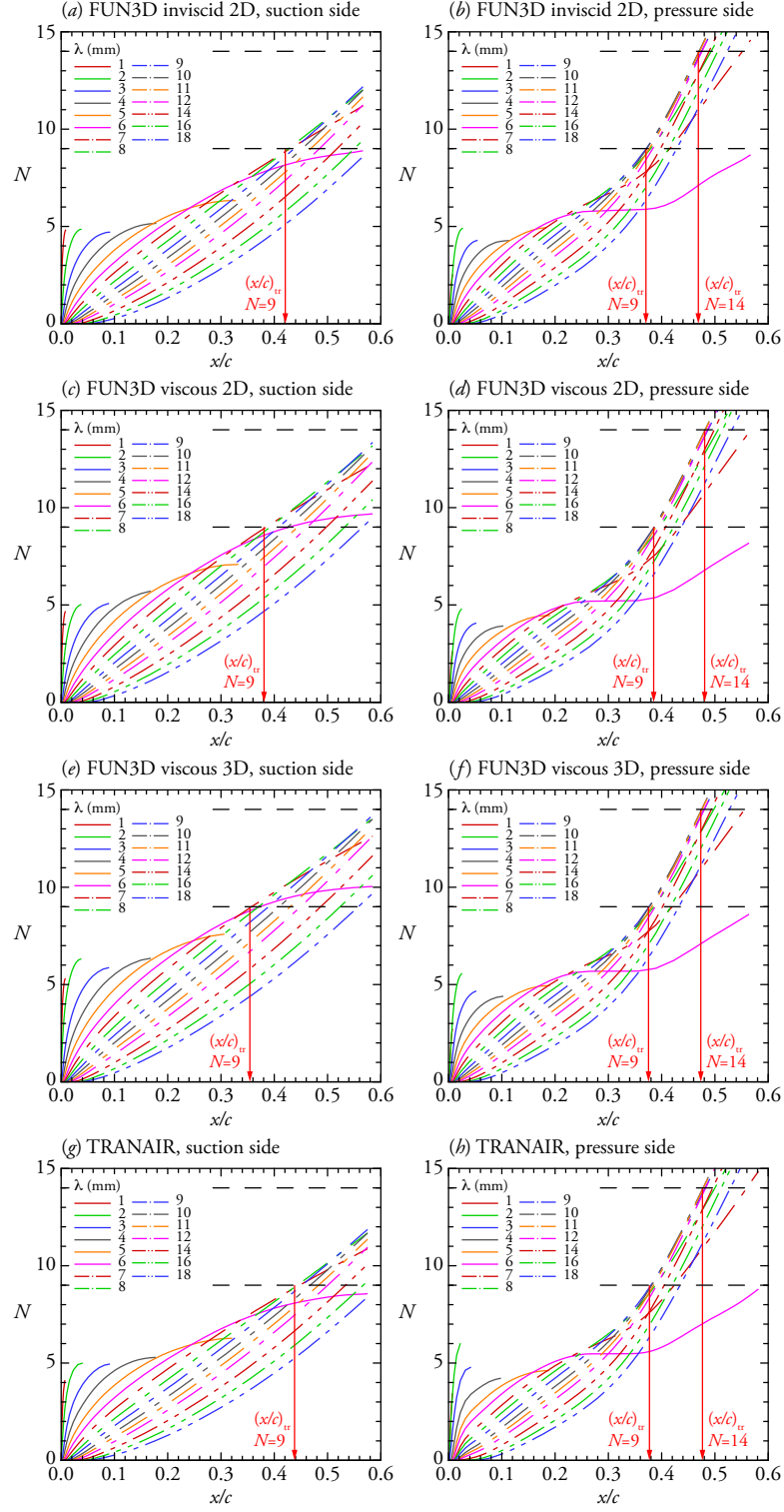
FIGURE III.16. Stationary crossflow LST *N*-factors corresponding to the pressure distributions calculated in figure III.15.

For this case, the TRANAIR coupled boundary layer model appears to bring the stability behavior closer to inviscid Euler, rather than to viscous Navier–Stokes. Although not shown, inviscid TRANAIR exhibits a significant deviation from inviscid Euler, showing a much greater flow acceleration on the suction side and a correspondingly lower C_p.

One issue contributing to the discrepancy follows from the aforementioned viscous effects near the trailing edge. In this case, the viscous location of the stagnation point on the trailing edge results in circulation that is slightly decreased in the viscous solution, effectively implying a slightly lower C_l at the same *AoA* for viscous flow when compared to inviscid: $C_l = 0.50$ for inviscid FUN3D, but $C_l = 0.48$ for both viscous FUN3D cases and TRANAIR.

Regardless, when compared to the comparison between XFOIL and inviscid FLUENT in the previous section, these differences are relatively minor and expected to be insignificant in comparison to 3D effects when the sections are lofted into a wing glove as in the following section. For this stage of design, which is essentially a "throwaway" analysis once 3D results are computed, any of the methods is considered suitable. As stated at the outset, the driving consideration is likely the required time per iteration. In this case, 2D TRANAIR is the most efficient by a few orders of magnitude. If the case is already configured, TRANAIR takes airfoil coordinates directly as input and generates the grid automatically, which implies negligible case configuration time. An entire flow solution is computed in seconds on a desktop workstation.

The Euler and Navier-Stokes methods in FLUENT or FUN3D, which require user-generated off-body gridding, consume significantly more computational time for a solution. Assuming the grid parameters are already determined (or automated) and the solution is run in parallel using 4 cores on the same workstation, the total time for a iteration-converged solution is 30-60 minutes. For a few percent in $(x/c)_{tr}$, this additional time is likely not worthwhile except as an occasional check.

III.4. 3D glove design: optimization

The extension of the 2.5D airfoil design process to 3D is straightforward. An overview of the optimization process is described in §§II.2.5,III.2. This section focuses on development of the target C_p to drive the objective function for C_p matching followed by an assessment of the efficiency of the optimization process as executed.

In the previous section, a target C_p was developed principally using XFOIL to establish sensitivity of the design to geometrical changes, followed by a detailed compressible Euler computation to determine a relatively more accurate C_p and associated LST stability behavior. By contrast, since the goal in optimization is to provide a C_p, alone, to be matched across the glove span, there is no requirement to determine the physical geometry. The starting point for the optimization routine is the TAMU-06-05 glove design, and the optimizer perturbs the geometry in a 3D TRANAIR solution to match the target C_p.

The problem here, therefore, is how to most effectively determine the target pressure distribution. Again, XFOIL could be used since it has an efficient interface for sketching pressure distributions. However, in certain situations—especially near the leading edge wither the pressure gradient is relatively large—XFOIL may exhibit significant Runge phenomena when fitting a spline through the specified C_p points.

Another option is to optimize the laminar flow stability directly without manually perturbing the C_p, following a method similar to that of Amoignon *et al.* (2006). However, when only an handful of target pressure distributions are likely to be to be developed in this design, it may not be practical to develop an optimization routine. Therefore, a method is developed using Mathematica (Wolfram Research 2013) to rapidly sketch a pressure distribution and analyze the LST stability.

An input C_p is parameterized using a least-squares fit to determine the control points of a B-spline curve with cubic basis as shown figure III.17. The Manipulate function in Mathematica allows the control points to be graphically adjusted; the x/c-location of the points is held fixed while the C_p value is varied within a suitable range. The end points of the adjustment region are held fixed, allowing the adjusted C_p to be trivially combined with unchanged portions of the C_p and written to a file. The resulting C_p is then analyzed using X2W, WINGBL2 and LASTRAC to estimate the laminar stability characteristics.
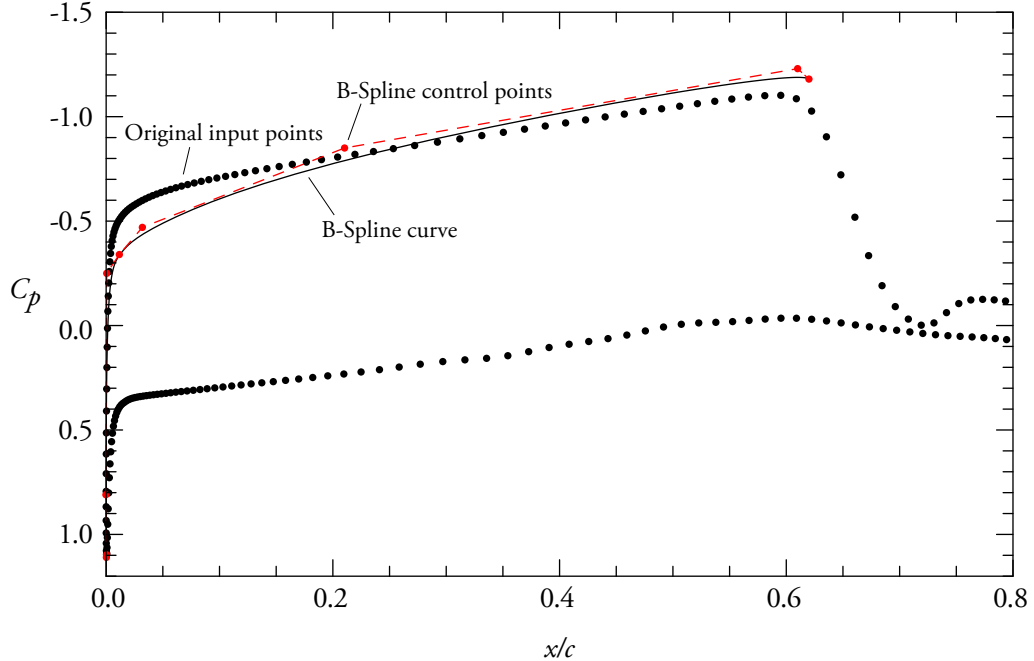
FIGURE III.17. B-spline control points used for C_p optimization target.

This direct C_p approach holds the physical geometry constant by assuming that the geometry changes are "small" such that they will not significantly affect an LST computations. LST neglects the effects of curvature and assumes a locally parallel flow, so this should not be an issue. As already mentioned, the physical 2.5D airfoil geometry is not needed in optimization process and hence there is no reason to compute it.

As a reassuring check, LST stability computations on four cases provide a quantitive evaluation of the validity of neglecting geometrical changes. The cases are constructed permuting the airfoil coordinates and C_p distributions of TAMU2D-03A-BL198 and TAMU2D-04-BL270:

- 00. TAMU2D-03A-BL198 geometry and C_p, figures III.18(*a*) and III.18(*b*)
- 10. TAMU2D-04-BL198 geometry and TAMU2D-03A-BL198 C_p, figures III.18(*c*) and III.18(*d*)
- 01. TAMU2D-03A-BL198 geometry and TAMU2D-04-BL198 C_p, figures III.18(*e*) and III.18(*f*)
- 11. TAMU2D-04-BL198 geometry and C_p, figures III.18(*g*) and III.18(*h*)

Table III.4 summarizes the basic parameters of the two airfoils.
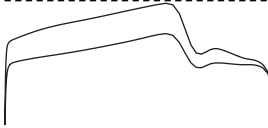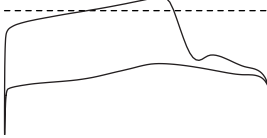
	TAMU2D-03A-BL198	TAMU2D-04-BL198
$-C_p$		
Airfoil		
M	0.75	0.75
AoA_{2D}	0.8°	2.2°
Re_c	22 million	22 million
Λ_{LE}	34.8°	34.6°
c (streamwise)	4.8 m (16 ft)	4.8 m (16 ft)
H (ft)	40 700	40 700
t/c (streamwise)	9.6%	8.2%
r_{LE}	19 mm (0.75 in)	18 mm (0.69 in)
Re_θ	73	70
C_ℓ	0.25	0.50

TABLE III.4. Specifications for airfoil geometry/C_p sensitivity interchange.

The crossflow LST N-factors for the four cases in figure III.18 show no significant influence of the physical geometry on either the suction or pressure side of the airfoils. One would expect that cases 00 and 10 would be similar and likewise for cases 01 and 11. This appears to be the case.

Furthermore, the difference in pressure distributions between these two cases is significantly larger than between the starting pressure distribution and final target pressure distribution in the actual TAMU-06-05 optimization. These pressure distributions have different C_l; the optimization uses $C_\ell = 0.5$ throughout.

The linear PSE Herbert (1997), however, includes the stabilizing effect of body curvature in the stability computation and nonparallel effects. A PSE analysis would be expected to reflect a difference between the two geometries if the curvature difference is significant. In this case, TAMU2D-03A-BL198 is a full glove with 2-inch clearance to $x/c \approx 0.60$ while TAMU2D-04-BL198 truncates much earlier at $x/c = 0.37$, which leads to a significant difference in curvature. Indeed, an qualitative LPSE analysis shows that the stabilizing effect of the TAMU2D-03A-BL198 geometry is significant, lowering final N-factors by a few counts when used in a computation.

The TAMU2D-06-05 optimization process took approximately 5 months to complete, from its start in March 2011 to the PDR OML freeze in August 2011. The planform was essentially unchanged. Figure III.19 shows the airfoil differences at BL198, BL234, and BL270. This demonstrates the high sensitivity of the flow to small geometrical changes, but one might wonder if the amount of time it took to set up the optimizer could have been more effectively used by continuing to modify the design "manually" by following a more traditional process along the lines of figure III.3(a).

Note, for example, that not much manual labor was saved by developing target C_p distributions instead of airfoil sections. The amount of labor in a single pressure distribution as implemented in this section is effectively the same as a single airfoil. The optimization process required only one target C_p to be developed, versus at least two airfoil sections to define a straight loft.

A more significant concern is that the aerodynamic optimization process is only optimization in the sense that it strives to meet the objective defined by the user. There is no guarantee that the objective itself is truly optimum in any global sense. The resulting optimum is limited by the design variables and ranges selected by the user, the robustness and specification of the objective function, and the behavior of the optimization algorithm for the given problem.

In aerodynamic optimization, even in a simplified case like this wing glove, there are dozens to hundreds of design variables and the objective function involves the evaluation of hundreds of values summed to a single objective value to be minimized. If the starting point in the design space given to the optimizer is far from the "best" answer, then the resulting design may be artificially limited. Furthermore, there are many considerations in aerodynamic design that cannot be easily represented in a single objective function.

For an elliptical set of PDEs like the Navier-Stokes equations, changes in conditions in one part of the domain can propagate to others: consider for example the effect of deforming a simple flap. Flap deformation produces additional lift by changing the circulation about the wing, as shown in figure III.20 for a notional $\delta_f = +3°$ flap deformation on TAMU2D-04-BL198.

This leads to one possible alternative approach to achieving the required C_ℓ on a wing glove design:
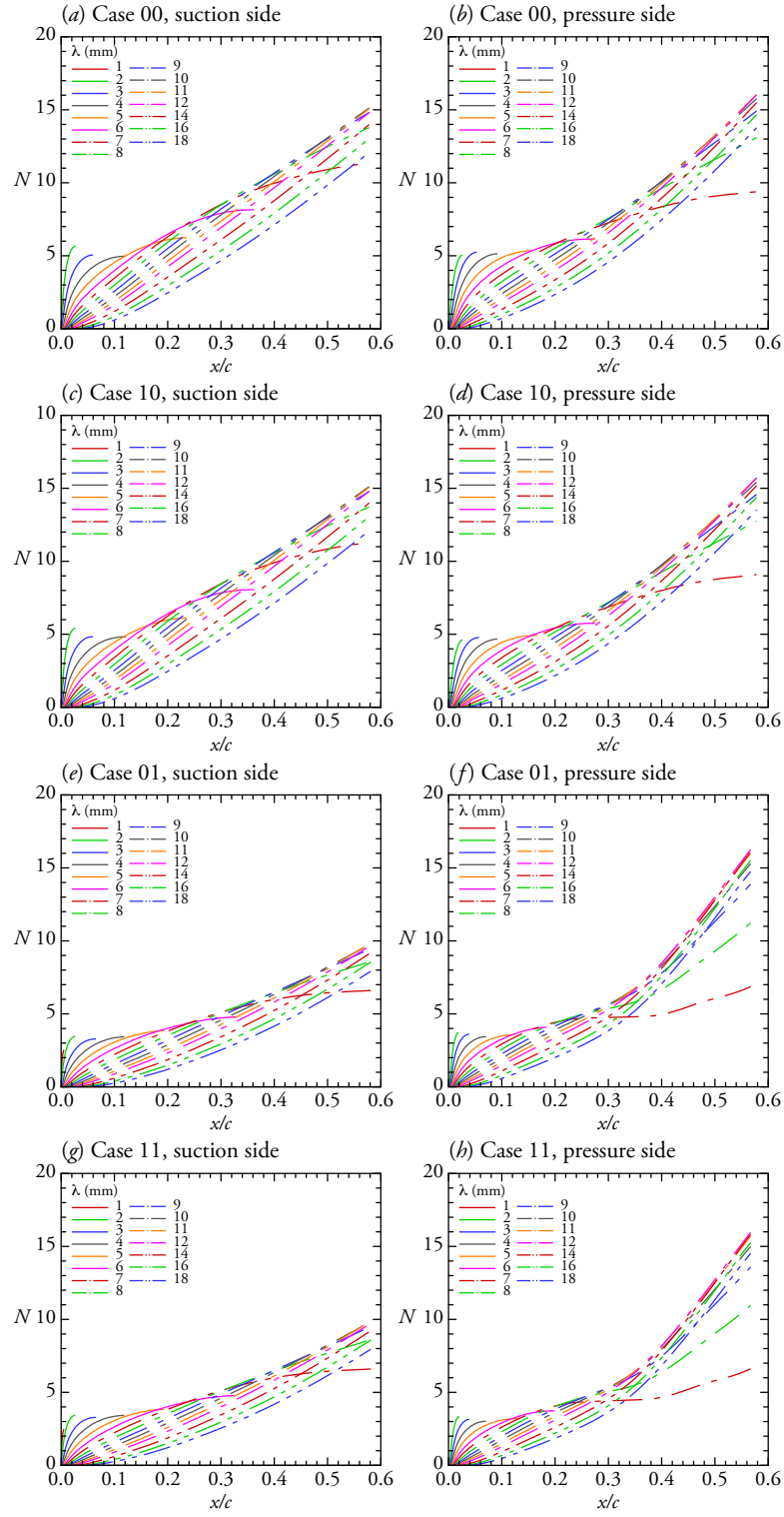
FIGURE III.18. LST *N*-factors for combinations of geometry and C_p from TAMU2D-03A-BL198 and TAMU2D-04-BL198. Refer to §III.4 for descriptions of (*a*)-(*h*).
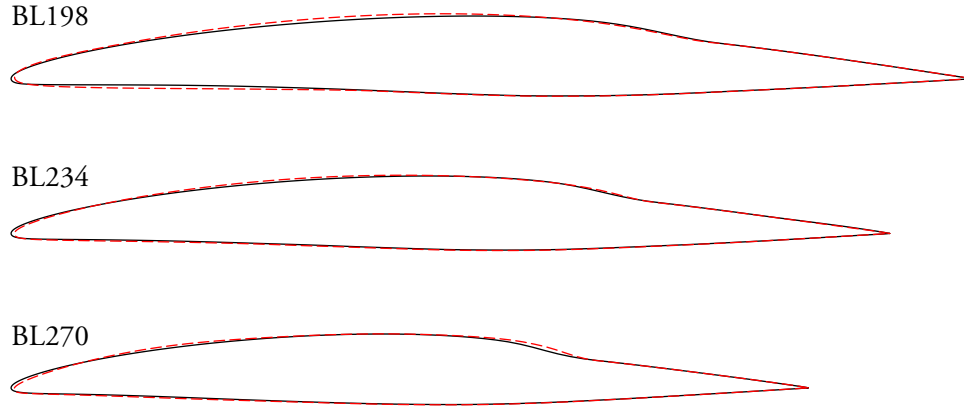
FIGURE III.19. Comparison between TAMU-05-04 (straight loft, solid black line) and TAMU-06-05 (optimized glove, dashed red line) at BL198, BL234, and BL270.
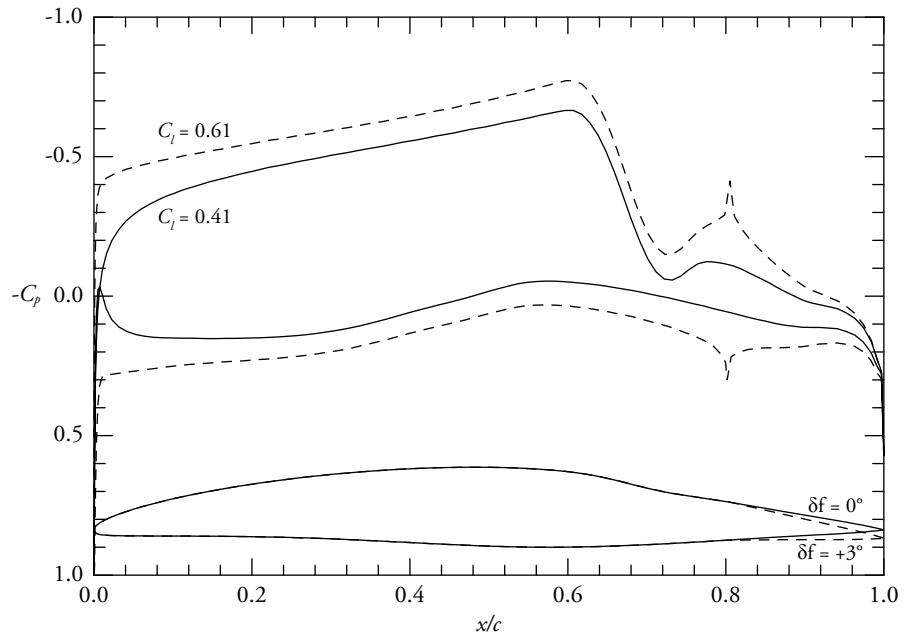
FIGURE III.20. Notional flap deformation on TAMU2D-04-BL198. Flow condition is incompressible 2D, $AoA_{2D} = 1°$. Solid line shows $\delta_f = 0°$, dashed line $\delta_f = +3°$.

impart a small deflection to the flap. For the G-III, $\delta_f = +10°$ is permitted up to $Q_\infty = 250$ KCAS, which allows deflection at the SARGE design point. Such a deflection may be justifiable for a glove design since in a full wing design, camber and geometry would not be constrained in the aft part of the wing as it is for the glove. If the deformed flap condition produces an operationally relevant pressure distribution on the glove surface, then it should be valid option to meet the design objectives.

Cavalierly stated, one principal advantage of using optimization to design a wing is that is that once the process is defined, execution to meet the objective function is effectively a "dumb" process. By defining a 2.5D target distribution and passing it to an optimization routine to achieve that target distribution on the fully 3D wing glove, little physical understanding of 3D, finite wing effects are required to attain that pressure distribution uniformly.

However, such an approach could be deceptive. As mentioned, the optimization only answers the question that the user asks, given the design space that the user defines. Optimization is not a substitute for physical understanding of 3D wing effects. When applied without such understanding, the optimization is likely to achieve a poor design for the simple reason that the user defined at the outset what the resulting design should be. The optimizer simply finds a way to geometry that fulfills the requested objectives.

III.5. 3D glove design: traditional process

An optimization process as described in the last section needs a starting point. It is essentially infeasible using current technology to automatically optimize a full, 3D wing design from scratch. This is the conundrum posed by Küchemann (1978), who notes that optimization "can only be done in a meaningful and realistic manner if a conceptual framework for the type of aircraft to be examined already exists."

The achievement of the optimizer is then most effectively the automation of some of the late stages of design refinement, most useful in localized situations: TAMU-05-04 marginally met the design requirements, so the optimizer improved the design by iterating the geometry by rote. Developing TAMU-05-04 required five months of design and analysis, which followed on a year of preliminary studies.

Clearly, the development of TAMU-05-04 was not the critical path had clear design requirements been defined at the outset and adhered to. This section describes the critical path that could have been taken from point the design requirements are defined to obtain an initial geometry for further refinement (by continuing through multiple iterations of this process) or for use as the starting geometry for an optimizer.

III.5.1. *Initial considerations*

The first step in the traditional process is to define the desired design goals and some basic conditions. This is covered previously in §III.1. From here, the first question to ask is what features in the design are minimally necessary to achieve the objectives. This follows from the concluding principle of (Rams 2013), chief design officer at Braun GmbH from 1961–1995, that "good design is as little design as possible." This principle could be as applicable to aerodynamic design as it is to industrial and product design.

The first step therefore is to define a minimal glove planform that meets all geometric constraints. There are two principal drivers on the choice of glove planform: t/c that can be achieved for a given extension (when considering the OML–OML clearance constraint) and the leading edge sweep.

Looking back on TAMU-06-05, the original reason for the glove extension was to minimize t/c to have a glove that is subcritical to supersonic flow. When the design requirement changed to require $C_\ell \geq 0.5$ instead of $C_\ell \geq 0.3$, it appeared that avoiding supercritical flow was infeasible for a glove of practical length and thickness. However, even despite the elimination of the prime motivation for the extension, TAMU-05-04 and TAMU-06-05 perserved it. As noted by (Liao *et al.* 2012), a likely separation region appears at the inboard fairing in TAMU-06-05, along with a shock and suggesting the fairing needs to be redesigned. When the extension has significant detrimental effect, a valid question arises about whether or not the extension still accomplishes any meaningful design objective.

The extended glove design intrinsically provided a Gaster bump that prevented the turbulent attachment line from the G-III wing from propagating onto the glove attachment line. Some other means of isolation is necessary. Maddalon & Braslow (1990) considered the effectiveness of a three different designs: a Gaster bump, a notch, and a notch bump. Each design can be applied to a designed wing. An alternative option is Gaster's passive suction patch (Gaster 2009). Each of these designs can be applied to a designed wing. Therefore, apart from the $Re_\theta < 100$ constraint on the design, for initial design purposes the attachment line contamination problem can be assumed to be resolved using an "aerodynamic fix" later in the design.

This question of applicability to the design objectives applies equally to the decision to derive Λ_{LE} from a conical planform using the underlying G-III wing as a basis. The ERA requirement specified that $\Lambda_{\text{LE}} \geq 30°$. The planform, by itself, has only a minimal impact on the expected isobar pattern, especially in a glove design. For an "untreated" swept wing of finite span, the isobars would not be expected to approximate the infinite swept isobars (Küchemann 1978). Furthermore, there is no requirement that the isobars follow the sweep of the planform. They more be more swept, or less swept, as observed naturally from the initial loft in TAMU-05-04 and the optimized PDR design in TAMU-06-05.

The hard requirement prescribed by ERA for this experiment is $\Lambda_{\text{LE}} \geq 30°$. Exceeding this sweep can be expected to make the stationary crossflow control problem more challenging, so it would be prudent to design to the minimum required sweep in absence of any compelling reason to exceed it.

The simplest possible planform from which to start the design is given in figure III.21, designated

"TAMU-X". The leading edge of the glove is chosen to follow the G-III leading edge exactly, which requires a minimal spanwise fairing and no leading edge extension. This would be expected to eliminate the separation region due to the accelerated flow on the TAMU-06-05 fairing. The leading edge sweep is therefore equal to the host G-III sweep, $\Lambda_{\text{LE}} = 31.6°$. The starting airfoil is the G-III airfoil with the required offset over the upper surface test section. The truncation location on the pressure side is the same as TAMU-06-05. Most of the G-III wing is a wet wing, but the G-III leading edge for $x/c < 0.08$ is assumed to be nonstructural and removable.
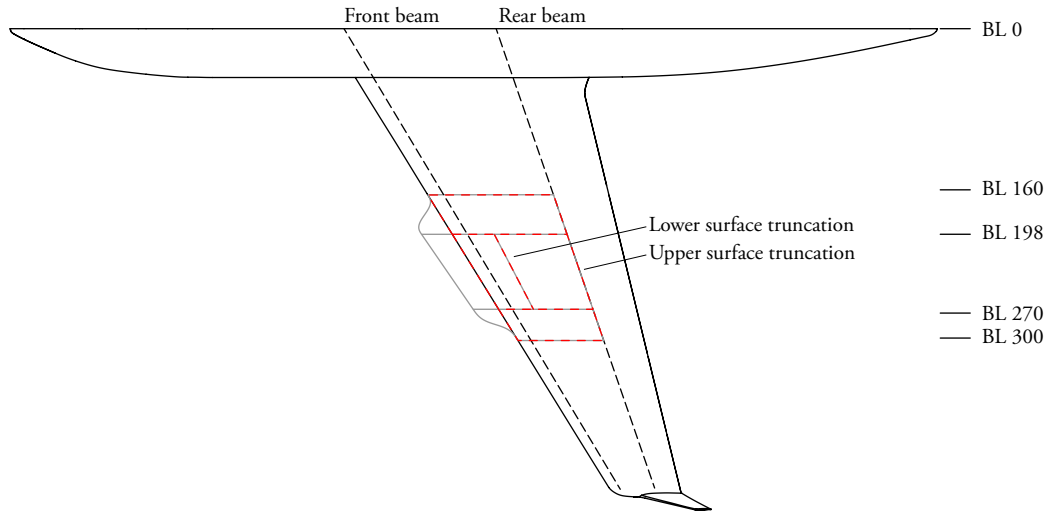
FIGURE III.21. Initial planform layout of TAMU-X wing glove (dashed red line) compared to TAMU-06-05 (solid gray line).

III.5.2. *Process overview*

The detailed wing design process diagrammed in figure III.22 is an specific embodiment of first loop in figure III.3(*a*). This process could used to initiate a design for passing to an optimizer routine. Or, the "manual" process could be continued with increasing levels of fidelity to design completion. If only a single configuration is to be designed, and no available optimizer is trivially configured for the problem, then the latter choice is likely to be an effective use of time and effort. This is of course just one such possible wing design process; any of the tools and methods may be substituted as desired and physically justifiable.

The design starts with the TRANAIR G-III surface grid initially developed in Hartshorn (2011) and used in the optimization of TAMU-06-05. The program POITOP3D (§C.4) converts the TRANAIR POI format grid to PLOT3D format (Walatka, Buning, Pierce & Elson 1990) for use in Pointwise.
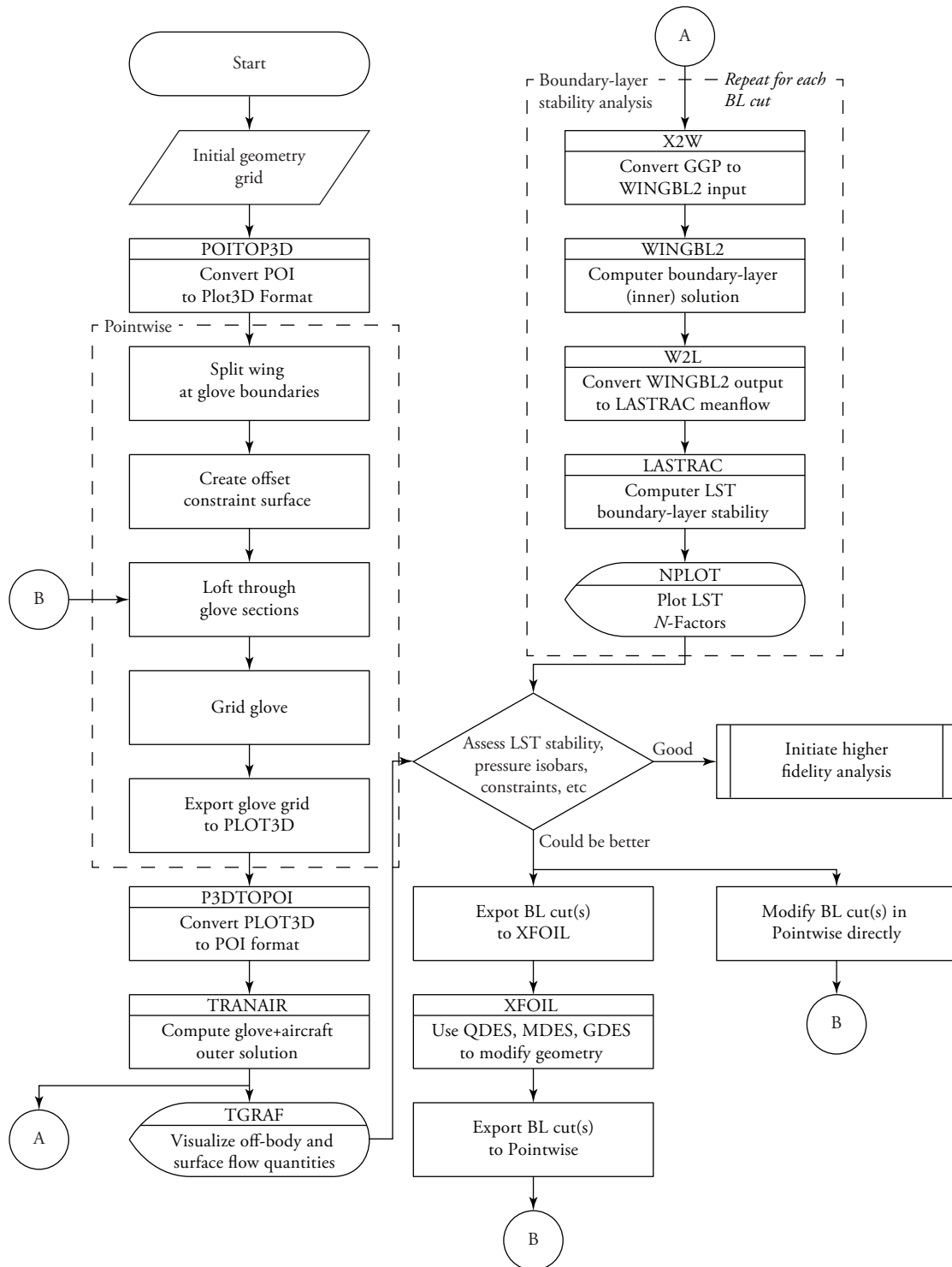
FIGURE III.22. Detailed traditional wing design process in initial stages of a new design.

The TRANAIR grid is broken into networks. The network WINGB defines the glove section of the wing from BL160 to BL300. This is the only grid domain that is modified in Pointwise. When the TAMU-X glove is gridded, the connectors that define the limits of the domain are left unchanged. The TAMU-06-05 glove is deleted and a ruled surface database created that defines the host G-III wing. A 1-inch offset from G-III wing upper surface defines the minimum thickness for the glove test section on the upper surface. This constraint surface has chordwise extent $x/c = [0.08, 0.60]$ of the G-III wing chord and spanwise extent from BL198 to BL270. The imported grid and constrain surfaces are shown in figure III.23.
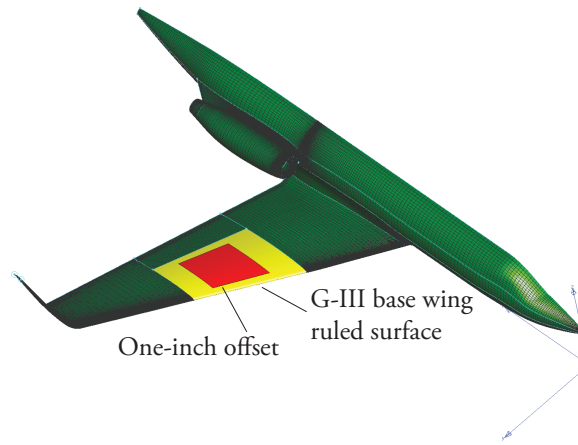
FIGURE III.23. G-III base aircraft grid (green), ruled surface for G-III wing in glove region (yellow) and one-inch offset constraint (red). The forward limit of the one-inch offset is the $x/c = 0.08$ for the host wing.

TAMU-X.i0, the initial starting glove loft shown in figure III.24, is created by lofting approximately through the inboard and outboard bounds of the offset surface. A similar offset from the G-III wing leading edge is the starting point for the leading edge. At this early stage of the design, curvature continuous constraints at the edges of the glove test section are relaxed; they would be included in the next phase of the design when a CAD model becomes the reference geometry instead of the Pointwise model. A CAD tool, such as SolidWorks as used by Roberts (2012), provides more robust control over curvature and tangency constraints than the surface generation facilities in Pointwise. Such control comes with a cost, however, so Pointwise is used here to save time in initial iteration.

The WINGB network is exported in PLOT3D format from Pointwise and P3DTOPOI (§C.3) converts the grid back to the POI format for TRANAIR. TRANAIR is run using largely the same settings as the SARGE optimization cases, with modification to the boundary-layer section for the
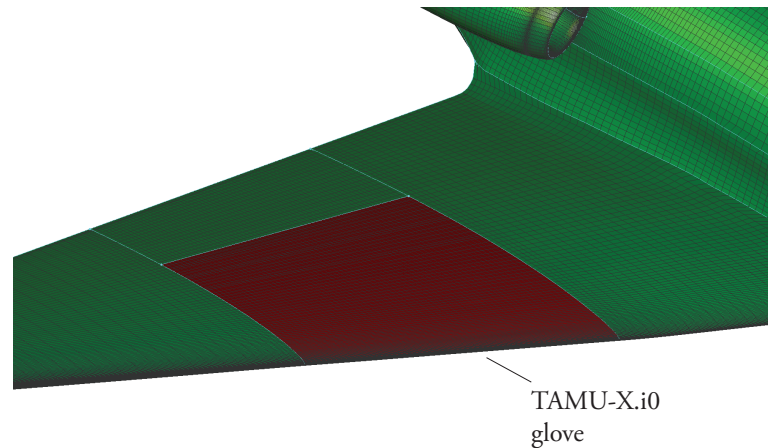
TAMU-X.i0
glove

FIGURE III.24. TAMU-X initial glove loft grid (maroon) integrated with G-III grid (green).

change in glove leading edge sweep and adjustment of the design Reynolds number to $Re_c = 30 \times 10^6$.

The steps in this initial iteration take approximately two hours to perform. Each TRANAIR case is executed on a workstation with a quad-core 2.8 GHz Intel Core i7-860 and 16 GB RAM, which takes approximately 45 minutes for 1200 iterations. Surface pressure isobars are visualized using the TGRAF tool included with TRANAIR.

X2W extracts pressure distributions and geometry at any grid buttline cut from the GGP file output from TRANAIR. XFOIL is again used as in §III.3.1 for geometry manipulation. The resulting coordinates are converted to a segment file for input to Pointwise, converted to an Akima or Bézier curve, relofted into a glove, and output to TRANAIR for analysis of the new configuration.

Initially, two buttline cuts are used at BL198 and BL270, but it is expected that as the design progresses additional cuts will be necessary, especially on the fairings and interior span of the glove. Analysis of a case, modification of two buttline cuts, and configuration of the new case is approximately 2 hours, approximately the same as the initial iteration.

After the design is matured initially using Pointwise's database creation methods, the database segments are output as IGES curves to a CAD model and lofted into a glove that rigidly maintains any specified constraints such as curvature continuity at the fairings. Assuming the CAD model is already configured, incorporating each glove iteration into the CAD model involves slightly more overhead than using Pointwise only—about an additional hour per iteration. Once the CAD model is created, it is the design reference. Since SolidWorks has limited support for outputting discrete points from solid geometry, some interchange between SolidWorks and Pointwise is needed to pass buttline cuts to XFOIL and back if modified using XFOIL instead of directly in SolidWorks. The principal advantage of continuing to use XFOIL is that the connection between the actual 3D flow and the inverse design methods is much closer than with CAD surfacing tools, were the latter have no knowledge of any flow

81

physics. CAD may permit more design freedom than is warranted.

Once the TRANAIR design with a CAD model as the reference advances to a sufficient degree of refinement, then the design advances to a higher fidelity analysis. If issues are identified in the higher fidelity analysis that require significant iteration, then the iteration may return to lower-fidelity methods. Four basic levels of detail might be used in the design process, in order of increasing fidelity:

1. Pointwise geometry, TRANAIR outer solution, WINGBL2 boundary layer
2. CAD geometry, TRANAIR outer solution, WINGBL2 boundary layer
3. CAD geometry, Navier–Stokes outer solution, WINGBL2 boundary layer
4. CAD geometry, Navier–Stokes with refined boundary layer

III.5.3. *Initial iteration results*

The baseline loft case, TAMU-X.i0 produced expectedly poor pressure distributions and need not be analyzed in detail. The critical buttlines on the wing glove are the inboard and outboard junctions of the test section with the fairings: BL198 and BL270, respectively. As with the previous SARGE designs, attention focused on these sections first. After importing the sections into XFOIL, simple favorable pressure gradients were sketched as shown in figure III.25. These pressure distributions are computed in the streamwise direction, without compressibility corrections, and hence are considered unphysically related to the lofted glove at flight condition. Given the efficiency of TRANAIR in analyzing a full 3D configuration, there is little reason to spend much time in 2D analysis other than to determine what changes to make to the 3D glove and rerun the case.

These 2D pressure distributions reflect first order effects when lofted into a glove and the full-aircraft flowfield is calculated in TRANAIR. The resulting isobars for this configuration after 1200 iterations in TRANAIR are shown in figure III.26, along with the 3D pressure slices in figure III.27. On the suction side, the isobars are promising for $x/c < 0.2$ across the entire span. Outboard of approximately the glove midspan at BL234, the isobars appear similarly conducive to spanwise uniformity.

A few potential options to improve the spanwise uniformity on the suction side might include the following:

1. Thicken the inboard section. A modest amount of thickness or camber is likely to accelerate the suction side pressure distribution at BL198 until it matches BL270. At the point that BL198 and BL270 match, then there is no particular reason that there should be expected to be significant differences for a straight loft between them.
2. Thinning the outer section, which is not physically possible without extending the glove forward. Since the current sweep is $\Lambda_{\text{LE}} = 31.6°$, some extension at the outer section is permitted until the sweep reaches $\Lambda_{\text{LE}} = 30°$.
3. Move the max thickness of the outer section aft. Due to constraints imposed by the host wing, this is essentially infeasible as well.
4. Isolate the glove in some manner from the host wing. Some amount of the variation in spanwise
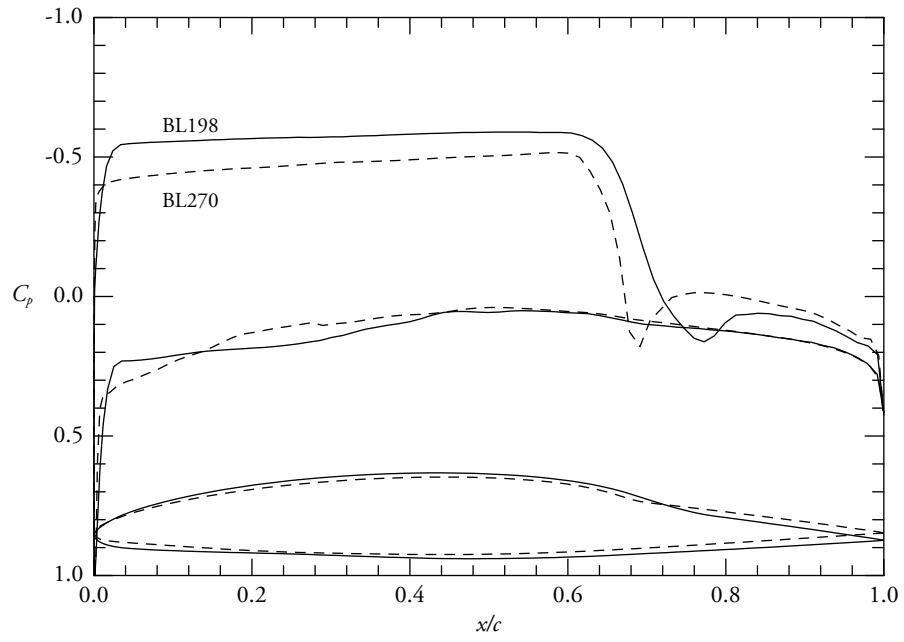
FIGURE III.25. XFOIL C_p and airfoil cuts for TAMU-X.i1 at BL198 (solid line) and BL270 (dashed line).
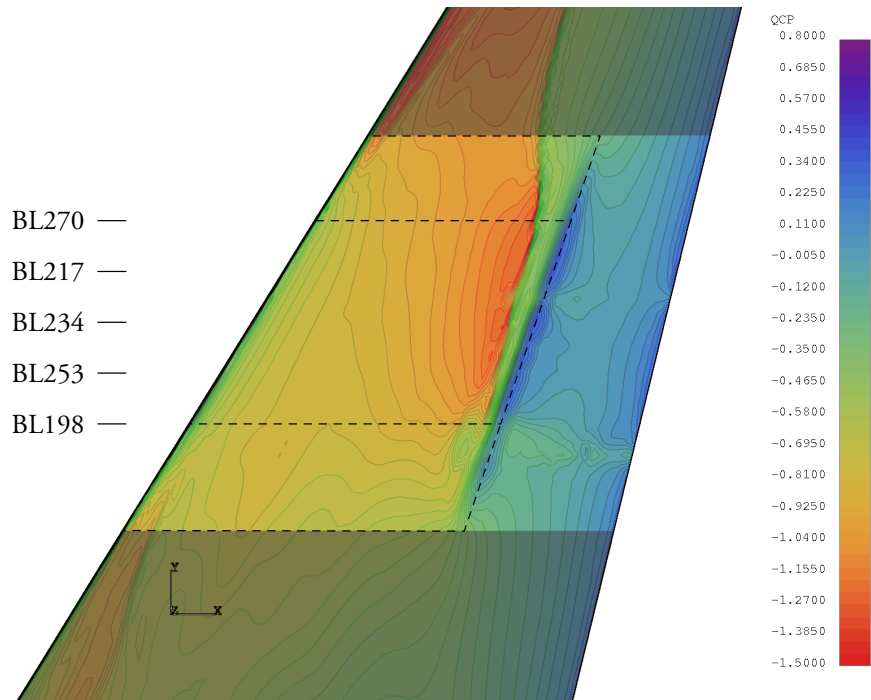
FIGURE III.26. C_p isobars on TAMU-X.i1, suction side.
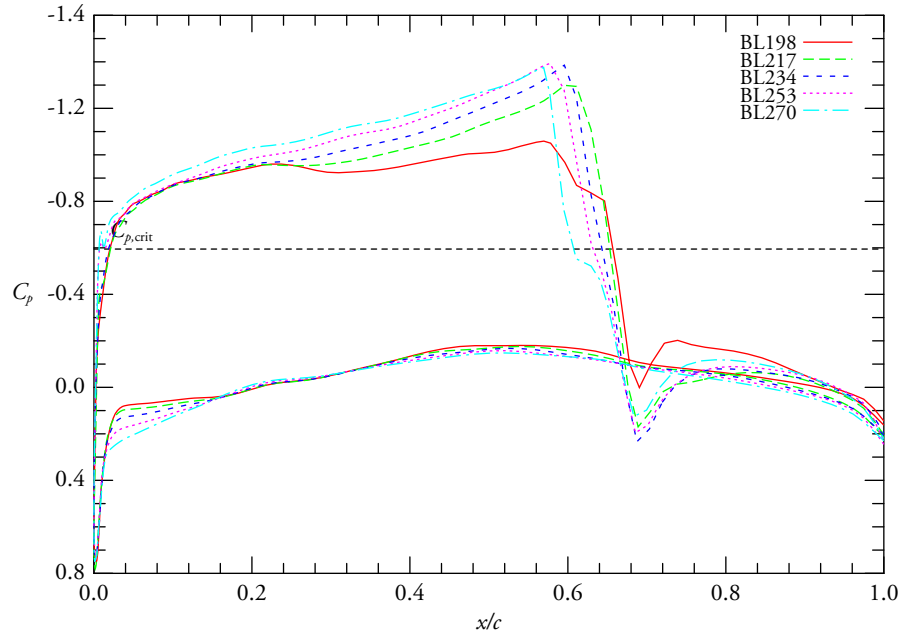
FIGURE III.27. C_p buttline cuts on TAMU-X.i1, suction side.

uniformity over the test section appears to carry over from matching the inboard and outboard conditions on the G-III wing. Perhaps an abrupt glove transition, rather than a smooth one as has been assumed, could facilitate a "reset" of the flow over the glove.

The pressure side needs only modest changes, and can likely be addressed as an afterthought.

Obviously, this initial iteration is in any sense a completed design. Qualitatively, the first iteration through this process has advanced this planform from inception to a level that would approach that of TAMU-05-04. A few (five to ten) more iterations, when executed by a graduate student familiar with the process and the basics of finite wing design, would probably be fruitful before the design is passed to more detailed analysis or an optimizer.

Since TAMU-X is not a design needed for any purpose, this initial iteration serves mainly to demonstrate the feasibility of the process to rapidly initiate new design planform and posit one possible alternative approach to the PDR SARGE configuration, where the problem to be considered again. Were this an entirely new case, on an another aircraft, or a full aircraft, or a wind tunnel model, then some additional preparation work would be required, such as the gridding of the complete geometry and configuration of the TRANAIR input file, but is not considered to be burdensome.

CHAPTER IV

CONCLUSIONS AND FUTURE WORK

The assessment by Küchemann (1978) that aerodynamic design is as much as art is a science seems to be validated by the SARGE design experience. Given the complexity of the Navier–Stokes equations, it is unlikely that a single design is necessarily the "best" design, or that a single process can cover all cases. The process presented in §III.5 is one process that works for the SARGE design and would have likely saved time and effort in the beginning phases of the design had all the tools (i.e. TRANAIR and Pointwise) been available at the start. This process is likely to require modifications for any other design. The necessary adjustments can be determined only through a comprehensive, informed assessment of the design objectives, constraints, and political environment.

The journey to TAMU-06-05 reinforced the idea that the availability of advanced design tools are no substitute for physical understanding of the flow behavior. The Navier–Stokes equations are sufficiently complex such that no current design tool can be reasonably employed to produce an efficient design unless the designer understands the physics underlying the problem and is able to guide the design towards a workable solution. Even so, understanding the physics is merely a necessary condition for a successful design; it is not sufficient. A certain amount of ingenuity is also required for success.

Passive SWLFC is one of the most challenging current problems in aerodynamic design. A plethora of issues remain to be solved in order to achieve SWLFC on operational aircraft. This work developed and documented a feasible, efficient process to develop such a design. Fundamentally, there must be a process to design the wing or test article to successfully mature the technology.

IV.1. Optimization and traditional wing design

The tradeoffs and interactions in using an optimizer to finalize the design and approaching the problem using the a traditional design approach is one sense a choice of where to accumulate and apply knowledge to advance the design. Once configured, the optimization algorithm advances with well-understood mathematical methods but little physical insight (apart from an adjoint or gradient to guide the solution to the objective minimum, a necessity in aerodynamic optimization). Internal to the optimization algorithm are computations on many intermediate designs that are practically useless and perhaps would not be considered at all by an experienced designer. A designer who understands the myriad nuances of the 3D problem could almost certainly achieve a good design in an amount of time comparable to what it takes to configure the optimizer and run the case. This fact is especially true if an nearly-complete optimization framework is not available, as it wasn't for most of this design until TAMU acquired TRANAIR. TRANAIR is an effective code developed specifically for aerodynamic design and

optimization, as expected since The Boeing Company developed (in conjunction with NASA) and extended it for their purposes in commercial aircraft design. Given the variety of similar wing-body-tail models aircraft Boeing produces, automating the aerodynamic design process makes practical sense. For a single design like that in this experiment, optimization may not be necessary.

The wing design process that was well established by the 1970s, at least, is still useful. In the days before even the most powerful computers struggled to solve simplified flow problems that a desktop computer today can solve in seconds, developing efficient methods that made maximal use of physical insight was critically important. That knowledge is still important today, especially in the development of advanced methods that automate some steps in the process. In a sense, we can never expect that we will completely human interaction in aerodynamic design. A naïvely implemented method has the potential to simply make bad decisions faster and more often.

An important question can be asked about how much should be automated. Amoignon *et al.* (2006) considered an objective function that uses laminar flow *N*-factors, which is a straightforward proposition in 2D airfoil design when only TS instability need be considered. What would the objective function be for DRE design? One could define some objective, say that the *N*-factors follow some sort of envelope, allow for DRE control, and that the envelope is uniform across the span of the wing. Unfortunately, that ideal details of such an envelope for effective DRE control is not yet established and computational methods are not currently able to define it. Optimization in this manner would merely demonstrate that one can produce a geometry with a given envelope, not that the envelope in question is conducive to promoting laminar flow.

In the aerodynamic design of a production vehicle, the objective function might be related to cost or performance. For example, empty weight is simplistically considered analogous to the fixed costs of an airplane. An optimum design in this sense would be one that minimizes the aircraft empty weight without violating any constraints. Using a carpet plot as in figure III.1, this is a problem that is conceptually straightforward.

In technology development, where there is no operational vehicle, there is no corresponding sense of a optimum design. The primary consideration is answering the question "Will this design lead to a flight experiment that successfully matures the technology?" Unfortunately, the available tools for SWLFC design are limited in quantitatively making that assessment, given the complexity inherent in our current understanding of the transition-to-turbulence process.

IV.2. Alternatives in aerodynamic design

An aerodynamic design is never truly an global optimum. It is simply a design that meets the design objectives without violating any constraints. There is no guarantee that the final design is the only design approach that could fulfill the mission or that another way of approaching the problem would not be feasible.

This is the idea preliminarily demonstrated by TAMU-X, which can likely be shown to be feasible and meet all the design objectives. One difference between the approach taken in TAMU-06-05 and that in TAMU-X is the way the question regarding the extension was posed. In the former, the question related to the extension was "how far can we go?" because the belief was that minimal thickness was desirable to avoid transonic flow. An answer obtained through structural and loads analysis in collaboration with DFRC was a few dozen inches.

In order to address a potential aerodynamic problem related to the extension, the TAMU-X planform approached the problem from a different direction, asking "how far do we need to go?" For the first iteration, the answer was taken to be zero inches to evaluate whether or not any extension is necessary. If this design were matured further, it's likely that some extension would be necessary, perhaps only as much at the outboard section to reduce the Λ_{LE} to the minimum requirement and perhaps to permit some thinning at that section.

This is a quintessential feature of the aerodynamic design problem: where the optimization algorithm was focused on relatively small changes (on the order of inches) to make a non-spanwise uniform flow more uniform, a large design change (on the order of tens of inches) can likely achieve a design that also fulfills the mission.

Regardless, in either case the maximum extension has been shown to be able to meet all the ERA objectives without violating any constraints. It is likely that the minimum extension could be shown to do so as well. Which one would be desirable is best left as a question for the designer to answer, but it would be better to flight test a design to answer the critical questions that cannot be answered computationally rather than iterate the design until the end of time.

IV.3. Future work

The methods used in this work are by no means claimed to an ultimate solution to the problems in SWLFC design. The following sections summarize three areas for future development: development of airfoils and target pressure distributions, improvements that could be made to the optimization approach, and—most importantly—a brief reminder that understanding of the transition process and means for prediction the location where it leads to turbulence is a fundamental difficulty preventing achievement of laminar flow on operational designs.

IV.3.1. *Airfoil and target pressure development*

The wing design process in §III.5 is efficient largely due to the automation of a number of steps that involve routine manual labor. A few steps could be improved. The impetus for the B-spline method for construction C_p distributions was an attempt to improve upon the facilities provided by XFOIL, which sometimes encounters curve-fitting difficulty with the steep gradient required by SWLFC design near the leading egde.

This method was not quite successful in this regard, although it was successfully employed to develop the objective function for TAMU-06-05. Not much time was saved by neglecting physical geometry. It is possible that by doing so a target distribution was generated that could not be physically realized in the 3D problem anywhere on the glove without violating a constraint. Thus, an improved method would maintain relevance to physical airfoil, in 3D if possible, even if that airfoil isn't used in the optimization. Better still would be if the target C_p is known to be feasible somewhere on the 3D glove.

Another improvement to the method would be to design the C_p in terms of Re_x rather than x/c. This partially follows from the modification to the optimization method carried out by Tufts *et al.* (2013), where the pressure isobars were optimized to follow an infinite swept wing planform rather than a conical planform. If multiple buttline airfoil cuts were to be designed instead of using an optimizer, it is likely that designing the pressure distributions in dimensional or Re_x terms could result in better uniformity. Additionally, as Re_c becomes large, it becomes harder to design a suitable initial pressure slope using x/c ordinate. With an Re_x ordinate, and considering the assumed nature of the assumed boundary-layer flow, designing a pressure gradient to achieve a given $Re_{x,\text{tr}}$ may not be any harder at $Re_c = 50$ million than it is at $Re_c = 30$ million.

In the optimization algorithm, the geometry was parameterized in terms of upper and lower X coordinates based on the geometrical planform. This choice makes sense for interaction with other disciplines and manufacturing purposes. However, there is little incentive in aerodynamic design to use such a parameterization. Whereas an arc-length parameter is smoothly distributed along the airfoil arc, X becomes problematic in the regions of high curvature near the leading edge. Thus, an alternative parameterization, perhaps an extension of the CST, should be considered that defines the airfoil surface in terms of single arc length for entire airfoil surface. According to Young (2011), such a method has been developed at Boeing and has advantages for aerodynamic optimization, but the details have not been published publicly.

IV.3.2. *Boundary-layer stability coupling in optimization*

Even though the method for developing a target pressure distribution can be improved, there is probably no reason to manually design a pressure distribution or to use it as an intermediate manual step in the optimization process. Such an activity makes the objective function for the optimizer complex due to the large number of points that need to be evaluated to determine the value of the objective.

The optimizer could be directly coupled to boundary layer stability, rather than using C_p as an intermediate step. For DRE design, despite the previously mentioned caveats about the uncertainty about the ideal N-factor envelope for effective DRE control, one possibility would be to consider at two least two values in the objective, using values suitable for the specific design under consideration:

1. the location where λ_2 reaches the selected value for N_{tr}; and
2. the location where λ_1 reaches $N = 6$, perhaps around $x/c = 0.3$.

Such work follows from Amoignon *et al.* (2006), who considered shape optimization of 2D natural laminar flow airfoils. For this to be done efficiently for 3D boundary layers, if numerous flow iterations are to be performed, a surrogate stability model such as that of Rajnarayan & Sturdza (2011) could be implemented to reduce the overhead involved in performing a full boundary-layer stability analysis.

IV.3.3. *Transition prediction*

Transition "prediction" in this work relied extensively on the e^N method and LST stability to make a qualitative estimate of the transition location. In 3D boundary layers, this estimate is expected to vary from the actual situation by a panoply of factors that will not be known until the experiment is carried out, such as surface roughness and freestream turbulence characteristics.

One reason that drives the use of LST in the early design phase is that a single, deterministic answer that can be efficiently calculated. The LST approach has limitations, most notably neglecting the influence of non-parallel, curvature, and nonlinear effects. For a low subsonic case like SWIFT, it appears to be sufficient to predict transition.

Some effort was made during the SARGE design to consider curvature and nonparallel effects via the linear PSE. However, the use of the PSE in design is problematic, largely because of the question of how to initiate the computation. Depending on the selected method for initiating the linear PSE, widely varying *N*-factors can be achieved.

According to Herbert (1997), "the problems in practical applications, however, are neither the PSE nor their implementation. The problem is finding the proper input for PSE runs." If you have the freestream environment, and have a experimental basis to know which modes to discard, then the PSE will give effective disturbance growth rates. However, the initial conditions in a nonlinear dynamical system may never truly be known and perhaps development of approach similar to that used for weather forecasting (see e.g. ch. 4 Silver 2012) may be warranted.

A complete design case would consider many iterations. It is impractical to use the linear PSE exclusively when iteration might require special care to ensure that a good mode is selected. "Qualitative" estimates of the downstream influence of curvature and nonparallel effects can be obtained using the LST eigenfunctions as initial conditions for the PSE, but this does little to address an important question for DREs: the location of the neutral stability point for the control mode, which may vary if curvature effects are included.

When validating to flight experiments, the PSE has been found to be in good agreement. At the design stage, however, the experiment does not yet exist. Surface roughness (which provides the initial disturbance amplitudes for stationary crossflow modes) will depend on the specific test article manufactured and installed. Freestream disturbances are dependent on the flight environment, and have been to date insufficiently characterized to determine a general model of the flight disturbance environment.

As pointed out by Roach (2009), the "failure to achieve a solution ... is not the same, nor as

dangerous, as achieving a false solution." While the spurious PSE modes are not mathematically wrong—they are valid solutions of the equations—they are physically suspect. Given the number of unknowns in the design stage, LST appears to be the preferred choice. It may better to have one answer, robustly determined with known limitations, than to have many answers with unknown features and validity.

The PSE can be used as a check, as it was for TAMU2D-03A and TAMU2D-04 to qualitatively identify possible issues, but needs further study and attention to give a consistent, trustworthy answer in the design space under consideration before it should be used in the regular course of design decisions. Herbert (1997) notes that "In the hands of an applied mathematician the PSE approach can probably be improved beyond its current capabilities."

REFERENCES

AMOIGNON, O., PRALITS, J., HANIFI, A., BERGGREN, M. & HENNINGSON, D. 2006 Shape optimization for delay of laminar–turbulent transition. *AIAA Journal* **44** (5), 1009–1024.

ANDERS, S. G. & FISCHER, M. C. 1999 F-16XL-2 supersonic laminar flow control flight test experiment. *NASA Technical Publication* TP-1999-209683.

ANDERSON, B. T. & MEYER, JR., R. R. 1990*a* Effects of wing sweep on boundary-layer transition for a smooth F-14A wing at Mach numbers from 0.700 to 0.825. *NASA Technical Memorandum* 101712.

ANDERSON, B. T. & MEYER, JR., R. R. 1990*b* Effects of wing sweep on in-flight boundary-layer transition for a laminar flow wing at Mach numbers from 0.60 to 0.79. *NASA Technical Memorandum* 101701.

ANDERSON, JR., J. D. 2003 *Modern Compressible Flow*, 3rd edn. New York, N. Y.: McGraw-Hill.

ANDERSON, JR., J. D. 2011 *Introduction to Flight*, 7th edn. New York, N. Y.: McGraw-Hill.

ANSYS, INC. 2010 *ANSYS FLUENT theory guide: release 13.0*. ANSYS, Canonsburg, Va.

ARCARA JR, P. C., BARTLETT, D. W. & MCCULLERS, L. A. 1991 Analysis for the application of hybrid laminar flow control to a long-range subsonic transport aircraft. *SAE Paper* 912113.

ARNAL, D. 1994 Etude des possibilités de réduction de la traînée par laminarisation. In *Proceedings of 7th European Aerospace Conference*. Labège, France.

ARNAL, D. & ARCHAMBAUD, J. P. 2008 Laminar-turbulent transition control: NLF, LFC, HLFC. In *Advances in Laminar-Turbulent Transition Modelling*, *NATO Educational Notes* RTO-EN-AVT-151, pp. 15-1–15-22.

ARNAL, D. & BULGUBURE, C. 1990 Drag reduction by boundary layer laminarization. *La Recherche aérospatiale* **1990-3**, 157–165.

ARNAL, D., CASALIS, G. & HOUDEVILLE, R. 2008*a* Practical transition prediction methods: Subsonic and transonic flows. In *Advances in Laminar-Turbulent Transition Modelling*, *NATO Educational Notes* RTO-EN-AVT-151, pp. 7-1–7-34.

ARNAL, D., HABIBALLAH, M. & COUSTOLS, E. 1984 Théorie de l'instabilité laminaire et critères de transition en écoulement bi- et tridimensionnel. *La Recherche aérospatiale* **1984-2**, 125–143.

ARNAL, D., PERRAUD, J. & SÉRAUDIE, A. 2008*b* Attachment line and surface imperfection problems. In *Advances in Laminar-Turbulent Transition Modelling*, *NATO Educational Notes* RTO-EN-AVT-151, pp. 9-1–9-20.

BASSOM, A. P. & HALL, P. 1991 Vortex instabilities in three-dimensional boundary layers: the relationship between Görtler and crossflow vortices. *Journal of Fluid Mechanics* **232**, 647–680.

BAUMANN, E. 2011 Subsonic Aircraft Roughness Glove Experiment (SARGE) objectives and requirements document (ORD) & levels I & II system requirements specification (SRS) draft. *NASA Dryden Flight Research Center Report* 804-DRE-101-ORD-005.00.

BELISLE, M. J., MARTINEZ, I., BAUMES, III, P., ROSE, C. P. & SALEM, J. 2005 überBœuf: A super-jumbo airliner proposal. Senior design report, Arizona State University, Tempe, Ariz.

BELISLE, M. J., NEALE, T. P., REED, H. L. & SARIC, W. S. 2010 Design of a swept-wing laminar flow control flight experiment for transonic aircraft. *AIAA Paper* 2010-4381.

BELISLE, M. J., ROBERTS, M. W., TUFTS, M. W., TUCKER, A. A., WILLIAMS, T. C., SARIC, W. S. & REED, H. L. 2011 Design of the Subsonic Aircraft Roughness Glove Experiment (SARGE). *AIAA Paper* 2011-3524.

BELISLE, M. J., ROBERTS, M. W., WILLIAMS, T. C., TUFTS, M. W., TUCKER, A. A., SARIC, W. S. & REED, H. L. 2012 A transonic laminar-flow wing glove flight experiment: Overview and design optimization. *AIAA Paper* 2012-2667.

BERTOLOTTI, F. P. & HERBERT, T. 1991 Analysis of the linear stability of compressible boundary layers using the PSE. *Theoretical and Computational Fluid Dynamics* **3** (2), 117–124.

BERTOLOTTI, F. P., HERBERT, T. & SPALART, P. R. 1992 Linear and nonlinear stability of the Blasius boundary layer. *Journal of Fluid Mechanics* **242**, 441–474.

BLASIUS, H. 1908 The boundary layers in fluids with little friction. *NACA Technical Memorandum* 1256. Translation of Grenzschivchten in Flüssigkeiten mit kleiner Reibung, *Zeitschrift für Mattematik und Physik*, Band 56, Heft 1, 1908.

BOEING COMMERCIAL AIRPLANE COMPANY 1984 F-111 natural laminar flow glove flight test data analysis and boundary layer stability analysis. *NASA Contractor Report* 166051.

BOEING COMMERCIAL AIRPLANE COMPANY 1987*a* Flight survey of the 757 wing noise field and its effects on laminar boundary layer transition, Volume I—Program description and data analysis. *NASA Contractor Report* 178216.

BOEING COMMERCIAL AIRPLANE COMPANY 1987*b* Flight survey of the 757 wing noise field and its effects on laminar boundary layer transition, Volume II—Data compilation. *NASA Contractor Report* 178217.

BOEING COMMERCIAL AIRPLANE COMPANY 1988 Flight survey of the 757 wing noise field and its effects on laminar boundary layer transition, Volume III—Extended data analysis. *NASA Contractor Report* 178419.

BOEING COMMERCIAL AIRPLANE GROUP 1993 High Reynolds number hybrid laminar flow control (HLFC) flight experiment final report, Volume I, Flight test program. *Boeing Report* D6-55648-1.

BOEING COMPANY 2006 737 next-generation performance summary. boeing.com/assets/pdf/commercial/startup/pdf/737ng_perf.pdf, accessed April 30, 2013.

BOEING COMPANY 2007 *TRANAIR user's manual*. Boeing, Seattle, Wash.

BOGUE, D. & CRIST, N. 2008 CST transonic optimization using Tranair++. *AIAA Paper* 2008-321.

BRADY, C. 2013 Boeing 737 technical site: wing design. b737.org.uk/flightcontrols.htm #Wing_Design, accessed April 30, 2013.

BRANDON, J. M., MANUEL, G. S., WRIGHT, JR., R. E. & HOLMES, B. J. 1990 In-flight flow visualization using infrared imaging. *Journal of Aircraft* **27** (6), 612–618.

BRASLOW, A. L. 1999 *A history of suction-type laminar-flow control with emphasis on flight research*. *Monographs in Aerospace History* 13. Washington, D. C.: NASA.

BRASLOW, A. L., MADDALON, D. V., BARTLETT, D. W., WAGNER, R. D. & COLLIER, JR, F. S. 1990 Applied aspects of laminar-flow technology. In *Viscous drag reduction in boundary layers* (ed. D. M. Bushnell & J. N. Hefner), *Progress in Aeronatuics and Astronautics*, vol. 1, pp. 47–48. New York, N. Y.: AIAA.

BULGUBURE, C. & ARNAL, D. 1992 Dassault Falcon 50 laminar flow flight demonstrator. In *First European Forum on Laminar Flow Technology*, *DGLR-Bericht* 92-06, pp. 11–18. Bonn, Germany:

DGLR.

CARPENTER, A. L. 2009 In-flight receptivity experiments on a 30-degree swept-wing using micron-sized discrete roughness elements. PhD thesis, Texas A&M University, College Station, Tex.

CARPENTER, M. H., CHOUDHARI, M., LI, F., STREETT, C. L. & CHANG, C.-L. 2010 Excitation of crossflow instabilities in a swept wing boundary layer. *AIAA Paper* 2010-378.

CHANG, C.-L. 2003 The Langley Stability and Transition Analysis Code (LASTRAC): LST, linear & nonlinear PSE for 2D, axisymmetric, and infinite swept wing boundary layers. *AIAA Paper* 2003-0974.

CHANG, C.-L. 2004 Langley Stability and Transition Analysis Code (LASTRAC) version 1.2 user manual. *NASA Technical Manual* TM-2004-213233.

COLEMAN, W. S. 1961 Roughness due to insects. In *Boundary Layer and Flow Control*, vol. 2 (ed. G. V. Lachmann), pp. 682–747. Oxford, United Kingdom: Pergamon Press.

COLLIER, JR., F. S. 1993 An overview of recent subsonic laminar flow control flight experiments. *AIAA Paper* 1993-2987.

COLLIER, JR., F. S. 2010 Overview of NASA's Environmentally Responsible Aviation (ERA) project. Invited presentation at the 48th AIAA Aerospace Sciences Meeting. Orlando, Florida.

COURTY, J. P., BULGUBURE, C. & ARNAL, D. 1993 Studies on laminar flow conducted at Dassault Aviation, calculations and test flights. In *AGARD Conference Proceedings*, AGARD-CP 547.

CUMPSTY, N. A. & HEAD, M. R. 1967 The calculation of three-dimensional turbulent boundary layers— Part II: Attachment-line flow on an infinite swept wing. *The Aeronautical Quarterly* **18**, 150–164.

DEYHLE, H. & BIPPES, H. 1996 Disturbance growth in an unstable three-dimensional boundary layer and its dependence on environmental conditions. *Journal of Fluid Mechanics* **316**, 73–113.

DRAKE, A. & SOLOMON, JR., D. 2010 Flight testing of a 30-degree sweep laminar flow wing for a high-altitude long-endurance aircraft. *AIAA Paper* 2010-4571.

DRELA, M. 1989 XFOIL—an analysis and design system for low reynolds number airfoils. *Low Reynolds Number Aerodynamics* pp. 1–12.

DRELA, M. & GILES, M. B. 1987a A two-dimensional transonic aerodynamic method. *AIAA Journal* **25** (9), 1199–1206.

DRELA, M. & GILES, M. B. 1987b Viscous–invsiscid analysis of transonic and low Reynolds number airfoils. *AIAA Journal* **25** (10), 1347–1355.

DRESSLER, U., HANSEN, H., RILL, S., HORSTMANN, K. H., ROHARDT, C. H. & WICHMANN, G. 1992 Design of the Fokker F100 natural laminar flow glove. In *First European Forum on Laminar Flow Technology*, DGLR-Bericht 92-06, pp. 152–163. Bonn, Germany: DGLR.

ELSENAAR, A. & HAASNOOT, H. A. 1992 A survey on Schipol airport of the contamination of wing leading edges of three different aircraft types under operating conditions. In *First European Forum on Laminar Flow Technology*, DGLR-Bericht 92-06, pp. 256–261. Bonn, Germany: DGLR.

EPPLER, R. & SOMERS, D. M. 1980 A computer program for the design and analysis of low-speed airfoils. *NASA Technical Memorandum* 80120.

FEAGIN, R. C. & MORRISON, W. D. 1978 Delta method, an empirical drag buildup technique. *NASA Contractor Report* 151971.

GASTER, M. 1967 On the flow along swept leading edges. *The Aeronautical Quarterly* **18**, 165–184.

GASTER, M. 2009 Establishment of laminar boundary layer flow on an aerofoil body. *European Patent* EP2091814B1.

GILL, P. E., MURRAY, W., SAUNDERS, M. A. & WRIGHT, M. H. 1998 *User's guide for NPSOL (version 4.0): a FORTRAN package for nonlinear programming*. Stanford Business Software, Palo Alto, Calif.

GRAY, W. E. 1952 The effect of wing sweep on laminar flow. *Royal Aircraft Establishment Technical Memorandum* 255.

GREEN, J. E. 2008 Laminar-flow control—back to the future? *AIAA Paper* 2008-3738.

GUBISCH, M. 2011 Go with the flow. *Flight International,* 26 July–1 August, pp. 24–26.

HALL, P. 1985 The gortler vortex instability mechanism in three-dimensional boundary layers. *Proceedings of the Royal Society of London. A.* **399**, 135–152.

HARTSHORN, F. 2011 Analysis of asymmetric aircraft aerodynamics due to an experimental wing glove. *AIAA Paper* 2011-3352.

HARTSHORN, F., BELISLE, M. J. & REED, H. L. 2012 Computational optimization of a natural laminar flow experimental wing glove. *AIAA Paper* 2012-0870.

HAYNES, T. S. & REED, H. L. 2000 Simulation of swept-wing vortices using nonlinear parabolized stability equations. *Journal of Fluid Mechanics* **405**, 325–349.

HENKE, R., CAPBERN, P., DAVIES, A. J., HINSINGER, R. & SANTANA, J. L. 1996 The "A320 HLF fin programme:" objectives and challenges (invited). In *Abstracts of the Second European Forum on European Flow Technology*, pp. 12.3–12.11. Brussels, Belgium: Council of European Aerospace Societies.

HERBERT, T. 1997 Parabolized stability equations. *Annual Review of Fluid Mechanics* **29**, 245–283.

HORSTMANN, K. H. & KÖRNER, H. 1996 Natural laminar flow flight test investigation for commuter aircraft application (invited). In *Abstracts of the Second European Forum on European Flow Technology*, pp. 2.19–2.30. Brussels, Belgium: Council of European Aerospace Societies.

HORSTMANN, K. H., REDEKER, G. & QUAST, A. 1990 Flight tests with a natural laminar flow glove on a transport aircraft. *AIAA Paper* 1990-3044.

HUMPHREYS, B. 1992 Contamination avoidance for laminar flow surfaces. In *First European Forum on Laminar Flow Technology*, *DGLR-Bericht* 92-06, pp. 262–269. Bonn, Germany: DGLR.

HUNT, L. E. & SARIC, W. S. 2011 Boundary-layer receptivity of three-dimensional roughness arrays on a swept-wing. *AIAA Paper* 2011-3881.

JOSLIN, R. D. 1998 *Overview of laminar flow control*. *NASA Technical Publication* TP-1998-208705.

KNIGHT, B. C. J. G. & STANDFAST, A. F. B. 1968 Directions to contributors. *The Journal of General Microbiology* **51** (1).

KOSIN, R. E. 1965 Laminar flow control by suction as applied to the X-21A airplane. *Journal of Aircraft* **2** (5), 384–390.

KÜCHEMANN, D. 1978 *The Aerodynamic Design of Aircraft*. Oxford, United Kingdom: Pergamon Press.

KULFAN, B. M. 2007 A universal parametric geometry representation method—CST. *AIAA Paper* 2007-62.

KULFAN, B. M. & BUSSOLETTI, J. E. 2006 Fundamental parametric geometry representations for aircraft component shapes. *AIAA Paper* 2006-6948.

Laintone, E. V. 1951 New compressibility correction for two-dimensional subsonic flow. *Journal of the Aeronautical Sciences* **18** (5), 350.

Landis, T. 2010 DRELFGE laminar-flow experiment. *NASA DFRC Graphic* ED10-0097-22.

Landis, T. 2012 Gulfstream III aerodynamics research test bed. *NASA DFRC Graphic* ED12-0191-12.

Li, F., Choudhari, M., Carpenter, M., Malik, M. R., Chang, C.-L. & Streett, C. 2010 Roughness based crossflow transition control for a swept airfoil design relevant to subsonic transports. *AIAA Paper* 2010-4380.

Li, F., Choudhari, M., Chang, C.-L., Streett, C. & Carpenter, M. 2011 Computational modeling of roughness-based laminar flow control on a subsonic swept wing. *AIAA Journal* **49** (3), 520–529.

Liao, W., Malik, M. R., Lee-Rausch, E. M., Li, F., Nielsen, E. J., Buning, P. G., Chang, C.-L. & Choudhari, M. 2012 Boundary-layer stability analysis of the mean flows obtained using unstructured grids. *AIAA Paper* 2012-2690.

Lin, R. S. & Reed, H. L. 1993 Effect of curvature on stationary crossflow instability of a three-dimensional boundary layer. *AIAA Journal* **31** (9), 1611–1617.

Mack, L. M. 1979 On the stability of the boundary layer on a transonic swept wing. *AIAA Paper* 1979-0264.

Mack, L. M. 1984 Special course on stability and transition of laminar flow. *AGARD Report* 709.

Maddalon, D. V. & Braslow, A. L. 1990 Simulated-airline-service flight tests of laminar-flow control with perforated-surface suction system. *NASA Technical Paper* 2966.

Malik, M. R. & Balakumar, P. 1993 Linear stability of three-dimensional boundary layers- effects of curvature and non-parallelism. *AIAA Paper* 1993-0079.

Malik, M. R., Liao, W., Lee-Rausch, E., Li, F., Choudhari, M. & Chang, C.-L. 2011 Computational analysis of the G-III laminar flow glove. *AIAA Paper* 2011-3525.

Malik, M. R., Liao, W., Li, F. & Choudhari, M. 2013 DRE-enhanced swept-wing natural laminar flow at high Reynolds numbers. *AIAA Paper* 2013-0412.

Mankins, J. C. 1995 *Technology readiness levels: a white paper*. Washington, D. C.: Office of Space Access and Technology, Advanced Concepts Office, NASA.

Marshall, L. A. 1999 Boundary-layer transition results from the F-16XL-2 supersonic laminar flow control experiment. *NASA Technical Memorandum* TM-1999-209013.

Marshall, L. A. 2000 Summary of transition results from the F-16XL-2 supersonic laminar flow control experiment. *AIAA Paper* 2000-4418.

Mavris, D. N., Saric, W. S., Ran, H., Belisle, M. J., Woodruff, M. J. & Reed, H. L. 2010 Investigation of a health monitoring methodology for future natural laminar flow transport aircraft. In *Proceedings of the 27th International Council of the Aeronautical Sciences*, *Paper* 2010-1.9.3.

Morkovin, M. V., Reshotko, E. & Herbert, T. 1994 Transition in open flow systems—a reassessment. *Bulletins of the American Physical Society* **39** (9), 1882.

NASA 1998 Gulfstream II 3-view. *NASA DFRC Graphic* EG-0050-01.

NASA 2013 FUN3D manual. fun3d.larc.nasa.gov, accessed July 4, 2013.

Neale, T. P. 2010 CFD investigations of a transonic swept-wing laminar flow control flight experiment. Master's thesis, Texas A&M University, College Station, Tex.

Obara, C. J. & Holmes, B. J. 1985 Roughness and waviness requirements for laminar flow surfaces. In *Langley Symposium on Aerodynamics* (ed. S. H. Stack), *NASA Conference Publication* 2397, pp. 519–537.

Obert, E. 2009 *Aerodynamic Design of Transport Aircraft*. Amsterdam, Germany: IOS Press.

Orr, W. M. 1907 The stability or instability of the steady motions of a perfect liquid and of a viscous liquid. *Proceedings of the Royal Irish Academy. A.* **27**, 9–68 and 69–138.

Peerhossaini, H., Bippes, H. & Steinbach, D. 1990 A model for the experimental study of curvature effects on transition of the boundary layer on a swept wing: preliminary results. *La Recherche aérospatiale* **6**, 15–21.

Pfenninger, W. 1965*a* Some results from the X-21A program. Part I. Flow phenomena at the leading edge of swept wings. In *Recent Developments in Boundary Layer Research*, *AGARDograph* 97, pt. IV, pp. 1–41.

Pfenninger, W. 1965*b* Some results from the textlnX-21A program. Part II. In *Recent Developments in Boundary Layer Research*, *AGARDograph* 97, pt. IV, pp. 1–41.

Pfenninger, W. 1987 Long-range LFC transport. In *Research in Natural Laminar Flow and Laminar-Flow Control, Part 1* (ed. J. N. Hefner & F. E. Sabo), *NASA Conference Publication* 2487, pp. 89–115.

Pfenninger, W., Reed, H. L. & Dagenhart, J. R. 1979 Design considerations of advanced supercritical low drag suction airfoils. In *Viscous Drag Reduction*, pp. 249–271. New York, N. Y.: AIAA.

Pointwise 2013 Mesh and grid generation software for CFD. www.pointwise.com/pw, accessed July 17, 2013.

Poll, D. I. A. 1979 Transition in the infinite swept attachment line boundary layer. *The Aeronautical Quarterly* **30**, 607–629.

Prandtl, L. 1946 On boundary layers in three-dimensional flow. *Ministry of Aircraft Production Reports and Translations* 64.

Pruett, C. D. 1994 A spectrally accurate boundary-layer code for infinite swept wings. *NASA Contractor Report* 195014.

Radeztsky, Jr., R. H., Reibert, M. S. & Saric, W. S. 1994 Development of stationary crossflow vortices on a swept wing. *AIAA Paper* 1994-2373.

Radeztsky, Jr., R. H., Reibert, M. S., Saric, W. S. & Takagi, S. 1993 Effect of micron-sized roughness on transition in swept-wing flows. *AIAA Paper* 1993-0076.

Rajnarayan, D. & Sturdza, P. 2011 Extensible rapid transition prediction for aircraft conceptual design. *AIAA Paper* 2011-3813.

Rams, D. 2013 Dieter Rams: ten principles for good design. vitsoe.com/us/about/good-design, accessed July 5, 2013.

Raymer, D. P. 2002 Enhancing aircraft conceptual design using multidisciplinary optimization. PhD thesis, Royal Institute of Technology, Stockholm, Sweden.

Redeker, G., Horstmann, K. H. & Köster, H. 1990 Design of a natural laminar flow glove for a transport aircraft. *AIAA Paper* 1990-3043.

Reed, H. L. 2008 Direct numerical simulation and transition: 2D flows. In *Advances in Laminar-Turbulent Transition Modelling*, *NATO Educational Notes* RTO-EN-AVT-151, pp. 5-1–5-36.

REED, H. L. & SARIC, W. S. 1989 Stability of three-dimensional boundary layers. *Annual Review of Fluid Mechanics* **21**, 235–284.

REED, H. L. & SARIC, W. S. 2011 Attachment-line heating in a compressible flow. *AIAA Paper* 2011-3242.

REED, H. L., SARIC, W. S. & ARNAL, D. 1996 Linear stability theory applied to boundary layers. *Annual Review of Fluid Mechanics* **28**, 389–428.

REIBERT, M. S., SARIC, W. S., CARRILLO, JR., R. B. & CHAPMAN, K. L. 1996 Experiments in nonlinear saturation of stationary crossflow vortices in a swept-wing boundary layer. *AIAA Paper* 1996-0184.

RENEAUX, J. & BLANCHARD, A. 1992 The design and testing of an airfoil with hybrid laminar flow control. In *First European Forum on Laminar Flow Technology*, *DGLR-Bericht* 92-06, pp. 164–174. Bonn, Germany: DGLR.

RHODES, R. G., REED, H. L., SARIC, W. S. & CARPENTER, A. L. 2010 Roughness receptivity in swept-wing boundary layers–computations. *International Journal of Engineering Systems Modelling and Simulation* **2** (1-2), 139–148.

RIZZETTA, D. P., VISBAL, M. R., REED, H. L. & SARIC, W. S. 2010 Direct numerical simulation of discrete roughness on a swept-wing leading edge. *AIAA Journal* **48** (11), 2660–2673.

ROACH, P. K. 2009 *Fundamentals of Verification and Validation*. Socorro, N. Mex.: Hermosa Publishers.

ROBERT, J. P. 1992 Hybrid laminar flow control—a challenge for a manufacturer. In *First European Forum on Laminar Flow Technology*, *DGLR-Bericht* 92-06, pp. 294–308. Bonn, Germany: DGLR.

ROBERTS, M. W. 2012 Computational evaluation of a transonic laminar-flow wing glove design. Master's thesis, Texas A&M University, College Station, Tex.

ROBERTS, M. W., REED, H. L. & SARIC, W. S. 2012 A transonic laminar-flow wing glove flight experiment: Computational evaluation and linear stability. *AIAA Paper* 2012-2668.

ROZENDAAL, R. A. 1986 Variable Sweep Transition Flight Experiment (VSTFE)—Parametric pressure distribution boundary layer stability study and wing glove design task. *NASA Contractor Report* 3992.

ROZENDAAL, R. A. 1987 Variable-Sweep Transition Flight Experiment (VSTFE): Stability code development and clean-up glove data analysis. In *Research in Natural Laminar Flow and Laminar-Flow Control, Part 3*, pp. 845–859. Hampton, Va.: NASA.

RUNYAN, L. J., BIELAK, G. W., BEHBEHANI, R., CHEN, A. W. & ROZENDAAL, R. A. 1990 757 NLF Glove Flight Test Results. In *Research in Natural Laminar Flow and Laminar-Flow Control, Part 3*, pp. 795–818. Hampton, Va.: NASA.

RYLE, JR., J. M. 1970 High Reynolds number subsonic aerodynamics. In *High Reynolds number subsonic aerodynamics*, *AGARD Lecture Series* AGARD-LS-37.

SACCO, G. & PIAGGIO, I. A. M. R. 1996 Piaggio P-180: Natural laminar flow test and in-service experience (invited). In *Abstracts of the Second European Forum on European Flow Technology*. Brussels, Belgium: Council of European Aerospace Societies.

SADIN, S. R., POVINELLI, F. P. & ROSEN, R. 1989 The NASA technology push towards future space mission systems. *Acta Astronautica* **20**, 73–77.

SAMANT, S. S., BUSSOLETTI, J. E., JOHNSON, F. T., BURKHART, R. H., EVERSON, B. L., MELVIN, R. G., YOUNG, D. P., ERICKSON, L. L., MADSON, M. D. & WOO, A. C. 1987 TRANAIR: a computer code for transonic analyses of arbitrary configurations. *AIAA Paper* 1987-34.

SARIC, W. S. 1994 Görtler vortices. *Annual Review of Fluid Mechanics* **26**, 379–409.

SARIC, W. S. 2008*a* Experiments in 3D boundary layers: stability and receptivity. In *Advances in Laminar-Turbulent Transition Modelling*, *NATO Educational Notes* RTO-EN-AVT-151, pp. 8-1–8-28.

SARIC, W. S. 2008*b* Introduction to linear stability. In *Advances in Laminar-Turbulent Transition Modelling*, *NATO Educational Notes* RTO-EN-AVT-151, pp. 2-1–2-56.

SARIC, W. S., CARPENTER, A. L. & REED, H. L. 2011 Passive control of transition in three-dimensional boundary layers, with emphasis on discrete roughness elements. *Philosophical Transactions of the Royal Society A* **369** (1940), 1352–1364.

SARIC, W. S., CARRILLO, JR, R. B. & REIBERT, M. S. 1998*a* Leading-edge roughness as a transition control mechanism. *AIAA Paper* 1998-0781.

SARIC, W. S., CARRILLO, JR, R. B. & REIBERT, M. S. 1998*b* Nonlinear stability and transition in 3D boundary layers. *Meccanica* **33** (5), 469–487.

SARIC, W. S. & REED, H. L. 2004 Toward Practical Laminar Flow Control-Remaining Challenges. *AIAA Paper* 2004-2311.

SARIC, W. S., REED, H. L. & KERSCHEN, E. J. 2002 Boundary-layer receptivity to free-stream disturbances. *Annual Review of Fluid Mechanics* **34**, 291–319.

SARIC, W. S., REED, H. L. & WHITE, E. B. 2003 Stability and transition of three-dimensional boundary layers. *Annual Review of Fluid Mechanics* **35**, 413–440.

SCHLICHTING, H. 1932 Über die Entstehung der Turbulenz in einem rotierenden Zylinder. *Nachrichten von der Gesellschaft der Wissenschaften zu Göttingen, Math. Phys. Klasse, Heft 2* pp. 160–198.

SCHLICHTING, H. 1933 Zur entstehung der Turbulenz bei der Plattenströmung. *Nachrichten von der Gesellschaft der Wissenschaften zu Göttingen, Math. Phys. Klasse* pp. 181–208.

SCHLICHTING, H. 1950*a* Amplitude distribution and energy balance of small disturbances in plate flow. *NACA Technical Memorandum* 1265.

SCHLICHTING, H. 1950*b* Turbulence and heat stratification. *NACA Technical Memorandum* 1262.

SCHRAUF, G. 2004 Large-scale laminar-flow tests evaluated with linear stability theory. *Journal of Aircraft* **41** (2), 224–230.

SCHRAUF, G., HERBERT, T. & STUCKERT, G. 1996 Evaluation of transition in flight tests using nonlinear parabolized stability equation analysis. *Journal of Aircraft* **33** (3), 554–560.

SCHUBAUER, G. B. & SKRAMSTAD, H. K. 1948 Laminar-boundary-layer oscillations and transition on a flat plate. *NACA Technical Memorandum* 909.

SILVER, N. 2012 *The Signal and the Noise*. New York, N. Y.: Penguin Press.

SMITH, A. M. O. & GAMBERONI, N. 1956 Transition, pressure gradient, and stability theory. *Douglas Aircraft Company Technical Report* ES-26388.

SOMMERFELD, A. 1908 Ein Beitrag zur hydrodynamischen Erklärung der turbulenten Flüssigkeitsbewegungen. In *Proceedings of the 4th International Congress of Mathematicians, Rome,* vol. III, pp. 116–124.

STURDZA, P. 2007 Extensive supersonic natural laminar flow on the Aerion business jet. *AIAA Paper* 2007-0685.

SZODRUCH, J. 1992 Welcome address. In *First European Forum on Laminar Flow Technology*, *DGLR-*

Bericht 92-06, pp. 2–3. Bonn, Germany: DGLR.

Tollmien, W. 1931 The production of turbulence. *NACA Technical Memorandum* 609.

Tollmien, W. 1936 General instability criterion of laminar velocity distributions. *NACA Technical Report* 792.

Tsien, H.-S. 1939 Two-dimensional subsonic flow of compressible fluids. *Journal of the Aeronautical Sciences* **6** (10), 399–407.

Tucker, A. A. 2012 Laminar flow control flight experiment design. PhD thesis, Texas A&M University, College Station, Tex.

Tufts, M. W., Reed, H. L. & Saric, W. S. 2013 Design of an infinite swept wing glove for an in-flight dre experiment. *AIAA Paper* 2013-2411.

Van Ingen, J. L. 1956 A suggested semi-empirical method for the calculation of the boundary layer transition region. *University of Delft Technical Report* VTH-74.

Vassberg, J. C., Tinoco, E. N., Mani, M., Rider, B., Zickuhr, T., Levy, D. W., Brodersen, O. P., Eisfeld, B., Crippa, S., Wahls, R. A., Morrison, J. H., Mavriplis, D. J. & Murayama, M. 2010 Summary of the fourth AIAA CFD drag prediction workshop. *AIAA Paper* 2010-4547.

von Kármán, T. 1941 Compressibility effects in aerodynamics. *Journal of the Aeronautical Sciences* **8** (9), 337–356.

Voogt, N. 1993 European Laminar Flow Investigation (ELFIN). Presented to the Netherlands Association of Aeronautical Engineers, Amsterdam.

Voogt, N. 1996 Flight testing of a Fokker 100 test aircraft with laminar flow glove (invited). In *Abstracts of the Second European Forum on European Flow Technology*, pp. 2.3–2.14. Brussels, Belgium: Council of European Aerospace Societies.

Wagner, R. D., Maddalon, D. V., Bartlett, D. W. & Collier, Jr, F. S. 1988 Fifty years of laminar flow flight testing. *SAE Paper* 881393.

Wagner, R. D., Maddalon, D. V. & Fisher, D. F. 1990 Laminar flow control leading-edge systems in simulated airline service. *Journal of Aircraft* **27** (3), 234–244.

Walatka, P. P., Buning, P. G., Pierce, L. & Elson, P. A. 1990 PLOT3D user's manual. *NASA Technical Memorandum* 101067.

White, E. B. & Saric, W. S. 2005 Secondary instability of crossflow vortices. *Journal of Fluid Mechanics* **525**, 275–308.

White, F. M. 2006 *Viscous Fluid Flow*, 3rd edn. New York, N. Y.: McGraw-Hill.

Williams, T. C. 2012 Design of an instrumentation for a boundary layer transition wing glove experiment. Master's thesis, Texas A&M University, College Station, Tex.

Wolfram Research 2013 Wolfram Mathematica: technical computing software. www.wolfram.com/mathematica, accessed July 27, 2013.

Young, D. P. 2011 Note on parametrization of airfoils. *AIAA Journal* **49** (1).

Young, D. P., Huffman, W. P., Melvin, R. G., Hilmes, C. L. & Johnson, F. T. 2003 Nonlinear elimination in aerodynamic analysis and design optimization. In *Large-Scale PDE-Constrained Optimization* (ed. L. T. Biegler, M. Heinkenschloss, O. Ghattas & B. Bart van Bloemen Waanders), *Lecture Notes in Computational Science and Engineering*, vol. 30, pp. 17–43. Berlin, Germany: Springer-Verlag.

APPENDIX A

ERA DRELFGE OBJECTIVES AND REQUIREMENTS

Objective no.	Objective	Measure of performance
ERA.DRE.001P	Demonstrate the aerodynamic validity of DRE technology for swept-wing laminar flow control beyond the limits of Natural Laminar Flow at operationally relevant and repeatable conditions for transport aircraft.	Success is evaluated through data obtained to verify the flight conditions, glove pressure distribution, and boundary layer transition location.
ERA.DRE.002P	Demonstrate the capability of DRE technology to repeatedly overcome quantified small-amplitude distributed surface roughness for extended control of cross-flow instability at roughness Reynolds numbers typical of transport aircraft.	Data including, but not limited to surface roughness measurements near the attachment line, flight conditions, glove pressure distribution, and boundary layer transition location will be used to assess this capability.
ERA.DRE.003S	Obtain repeatable and sustainable high-quality, flight-research data suitable for evaluating the physical processes associated with the Tollmien-Schlichting and crossflow transition mechanisms for verification and improvement of design and analysis tools.	The instrumentation suite will include the required instrumentation to satisfy goals 1 and 2 and should include additional capability to identify time-dependent and/or transient boundary layer events at high temporal and spatial fidelity through a wide range of flight conditions and glove aerodynamic loading levels.
ERA.DRE.004S	Demonstrate pressure side laminar flow simultaneously with suction side laminar flow.	Success is evaluated through data, including but not limited to, flight condition information, glove pressure distribution, and boundary layer transition location on the pressure surface.

TABLE A.1. ERA DRELFGE objectives. "P" indicates a primary ojbective, while "S" indicates secondary.

Requirement no.	Requirement	Parent objective	Verification method	Planned satisfaction method, feature, or item
ERA.DRE.ExR.001	NLF shall be demonstrated at $Re_c \geq 15$ million with $(x/c)_{tr} \geq 0.60$ on the suction side over 14 inches of span.	ERA.DRE.001P ERA.DRE.002P ERA.DRE.003S ERA.DRE.004S	analysis, test	The DRELFGE has been designed to meet this requirement, and that will be shown through a boundary layer stability analysis. Flights of the DRELFGE on the SCRAT will test this requirement.
ERA.DRE.ExR.002	DRE shall extend laminar flow at $Re_c \geq 22$ million on the suction surface by at least 50%.	ERA.DRE.001P ERA.DRE.002P ERA.DRE.003S ERA.DRE.004S	analysis, test	The DRELFGE has been designed to accommodate DREs, and this will be shown through analysis. Flights of the DRELFGE on the SCRAT will test this requirement.
ERA.DRE.ExR.003	The DRE LFGE shall be demonstrated at a Reynolds number no less than 1.4 million/ft.	ERA.DRE.001P ERA.DRE.002P ERA.DRE.003S ERA.DRE.004S	test	The DRELFGE has been designed for a Reynolds number of 1.5 million/ft. Flights of the DRELFGE will test that this requirement will be met.
ERA.DRE.ExR.004	NLF and DRE application shall be demonstrated at leading edge sweeps of $\Lambda_{LE} \geq 30°$.	ERA.DRE.001P ERA.DRE.002P ERA.DRE.003S ERA.DRE.004S	inspection, test	The DRELFGE has been designed with a leading edge sweep angle of $34.6°$. The DRELFGE planform will be inspected to ensure this requirement has been met. Flights of the DRELFGE on the SCRAT will test this requirement.

Table A.2. ERA DRELFGE derived experimental requirements (page 1 of 3).

Requirement no.	Requirement	Parent objective	Verification method	Planned satisfaction method, feature, or item
ERA.DRE.ExR.005	Transport relevant section loading, shall be designed to a $C_\ell = 0.5$ referenced to the local glove chord within the laminar-flow span.	ERA.DRE.001P ERA.DRE.002P ERA.DRE.003S ERA.DRE.004S	inspection, test	The DRELFGE has been designed to a $C_\ell = 0.5$ referenced to the local glove chord within the laminar-flow span. Flights of the DRELFGE on the SCRAT will test this requirement.
ERA.DRE.ExR.006	Transport relevant section loading shall be designed to a Mach of no less than $M = 0.72$.	ERA.DRE.001P ERA.DRE.002P ERA.DRE.003S ERA.DRE.004S	test	Mach 0.75 has been used as the design point for the DRELFGE. Flights of the DRELFGE on the SCRAT will test this requirement.
ERA.DRE.ExR.007	Repeatable data shall be obtained at a repeatable and stabilized flight condition (i.e. altitude, Mach, etc).	ERA.DRE.001P ERA.DRE.002P ERA.DRE.003S ERA.DRE.004S	analysis, test	The DRELFGE has been designed to demonstrate NLF at aircraft angles of attack that are at or near the SCRAT's trim point. Flights of the DRELFGE on the SCRAT will test this requirement.
ERA.DRE.ExR.008	Passive DRE appliqué shall be used.	ERA.DRE.001P ERA.DRE.002P ERA.DRE.003S ERA.DRE.004S	inspection	The DRELFGE has been designed for passive DRE applique.

TABLE A.2. ERA DRELFGE derived experimental requirements (page 2 of 3).

Requirement no.	Requirement	Parent objective	Verification method	Planned satisfaction method, feature, or item
ERA.DRE.ExR.009	Glove design shall include the capability to vary leading edge surface roughness from approximately 0.3 μm RMS to 4 μm RMS.	ERA.DRE.001P ERA.DRE.002P ERA.DRE.003S ERA.DRE.004S	inspection, test	The DRELFGE has been designed with re-movable leading edges which will facilitate this requirement. The DRELFGE leading edges can be painted and roughened to meet this requirement. Flights of the DRELFGE on the SCRAT will test this requirement.
ERA.DRE.ExR.0010	Simultaneous pressure side and suction side laminar flow should be demonstrated at the flight conditions prescribed by ERA.DRE.ExR.001.	ERA.DRE.004S	analysis, test	The DRELFGE has been designed for NLF on the pressure and suction sides, and this will be shown through analysis. Flights of the DRELFGE on the SCRAT will test this requirement.

TABLE A.2. ERA DRELFGE derived experimental requirements (page 3 of 3).

APPENDIX B

INVSICID GRID INDEPENDENCE

A grid independence study substantiates the arguments regarding the differences observed between linear-vorticity panel XFOIL (Drela 1989) and compressible Euler FLUENT (ANSYS, Inc. 2010) computations for 2D, invsicid airfoils as described in §III.3.1. This verification study comprises three comparisons using results on XFOIL and FLUENT grids:

1. Incompressible governing equations
2. Compressible governing equations
3. Airfoil thickness effects

The objective of this study is to first verify that both the FLUENT and XFOIL grids are sufficiently converged to allow qualitative C_p comparisons to be made between them. The second objective is to verify that the LST results on the FLUENT mesh are sufficiently resolved for qualitative use in design. The test of mission success are the lofted glove results as computationally evaluated by Roberts *et al.* (2012); hence the level of convergence for a typical design iteration is relaxed somewhat to emphasize computational speed over strict correctness.

B.1. Grid parameters

A total of eight FLUENT grids and three XFOIL grids are evaluated in this study. Table B.1 summarizes the key grid parameters as referenced to the C-mesh topology in figure B.1. The airfoil for the study is TAMU2D-003T-075 (table II.3).

In XFOIL version 6.97, grid N160 is the default paneling, N354 the maximum number of panels allowed by the code, and N354b the maximum number of panels with additional refinement in the LE and TE regions.

The baseline structured FLUENT grid, G0, is the grid used for analysis purposes throughout this dissertation. Grids G1–G4 consider the effects of extending the farfield, up to at least 100 chord lengths as recommended by Vassberg, Tinoco, Mani, Rider, Zickuhr, Levy, Brodersen, Eisfeld, Crippa, Wahls, Morrison, Mavriplis & Murayama (2010). The scaling factor for each farfield expansion is 1.5. The first cell height is less than the recommended values for boundary-layer computations in Vassberg *et al.* (2010), which should be superfluous since there is no boundary layer in an Euler computation. Grids G4-G7 consider mesh refinement with uniform refinement of factor of 1.4. Hyperbolic tangent spacing is used for all connectors with the specified initial spacings at the key locations in the mesh. *n* refers to the number of nodes on a given connector (or total nodes in the domain n_{total}) and *Δ* refers

to a connector end spacing constraint (indicated by arrows in the topology figure). The grids in this section were generated in Pointwise version 17.1R3 (Pointwise 2013) while FLUENT computations were computed using version 13.0.0. Solutions are carried out in 2D and the C_p corrected to 3D according to the procedure in §III.2.1.

FLUENT grids

ID	X_0	X_1	X_2	Y_0	n_{af}	n_y	n_{wake}	n_{total}	Δx_0	Δx_1	Δx_2	Δy_0	Δy_1
G0	-25.0	40.0	9.3	40.0	125	100	120	48 580	0.00010	0.0010	0.20	0.50	0.10
G1	-37.5	60.0	14.0	60.0	125	100	120	48 580	0.00010	0.0010	0.20	0.50	0.10
G2	-56.3	90.0	20.9	90.0	125	100	120	48 580	0.00010	0.0010	0.20	0.50	0.10
G3	-84.4	135.0	31.4	135.0	125	100	120	48 580	0.00010	0.0010	0.20	0.50	0.10
G4	-126.6	202.5	47.0	202.5	125	100	120	48 580	0.00010	0.0010	0.20	0.50	0.10
G5	-126.6	202.5	47.0	202.5	175	140	168	95 452	0.00007	0.0007	0.14	0.36	0.07
G6	-126.6	202.5	47.0	202.5	245	235	196	187 337	0.00005	0.0005	0.10	0.26	0.05
G7	-126.6	202.5	47.0	202.5	343	329	274	367 105	0.00004	0.0004	0.07	0.18	0.04

XFOIL grids

ID	Number of panels	TE/LE panel density ratio
N160	160	0.150
N354	354	0.150
N354b	354	0.500

TABLE B.1. Grid specifications for FLUENT and XFOIL grid independence studies. The FLUENT parameters are referenced to the topology in figure B.1

B.2. Incompressible governing equations

Figure B.2 shows the C_p distributions for the incompressible case ($M = 0.001$, $AoA = 0°$, $H = 40\,000$ ft in FLUENT). The solution is computed using double precision, node- and pressure-based solver, coupled pressure–velocity equations, second-order pressure discretization and second-order upwind momentum discretization. A velocity inlet boundary condition is imposed at the conic upstream boundaries and a gauge pressure outlet at the vertical downstream boundaries. Residuals in all cases converge smoothly to at least 10^{-10}. No oscillation is observed in C_ℓ, C_d, or moment coefficient and each converge to a single value.

As expected, the agreement between XFOIL and FLUENT is good. The solution is relatively insensitive to refinement in either flow solver. An exception is near the trailing edge in XFOIL, where N354b agrees best with the trailing edge behavior in FLUENT, especially on the pressure side of the airfoil.
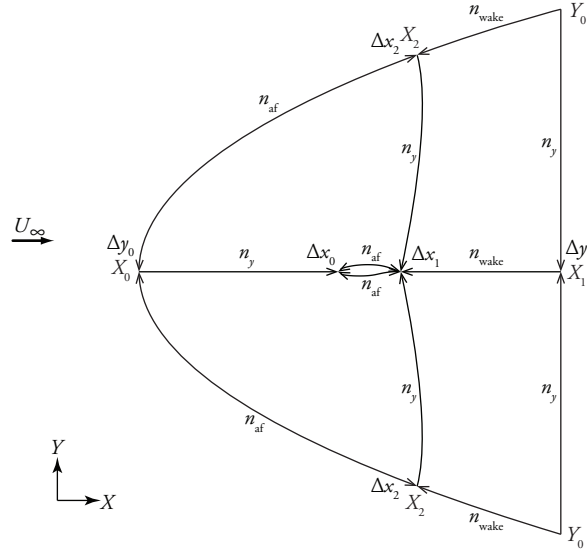
FIGURE B.1. FLUENT invscid mesh topology. Not to scale. Origin is at airfoil leading edge.
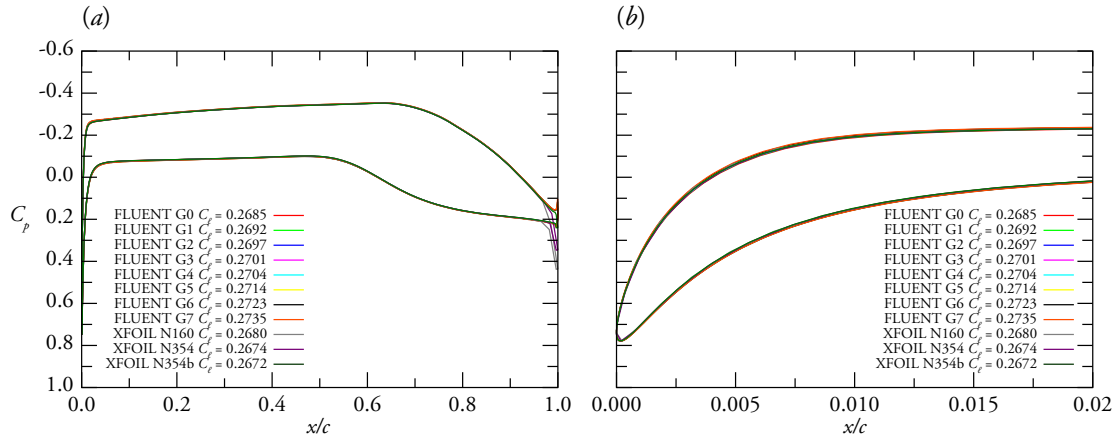
FIGURE B.2. Incompressible grid independence C_p distributions on TAMU2D-003T-075.

B.3. Compressible governing equations

Double-precision 2D FLUENT is configured using the node- and pressure-based solver with compressible ideal gas air, coupled pressure-velocity equations, second-order pressure discretization and second-order upwind density, momentum, and energy equations. All boundary connectors are specified as pressure far field. The conditions correspond to the primary design point for this airfoil: $M = 0.75$, $AoA = 0°$, $H = 40\,000$ ft.

Residuals on all grids converge smoothly to at least 10^{-10} and C_ℓ, C_d, or moment coefficient each

converge to a single value without oscillation. WINGBL2 is used to generate the boundary-layer profiles for LST computations in LASTRAC as described in §III.3.

Graphically (figure B.3), the compressible case shows relatively minor integral variations as the grid is refined. Convergence in FLUENT or XFOIL does not account for the differences in the suction-side C_p observed between the two solvers, which was attributed to limitations of the Kármán-Tsien correction in §III.3.1.
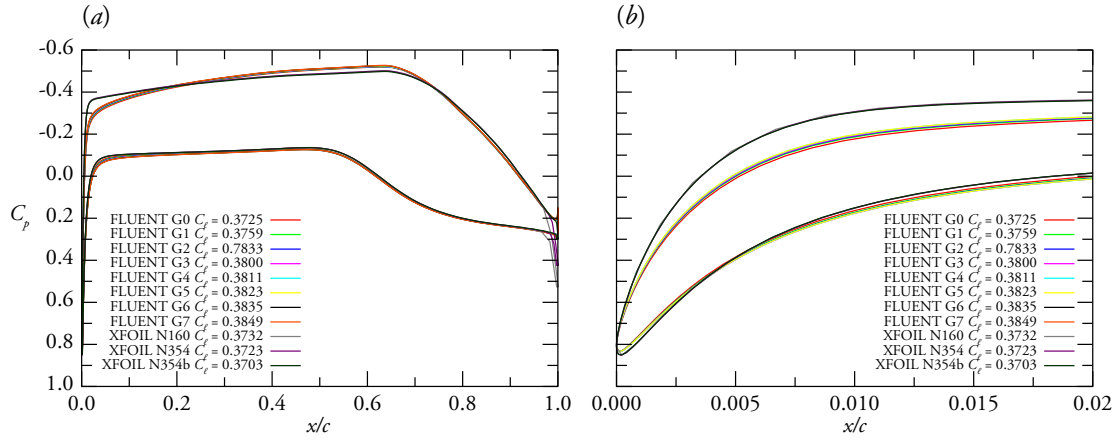
FIGURE B.3. Compressible grid independence C_p distributions on TAMU2D-003T-075.

The N-factors in figures B.4 and B.5 show the sensitivity of the LST stability to apparently minor changes in C_p. Grid G7 appears to be approaching convergence and predicts transition 16% further aft than in grid G0. If these results were being used for mission success, further grid convergence effort might be warranted; here the primary purpose of the LST results at this stage is qualitative to determine sensitivities for OML changes before lofting into a 3D glove. Design iteration speed is a driving factor in choosing the appropriate level of refinement. Grid G7 takes approximately 30 minutes to converge compared to 5 minutes for grid G4. Although the specific transition location for $N = 7$ changes significantly as the grid is refined, the qualitative behavior is unchanged. Thus, G7 is probably excessive refinement for this stage of the study. G5 or G6 is perhaps an ideal balance for buttline design purposes.

B.4. Airfoil thickness effects

Since the Kármán-Tsien correction is predicated on small perturbations about $C_p \approx 0$ for elliptical, non-lifting airfoils (Tsien 1939; von Kármán 1941), the agreement between FLUENT and XFOIL should be expected to improve as the airfoil is progressively thinned. To evaluate this property of the approximation, the airfoil is halved successively in thickness and the results computed on grid G5 and
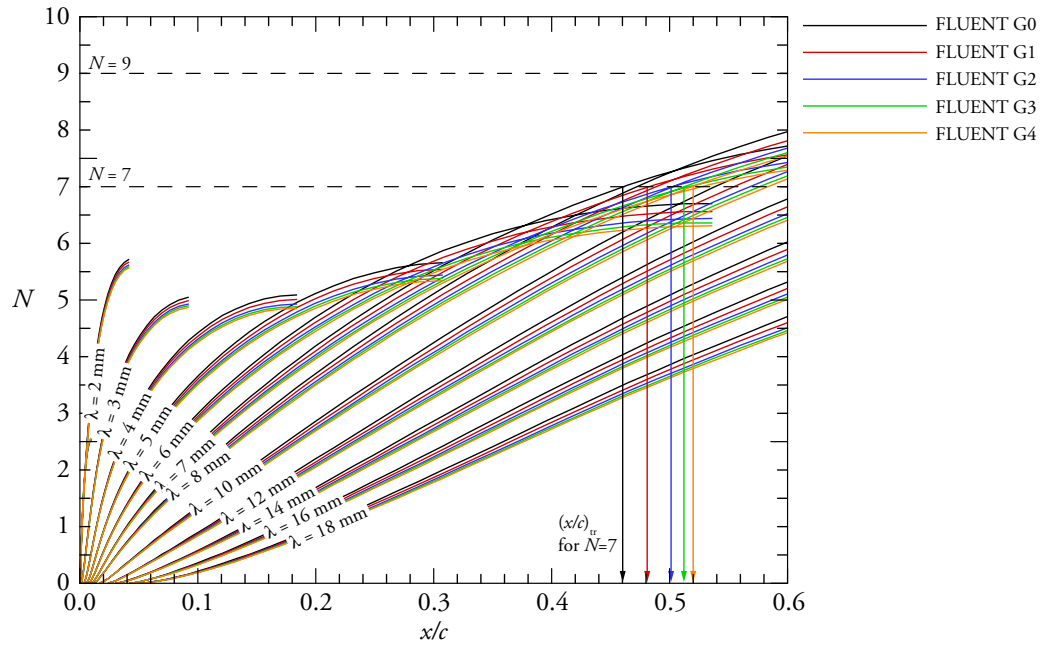
FIGURE B.4. *N*-factors for FLUENT farfield independence grids G0–G4.
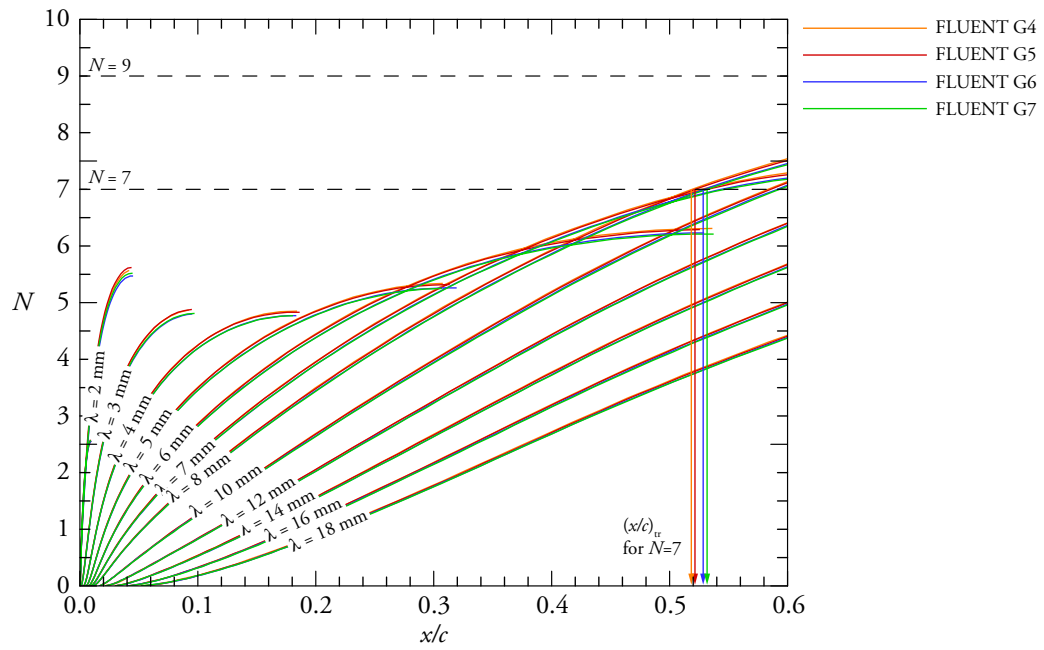
FIGURE B.5. *N*-factors for FLUENT refinement convergence grids G4–G7.

N354b at the same conditions as the compressible case in the previous section.

Figure B.6 shows that this is indeed the case, apart from the suction peak near the leading edge. Since the attachment line is inherently near $C_p = 1$, conceivably the Kármán-Tsien approximation will never approach a compressible Euler solution near the leading edge, which propagates to produce differences in the rest of the C_p over the airfoil.
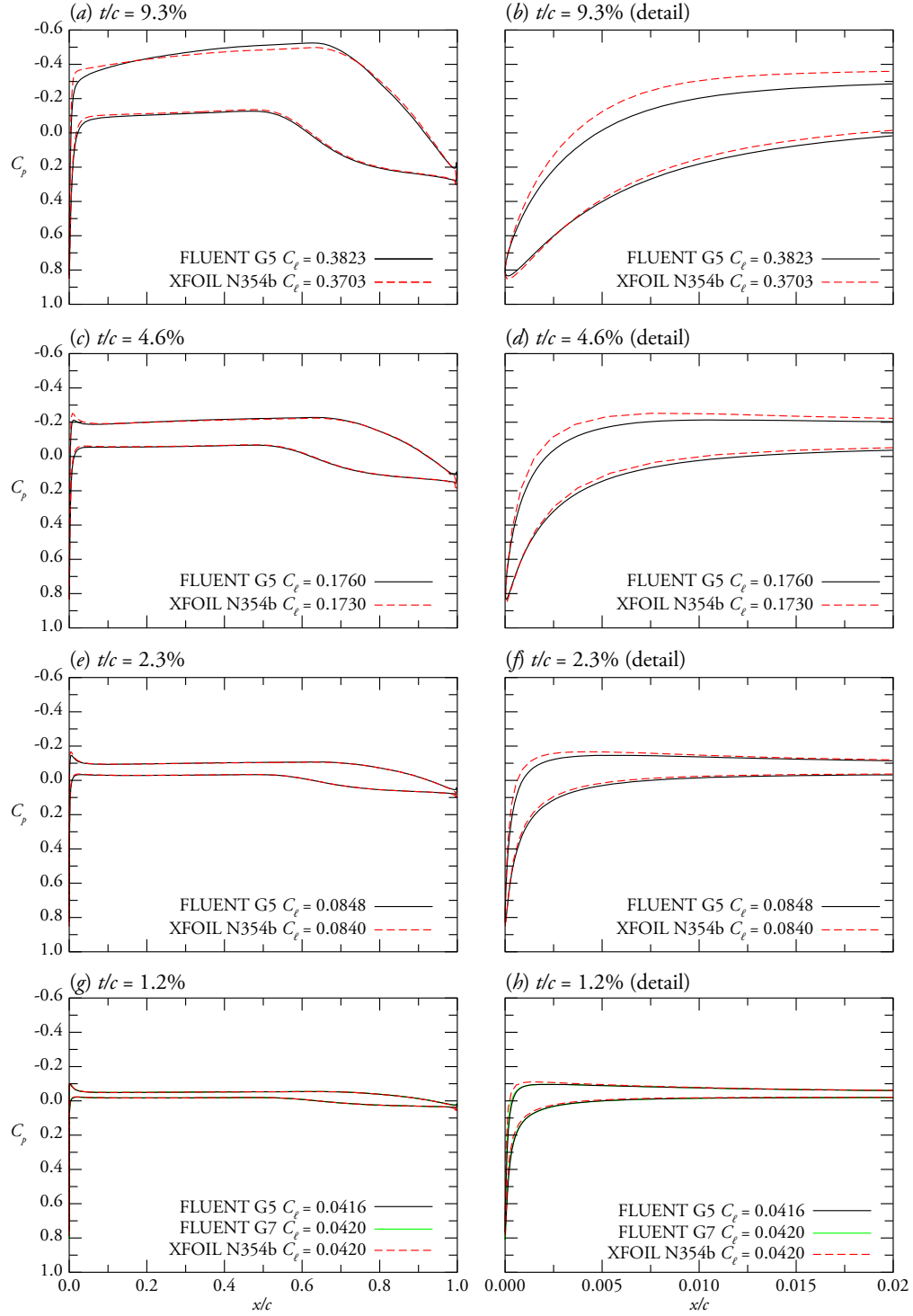
FIGURE B.6. XFOIL and FLUENT results for TAMU2D-003T-075 sections scaled to various thicknesses.

APPENDIX C

SCRIPT AND PROGRAM SOURCE FILES

C.1. x2w.py: Outer solution to boundary-layer solver input

C.1.1. *x2w.py*

```python
#!/usr/bin/env python

# x2w: takes the pressure coefficient from a outer solution and converts it into
#      the input for wingbl2.

import warnings
warnings.filterwarnings("ignore", category=DeprecationWarning)

import sys
import os
import re
import shutil
from subprocess import call
from atmosphere import atmosphere
from numpy import *
from scipy import integrate , interpolate
from math import cos,sin,pi
from optparse import OptionParser
from operator import itemgetter
from sys import exit

p0   = 2116.22807
t0   = 518.67
rho0 = 0.0023772
srcdir=os.path.expanduser('~/src/xwlkit')

def error(message):
    sys.stderr.write("error: "+message+"!\n")
    exit(1)
def warning(message):
    sys.stderr.write(" warn: "+message+"\n")

def calcRecAlt(altitude,chord,fs):
    M = fs["Mach number"]
    gamma = fs["gamma"]
    sc1 = fs["sc1"]
    sc2 = fs["sc2"]
    rgas = fs["rgas"]
    sigma,delta,theta = atmosphere(altitude*3.048e-4)
```

```python
        pressure = delta * p0
        temperature = theta * t0
        density = sigma * rho0
        mu = sc1 * temperature*sqrt(temperature) / (temperature + sc2)
        Uinf = M * sqrt( gamma * rgas * temperature )
        rec = density * Uinf * chord / mu
        return(rec)

def calcRecPT(chord,fs):
        M = fs["Mach number"]
        gamma = fs["gamma"]
        sc1 = fs["sc1"]
        sc2 = fs["sc2"]
        rgas = fs["rgas"]
        pressure = fs["pressure"]
        temperature = fs["temperature"]
        density = pressure / ( rgas * temperature )
        mu = sc1 * temperature*sqrt(temperature) / (temperature + sc2)
        Uinf = M * sqrt( gamma * rgas * temperature )
        rec = density * Uinf * chord / mu
        return(rec)

#parse arguments
command=sys.argv[0]
command=command.split('/')[-1]
usage = "usage: %s [options] [CASENAME] [CONDITIONFILE] [DATAFILE]"%command
parser = OptionParser(usage=usage)

parser.add_option("-b", "--buttline", dest="buttline",
                    help="specify buttline location: (_none_)",
                default=None)

parser.add_option("-c", "--correct", action="store_true" , dest="correct",
                    help="apply karman-tsien compressiblity correction to cp",
                default=False)

parser.add_option("-f", "--fudge", dest="fudge",action="store_true",
                help="fudge stagnation point cp",
                default=False)

parser.add_option("-n", "--normal", dest="normal",action="store_true",
                help="correct 2D cp for sweep",
                default=False)

parser.add_option("-p", "--program", dest="program",
                help="input file format: (fluent2|fluent3|tranair2|_tranair3_|xfoil)",
                default="tranair3")

parser.add_option("-s", "--side", dest="side",
                    help="airfoil pressure or suction side: (_suction_|pressure)",
                default="default")
```

```python
parser.add_option("-d", "--dimensions", dest="dimensions",
          help="input dimensions: (_non_|m|cm|in)",
          default="non")

parser.add_option("-i", "--input", dest="input",
              help="source for certain input conditions (_path_|none)",
          default="path")

parser.add_option("-m","--mirror", dest="mirror",
              help="mirror axes (_none_|x|y|xy)",
              default="none")

parser.add_option("-x","--xstride", dest="xstride",
              help="x index stride (_1_)",
              default="1")

(options,args) = parser.parse_args()

# make sure side has a valid value
side=options.side.lower()
if side!="suction" and side!="pressure" and side!="default":
    error('airfoil side must be pressure or suction')

if (options.buttline):
    buttline = float(options.buttline)
else:
    buttline = options.buttline
fudge = options.fudge
correct = options.correct
normal = options.normal
program = options.program
if program!="fluent2" and program!="xfoil" and program!="tranair2" \
and program!="tranair3" and program!="fluent3" and program !="fun3":
    error('input format must be fluent[23], tranair[23], fun3d, or xfoil')

dimensions = options.dimensions
if dimensions!="non":
    if (program!="tranair3" and program!="fluent3" and program!="fun3"):
        dimensions = "non"
        warning('dimensional input only supported for fluent3, tranair3, and fun3')
        warning('using non-dimensional instead')
    elif(dimensions!="m" and dimensions!="cm" and dimensions!="in"):
        error('dimensions must be non, m, cm, or in')

inSrc = options.input

mirror = options.mirror

xstride = int(options.xstride)
```

```python
if len(args)==0:
    parser.print_usage()
    exit(1)
elif len(args)==1:
    fsfname="fs.txt"
    if (program=="fluent2" or program=="tranair"):
        casename=args[0]
        datafname="data.csv"
    elif (program=="xfoil"):
        casename=args[0]
        xyfname="xy.txt"
        cpfname="cp.txt"
elif (len(args)<4
and not program=="fluent2"
and not program=="tranair2"
and not program=="tranair3"
and not program=="fluent3"
and not program=="fun3") or (len(args)<3):
    parser.print_usage()
    exit(1)
else:
    if (program=="fluent2" or program=="tranair2" or program=="tranair3"
            or program=="fluent3"
            or program=="fun3" ):
        casename=args[0]
        fsfname=args[1]
        datafname=args[2]
    elif (program=="xfoil"):
        casename=args[0]
        fsfname=args[1]
        xyfname=args[2]
        cpfname=args[3]
xytitle = casename

if(casename=="suction"):
    side="suction"
elif(casename=="pressure"):
    side="pressure"
elif(side=="default"):
    side="suction"

#make working directory
casedir="./"+casename+"/"
if os.path.isdir(casedir):
    shutil.rmtree(casedir)
#    error("case "+casename+" already exists")
#else:
os.mkdir(casedir)

# regular expressions
reFloat = re.compile('[+-]?\d*\.?\d+[Ee]?[+-]?\d*')
```

114

```
reBlank = re.compile('^ *$')

# process freestream file
f=open(fsfname)
lineno=0

fs = {}
for line in f:
    lineno+=1
    if reBlank.match(line):
        continue
    (num,param) = line.split("/")
    if not num or not param:
        error("problem with "+xyfname+\
          " format on line %d"%lineno)
    param = param.replace('reference','').strip()
    fs[param] = float(num)
    if param == "chord length in in":
        chord = fs["chord length in in"]/12.
    if param == "chord length in ft":
        chord = fs["chord length in ft"]
f.close()

sweepd = fs["sweep angle in degrees"]
sweep = sweepd * pi/180
mach = fs["Mach number"]
gamma = fs["gamma"]

# check for complete state specification
if "altitude in ft" in fs:
    lastspec="altitude"
elif "chord Reynolds number" in fs and "temperature" in fs:
    lastspec="recT"
elif "temperature" in fs and "pressure" in fs:
    lastspec="pT"
elif "chord Reynolds number" in fs:
    lastspec="findAlt"
else:
    error("need a complete state specification (p+T|altitude|rec+T|rec)")

# process xy file
x = array([])
y = array([])
cpx = array([])
cpy = array([])
cpp = array([])

if(program=="xfoil"):
    # get title or read in first xy data
    f=open(xyfname,'r')
    lineno=0
```

```
        line=f.readline().strip()

        if len(reFloat.findall(line))<2:
            xytitle=line
        else:
            nums  = reFloat.findall(line.strip())
            if len(line)<2:
                error("problem with "+xyfname+" format on line %d"%lineno)
            x=append(x,float(nums[0]))
            y=append(y,float(nums[1]))

        # read in xy data
        for line in f:
            lineno+=1
            nums  = reFloat.findall(line.strip())
            if len(nums)<2:
                continue
            x=append(x,float(nums[0]))
            y=append(y,float(nums[1]))
        f.close()

    # process cp data
        f = open(cpfname)
        for line in f:
            nums  = reFloat.findall(line.strip())
            if len(nums)<2:
                continue
            cpx=append(cpx,float(nums[0]))
            cpy=append(cpy,float(nums[0]))
            cpp=append(cpp,float(nums[1]))
        f.close()
elif(program=="fluent2"):
    f=open(datafname,'r')
    for line in f:
        nums = reFloat.findall(line.strip())
        if len(nums)<3:
            continue
        x=append(x,float(nums[1]))
        cpx=append(cpx,float(nums[1]))
        cpy=append(cpy,float(nums[0]))
        y=append(y,float(nums[2]))
        cpp=append(cpp,float(nums[3]))
    f.close()
elif(program=="tranair2"):
    f=open(datafname,'r')
    f.readline()
    for line in f:
        nums = reFloat.findall(line.strip())
        if re.match("\*EOF",line):
            break
        elif len(nums)<3:
```

```python
                continue
        x=append(x,float(nums[0]))
        cpx=append(cpx,float(nums[0]))
        cpy=append(cpy,float(nums[0]))
        y=append(y,float(nums[1]))
        cpp=append(cpp,float(nums[3]))
    f.close()
elif(program=="tranair3"):
    call("awk"+" -f"+srcdir+"/ggp2xycp.awk "+datafname+">ggpdata.dat",
        shell=True)
    datafname="ggpdata.dat"
    cpindex = 4
    xindex = 0
    yindex = 2
    blindex = 1
    f=open(datafname,'r')
    foundbl = False
    for line in f:
        nums = reFloat.findall(line.strip())
        if len(nums)<3:
            if(foundbl):
                break
            else:
                continue
        if( not foundbl and  float(nums[blindex]) - 0.1 < buttline
                and float(nums[blindex]) + 0.1 > buttline ):
            foundbl=True
        if(foundbl):
            x=append(x,float(nums[xindex]))
            cpx=append(cpx,float(nums[xindex]))
            cpy=append(cpy,float(nums[0]))
            y=append(y,float(nums[yindex]))
            cpp=append(cpp,float(nums[cpindex]))
    f.close()
elif(program=="fluent3"):
    cpindex = 2
        if (dimensions=="non"):
                xindex = 0
                yindex = 1
        elif (dimensions=="m"):
                xindex = 0
                yindex = 1
    f=open(datafname,'r')
    for line in f:
        nums = reFloat.findall(line.strip())
        #if len(nums)<3:
            #continue
        x=append(x,float(nums[xindex]))
        cpx=append(cpx,float(nums[xindex]))
        cpy=append(cpy,float(nums[yindex]))
        y=append(y,float(nums[yindex]))
```

```
            cpp=append(cpp,float(nums[cpindex]))
        f.close()
elif(program=="fun3"):
        cpindex = 3
        xindex = 0
        yindex = 2
        f=open(datafname,'r')
        for line in f:
                if line.strip()[0].isalpha():
                        continue
                nums = reFloat.findall(line.strip())
                if len(nums)<3:
                        continue
                x=append(x,float(nums[xindex]))
                cpx=append(cpx,float(nums[xindex]))
                cpy=append(cpy,float(nums[yindex]))
                y=append(y,float(nums[yindex]))
                cpp=append(cpp,float(nums[cpindex]))
        f.close()

# write out unmodified xy points if dimensional
if(dimensions!="non"):
    f = open("xy-"+dimensions+".dat","w")
    for i in range(0,len(x)):
        if(buttline):
            f.write("%18.10e %18.10e %18.10e\n"%(x[i],y[i],
                    buttline))
        else:
            f.write("%18.10e %18.10e %18.10e\n"%(x[i],y[i],
                    buttline))
    f.close()

# mirror axes to get orientation correct if desired
if(mirror=="x" or mirror=="xy"):
    x = -x
    cpx = -cpx
if(mirror=="y" or mirror=="xy"):
    y = -y
    cpy = -cpy

# determine if xy data is ordered counterclockwise from te to le to start
# this assumes that the data is in some unidirectional order
iTE = x.argmax()
if(iTE != 1 or iTE != len(x)):
    x = append(x[iTE:],x[:iTE])
    y = append(y[iTE:],y[:iTE])
    cpx = append(cpx[iTE:],cpx[:iTE])
    cpy = append(cpy[iTE:],cpy[:iTE])
    cpp = append(cpp[iTE:],cpp[:iTE])

# check for duplicated points
```

```
i=1
while i < len(x):
    if (x[i]-x[i-1])==0.0 and (y[i]-y[i-1])==0.0:
        x=delete(x,i)
        y=delete(y,i)
        cpx=delete(cpx,i)
        cpy=delete(cpy,i)
        cpp=delete(cpp,i)
    else:
        i+=1

# drop some values if desired
if(xstride>0):
        x = x[::xstride]
        y = y[::xstride]
    cpx = cpx[::xstride]
    cpy = cpy[::xstride]
    cpp = cpp[::xstride]


# make sure the TE is at the start and the end
if x[0] != x[-1] or y[0] != y[-1]:
    x=append(x,x[0])
    y=append(y,y[0])
    cpx=append(cpx,cpx[0])
    cpy=append(cpy,cpy[0])
    cpp=append(cpp,cpp[0])

iComp = 30
xyccw = bool(y[iComp]<y[-iComp])
if not xyccw:
        x = x[::-1]
        y = y[::-1]
    cpx = cpx[::-1]
    cpy = cpy[::-1]
    cpp = cpp[::-1]

# find leading edge index and make sure it's at zero
iLEx = x[30:-30].argmin()+30
if (x[iLEx] != 0.):
    x = x - x[iLEx]
iLE = cpx[30:-30].argmin()+30
if (cpx[iLE] != 0.):
    cpx = cpx - cpx[iLE]

# need cp at exact same x locations
if len(cpx)!=len(x) or not (cpx==x).all():
    # unwrap coordinates
    for i in range(0,iLEx):
        x[i] = -x[i]
    for i in range(0,iLE):
```

```
        cpx[i] = -cpx[i]
    warning("interpolating xy coordinates to match cp locations")
    tck = interpolate.splrep(x,y,s=0,k=1)
    cpy = y = interpolate.splev(cpx,tck,der=0)
    x = copy(cpx)
        for i in range(0,iLE):
                x[i] = -x[i]
                cpx[i] = -cpx[i]
#    warning("interpolating cp coordinates to match x locations")
#        f = interpolate.interp1d(cpx,cpp)
#        cpx = copy(x)
#        cpy = copy(y)
#        cpp = f(x)
#    for i in range(0,iLEx):
#        x[i] = -x[i]
#                cpx[i] = -cpx[i]

# determine if xy data is ordered properly for the side under consideration
iComp = 30
xycw = bool(y[iComp]<y[-iComp])
if ( side=="suction" and not xycw) or ( side=="pressure" and xycw):
        x = x[::-1]
        y = y[::-1]
    cpx = cpx[::-1]
    cpy = cpy[::-1]
    cpp = cpp[::-1]
if (side=="pressure"):
        y = -y
    cpy = -cpy

# change dimensions of x and y to feet if dimensional
if(dimensions=="cm"):
    cm2ft = 0.0328083989501312
    x = x*cm2ft
    cpx = cpx*cm2ft
    cpy = cpy*cm2ft
    y = y*cm2ft
if(dimensions=="m"):
    m2ft = 3.28083989501312
        x = x*m2ft
        cpx = cpx*m2ft
        cpy = cpy*m2ft
        y = y*m2ft
if(dimensions=="in"):
    x = x/12.
    y = y/12.
    cpx = cpx/12.
    cpy = cpy/12.

# derotate coordinates if needed
while (abs(x[iLE]) !=0. or abs(y[iLE]) != 0. or abs(y[0])!=0.):
```

```
    x = x - x[iLE]
    y = y - y[iLE]
    cpx = cpx - cpx[iLE]
    cpy = cpy - cpy[iLE]
    theta = math.atan2(y[0],x[0])
    xd = x * math.cos(theta) + y * math.sin(theta)
    yd = -x * math.sin(theta) + y * math.cos(theta)
    x = xd
    y = yd
    cpx = copy(xd)
    cpy = copy(yd)
    iLE = x[30:-30].argmin()+30
    iTE = x.argmax()
        if iTE != 0:
                    x = append( x[iTE:] , x[2:iTE] )
                    y = append( y[iTE:] , y[2:iTE] )
                    cpx = append( cpx[iTE:] , cpx[2:iTE] )
                    cpy = append( cpy[iTE:] , cpy[2:iTE] )
                    cpp = append( cpp[iTE:] , cpp[2:iTE] )

# if using dimensional coordinates, extract chord and renormalize data
if (dimensions!="non"):
    chord = max(x)
    cpx = cpx/chord
    cpy = cpy/chord
    x = x/chord
    y = y/chord

# if chord is negative, it is the normal chord length rather than streamwise
if chord < 0:
    chord = abs(chord) / cos(sweep)
    y = y * cos(sweep)
    cpy = cpy * cos(sweep)

# correct for sweep if 2D calculation
if (normal):
    # correct Cp for compressible flow
    if correct :
        # Karman-Tsien
        mn = mach * cos(sweep)
        beta = sqrt( 1. - mn ** 2. )
        for i in range(0,len(cpp)):
            cpp[i] = cpp[i] / ( beta + (mn**2. / ( 1. + beta ) ) \
                        * cpp[i] / 2. )
    y = y*cos(sweep)
    cpp = cpp*cos(sweep)**2

#find stagnation point
iStag = cpp.argmax()

#calculate derivative and decide where key points are
```

```
dx = (x[1:]-x[:-1])
dy = (y[1:]-y[:-1])

dydx = dy/dx

# Find location where the slope equals 1 in roughly first half of the airfoil
pm = floor(len(x)/4)
(iStart,iSwitch) = nonzero(abs(dydx[iLE-pm:iLE+pm])>1)[0][[0,-1]]+iLE-pm

if (iStag < iStart):
    iStart = iStag - 20

if (iLE - iStart < 20):
    iStart = iLE - 20

# change to case directory and make necessary folders
os.chdir(casedir)
os.mkdir("crossflo")
os.mkdir("graph")
os.mkdir("sta")

# write out some files
f = open("../cp.dat","w")
for i in range(0,len(cpx)):
    f.write("%18.10e %18.10e %18.10e\n"%(cpx[i],cpp[i],0.))
f.close()
f = open("../xy.dat","w")
for i in range(0,len(x)):
    if(side=="suction"):
        f.write("%18.10e %18.10e %18.10e\n"%(x[i],y[i],0.))
    else:
        f.write("%18.10e %18.10e %18.10e\n"%(x[i],-y[i],0.))

f.close()

# get minimum cp value for use in plotting
cpmin = floor(cpp.min()*5.)/5.

#compute lift coefficient
cl = abs(integrate.trapz(cpp,cpx))

#reduce arrays
x=x[iStart:]
y=y[iStart:]

iLE = iLE - iStart
iSwitch = iSwitch - iStart + 2

#Find stagnation point and trim cp
ex = 1
```

```python
cpx=cpx[iStag-ex:]
cpy=cpy[iStag-ex:]
cpp=cpp[iStag-ex:]
iFirst=iStag - iStart + 1 - ex
iStag=ex
iCpMin = cpp[iStag:].argmin() + iStag + 1


# calculate sonic line
ma = fs["Mach number"]
scline = 2./(gamma*mach**2.)\
*(((1.+(gamma-1.)/2.*mach**2.)/(1.+(gamma-1.)/2.))**(gamma/(gamma-1.))-1.)
f=open("../scline.txt","w")
f.write("0. %18.10e\n"%scline)
f.write("1. %18.10e\n"%scline)
f.close()


# now, we'll cheat and correct it further using the isentropic attachment cp
if(fudge):
    ppinf = (1.-(gamma-1.)/2.*mach**2.\
      *(sin(sweep)**2.-1.))\
            **(gamma/(gamma-1.))
    cpisen = 2./(gamma*mach**2.)*(ppinf-1.)*0.99
    cp0 = cpp[iStag]
    for i in range(0,len(cpp)):
         if(cpp[i]>cpisen):
             cpp[i] = cpp[i] * cpisen / cp0


# Get version number and AoA from directory structure
if(inSrc=="path"):
    cwd = os.getcwd()

    if not "aoa" in locals():
        aoa = re.search('a[0-9]+',cwd)
        if (aoa):
            aoa = aoa.group()[1:]
            if(aoa[0]=='1'):
                aoa='-'+aoa[1]+'.'+aoa[2:]
            else:
                aoa=aoa[1] + '.' + aoa[2:]
            aoa = float(aoa)

    if not "modstr" in locals():
        modstrver = re.compile('modstr([0-9]{3})([0-9]+)')
        modstr = re.search('modstr[0-9]+',cwd)
        if (modstr):
            modstr = modstr.group()
            modstr = modstrver.sub('\\1.\\2',modstr)

    if (not buttline):
        buttline = re.search('bl[0-9]+',cwd)
        if (buttline):
```

```
            buttline=float(buttline.group()[2:])

    else:
        if not "aoa" in locals():
            aoa = None
        if not "modstr" in locals():
            modstr = None

    # write out geometry file
    f = open("geom.dat","w")
    f.write("4 /number of header lines\n")
    f.write("######\n")
    f.write("# %s (%s side)\n"%(xytitle,side))
    f.write("# x y\n")
    f.write("######\n")
    f.write("%18.10e   /chord\n"%chord)
    f.write("%18.10e   /sweepd\n"%sweepd)
    f.write("%18d  /ksplit\n"%iSwitch)
    for i in range(0,len(x)):
        f.write("%18.10e %18.10e\n"%(x[i],y[i]))
    f.close()

    # write out cp data file
    if modstr:
        print "modstr %s"%(modstr)
    if buttline:
        print "bl %0.1f"%buttline
    print "c %0.3f"%(chord)
    print "M %0.2f"%(mach)
    # first, decide what values to use for the conditions
    if(lastspec=="altitude"):
        altitude = fs["altitude in ft"]
        sigma,delta,theta = atmosphere(altitude*3.048e-4)
        pressure = delta * p0
        temperature = theta * t0
        rec = calcRecAlt(altitude,chord,fs)
        print "h %d"%(altitude)
    elif(lastspec=="recT"):
        rec=fs["chord Reynolds number"]
        temperature = fs["temperature"]
        M = fs["Mach number"]
        gamma = fs["gamma"]
        sc1 = fs["sc1"]
        sc2 = fs["sc2"]
        rgas = fs["rgas"]
        Uinf = M * sqrt( gamma * rgas * temperature )
        mu = sc1 * temperature*sqrt(temperature) / (temperature + sc2)
        density = rec * mu / ( Uinf * chord )
        pressure = density * rgas * temperature
    elif(lastspec=="pT"):
        pressure = fs["pressure"]
```

```python
        temperature = fs["temperature"]
        rec=calcRecPT(chord,fs)
    elif(lastspec=="findAlt"):
        altitude="altitude in ft"
        delta = 1.
        hA = 25000.0
        hB = 45000.0
        rec=fs["chord Reynolds number"]
        recA = calcRecAlt(hA,chord,fs)
        recB = calcRecAlt(hB,chord,fs)
        if((recA-rec)*(recB-rec)>0):
            error("target Rec is not in range 25000 - 45000 ft")
        max1 = int(1+round((log(hB-hA)-log(delta))/log(2.)))
        for k in range(1,max1):
            hC = (hA+hB)/2.
            recC = calcRecAlt(hC,chord,fs)
            if ( recC-rec==0):
                hA = hC
                hB = hC
            elif ((recB-rec)*(recC-rec)>0):
                hB = hC
                recB = recC
            else:
                hA = hC
                recA = recC
            if (hB-hA) < delta:
                exit
        altitude = round((hA+hB)/2.,-1)
        rec = calcRecAlt(altitude,chord,fs)
        sigma,delta,theta = atmosphere(altitude*3.048e-4)
        pressure = delta * p0
        temperature = theta * t0
        print "h = %d ft"%(altitude)
print "Rec %0.1fe6"%(rec/1e6)
print "C_l %0.3f"%cl
if aoa:
    print "AoA %0.3f"%(aoa)


f = open("edge.dat","w")
f.write("4 /number of header lines\n")
f.write("######\n")
f.write("# %s (%s side)\n"%(xytitle,side))
f.write("# x cp q\n")
f.write("######\n")
f.write("%18d   /ifirst\n"%iFirst)
f.write("%18d   /istag\n"%(iStag+1))
f.write("%18.10e   /rmref = post-shock reference mach number\n"%mach)
f.write("%18.10e   /pref = post-shock reference pressure\n"%(pressure) )
f.write("%18.10e   /tref = post-shock reference temperature\n"%(temperature) )
for i in range(0,len(cpx)):
    f.write("%18.10e %18.10e %18.10e\n"%(cpx[i],cpp[i],0.))
```

```
f.close()

shutil.copy(srcdir+"/doit.sh","..")

infile=open(srcdir+"/plot.gp","r")
outfile=open("../plot.gp","w")
title=""
if modstr:
    title=title+"%s"%(modstr)
if buttline:
    title=title+" BL %0.1f"%(buttline)
if modstr or buttline:
    title=title+"\\n"
title=title+"M = %0.3f"%(mach)
if aoa:
    title=title+" AoA = %0.3f"%(aoa)
title=title+" C_l = %0.3f"%(cl)
title=title+" Re_c = %0.2fx10^6"%(rec/1e6)

for s in infile:
    s = s.replace("CPMIN","%s"%(cpmin))
    s = s.replace("STRE",title)
    outfile.write(s)
infile.close()
outfile.close()

infile=open(srcdir+"/wingbl2.in","r")
outfile=open("wingbl2.in","w")
for s in infile:
    outfile.write(s.replace("NTRE","%d"%(iCpMin-1)))

infile=open(srcdir+"/lastrac.in","r")
outfile=open("lastrac.in","w")
for s in infile:
    outfile.write(s.replace("NTRE","%d"%(iCpMin-3)))
infile.close()
outfile.close()

infile=open(srcdir+"/lastrac-ts.in","r")
outfile=open("lastrac-ts.in","w")
for s in infile:
    outfile.write(s.replace("NTRE","%d"%(iCpMin-3)))
infile.close()
outfile.close()
```

C.1.2. *doit.sh*

```
#!/bin/bash

base=`pwd | sed '
s!/!!g
```

```
s/^.*\(mod.*\)$/\1/
'`


gnuplot -persist plot.gp
for side in suction pressure
do
name="${base}`echo $side | sed 's/\(.\).*/\1/'`"
echo $name
cd $side
wingbl2 < wingbl2.in > wingbl2.log
w2l mflow.dat $name
lastrac lastrac.in > lastrac.log 2>&1
ls -l nfact.dat
lastrac -t_ts lastrac-ts.in > lastrac-ts.log 2>&1
ls -l nfact_ts.dat
cd ..
done
```

C.1.3. *plot.gp*

```
p 'cp.dat' w l , 'scline.txt' w l , 'xy.dat' w l axes x1y2
set yrange [1.2:CPMIN]
set y2range [-0.1:0.7]
set xrange [0:1]
set xlabel "x/c"
set ylabel "C_p"
set title "STRE"
unset key
replot
set terminal postscript enhanced solid color
set output 'cp.ps'
replot
set terminal x11
set output
```

C.1.4. *wingbl2.in*

```
  1     /irun = 0 (edge data only); 1(profiles + edge data)
  1     /iblunt = 0 (sharp leading edge); 1 (blunt body)
  0     /iscale = 0 (scale lengths by L*); 1 (scale by delta*)
  0     /idiag = diagnostics trigger (0=off, 1=on, 2=lots)
 NTRE   /nsteps = number of steps in marching (xi) direction
  0     /dx = dimensional increment in x if > 0 (otherwise use input grid)
 62     /np = number of grid points in wall-normal (eta) direction
  0     /istart = start switch: 0 (fresh start); i > 0 (restart from i)
  3     /m = max. order of backward difference method [2 or 3 RECOMMENDED]
  1     /iread = edge data switch (1=Cp_e, 2=p_e, 3=u_e)
  0     /ismooth = divided difference smoothing in spline1 (1=yes,0=no)
  1     /iout = output stride for sta_xxxx files
 2.e-4 /rlim = maximum residual allowed   [KEEP DEFAULT 5.e-7]
  100   /itmax = iteration limit   [KEEP DEFAULT 20]
```

```
   0.7   /str = parameter of tanh stretching   [KEEP DEFAULT 0.7]
   40.   /eta_max = outer bound in wall-normal variable eta
   -.35  /ro = initial guess for F = 1 - exp(ro*eta)   [KEEP DEFAULT -.35]
   300.  /twall = dimensional wall temp. (Rankine--irrelevant for iadiab=1)
   1     /iadiab = wall boundary condition:  0 (isothermal); 1 (adiabatic)
   1     /massage = Cp_e data manipulation switch (0--off; 1--on)
   0.75  /factor = level above which to turn on Cp_e adjustment if massage = 1
         (recommend factor not less than 0.75)
```

C.1.5. *lastrac.in*

```
//
// LASTRAC LST for stationary crossflow
//

// mflow_filename = "mflow.dat"
nonl_pse_calc = false

grid_type = dual_cluster

relax_type = wall_temp

   num_normal_pts       = 101
// num_normal_pts_geig = 61
strm_order = second_order
wall_normal_order = fourth_order

// ymax = 8.
// ymax_glob_search = 8.
use_extrap_mprof = false

marching_method_2d  =  along_station
init_station        =  2
final_station       =  NTRE
// marching_method_2d  =  along_xc
// init_xc             =  .5
// final_xc            =  1.0
// step_xc             =  0.01

strm_curvt          =  false

solution_type       =  local_eig_solution

freq_unit           =  in_hertz_freq
beta_unit           =  in_mm_beta

freq = 15*0.
beta = 1.,2.,3.,4.,5.,6.,7.,8.,9.,10.,11.,12.,14.,16.,18.
wave_ang_min = 65, wave_ang_max = 99

qp_approx           =  true
```

```
// mflow_storage_type  = memory_storage
```

C.1.6. *lastrac-ts.in*

```
//
//  LASTRAC LST for streamwise instability
//

// mflow_filename = "mflow.dat"
nonl_pse_calc = false

grid_type = dual_cluster

relax_type = wall_temp

num_normal_pts       = 101
// num_normal_pts_geig = 61
strm_order = second_order
wall_normal_order = fourth_order

// ymax = 8.
// ymax_glob_search = 8.
use_extrap_mprof = false

marching_method_2d  =  along_station
init_station        =  2
final_station       =  NTRE
// marching_method_2d  =  along_xc
// init_xc             =  .5
// final_xc            =  1.0
// step_xc             =  0.01

strm_curvt          =  false

solution_type       = local_eig_solution

freq_unit           =  in_hertz_freq
beta_unit           =  non_dim_beta

freq =  0.333e3 , 0.667e3 , 1e3 , 1.333e3 , 1.667e3 , 2e3 , 2.333e3 ,
        2.667e3 , 3e3 , 3.333e3 , 3.667e3 , 4e3 , 6e3 , 8e3 , 10e3
beta = 15*0.

qp_approx           = true
// mflow_storage_type  = memory_storage
```

C.1.7. *Example freestream condition input file*

```
 0       / nhead
 1716.   / rgas
 2.27E-8 / reference sc1
```

129

```
198.6     / reference sc2
1.4       / reference gamma
0.72      / reference prandtl
0.75      / reference Mach number
535.39    / reference pressure
399.32    / reference temperature
34.59     / sweep angle in degrees
15.833    / chord length in ft
```

C.2. w2l.f90: Boundary-layer solver output to LASTRAC meanflow file

```fortran
program w2l

  implicit none

  integer :: k , n , iarg
  integer :: npts , n_station , istat , khead
  double precision , allocatable , dimension(:) :: eta , f , fp , fpp
  double precision , allocatable , dimension(:) :: y , u , v , w , t , p
  double precision :: x, rl, Rel, xcurvt, drdx , chord , u_e , t_e , rho_e , p0
  double precision :: ufs , prandtl , x0 , pfs , tfs , rhofs , rgas , gamma
  double precision :: delta , dol , minf , tmach , p_e , w_e , tv_e , tv
  double precision :: tmach_e , yy , muinf , s , h , f0 , f1 , f2 , disp , mome
  double precision :: reth1 , reth2 , reth3, sweepd, tinf , qinf , rhoinf , mu_e
  double precision :: sweep

  logical :: allocated = .false.

  integer , parameter :: inunit=16
  integer , parameter :: outunit=24

  character*16 , parameter :: legendfile = 'sta/legend'
  character*16 , parameter :: fsfile = 'freestream.d'
  character*8 , parameter :: prefix = 'sta/sta_'

  double precision :: null

  character*64 :: title , outfile , indir , infile
  integer , parameter :: igas = 1 ! perfect gas, 1 = yes
  integer , parameter :: iunit = 0 ! 1 = si, 0 = customary
  double precision , parameter :: nsp = 0 ! number of species
  double precision , parameter :: radius = 1 ! transverse cone radius

  double precision , parameter :: sc1 = 2.27e-8
  double precision , parameter :: sc2 = 198.6


  iarg = iargc()

  if(iarg.ne.2) then
```

```
  write(0,*) "usage: w2l [outfile] [title]"
    call exit(1)
  endif

  call getarg(1,outfile)
  call getarg(2,title)

  open(unit=inunit,file=fsfile,status='old',form='formatted')

  read(inunit,*) khead
  do k = 1 , khead
    read(inunit,*) !null
  end do

  read (inunit,*) rgas
  read (inunit,*) !sc1
  read (inunit,*) !sc2
  read (inunit,*) gamma
  read (inunit,*) prandtl
  read (inunit,*) minf
  read (inunit,*) pfs
  read (inunit,*) tinf
  read (inunit,*) sweepd
  read (inunit,*) !chord

  close(inunit)

  open(unit=inunit,file=legendfile,status='old',form='formatted')
  read(inunit,*)

  do while(.true.)
    read(inunit,*,end=10) n_station
  end do
10 close(inunit)

  ! calculate and write binary meanflow file
  open(unit=outunit,file=outfile,form='unformatted',status='replace')

  write(outunit) title
  write(outunit) n_station
  write(outunit) igas , iunit , prandtl , pfs , nsp


!  allocate(eta(npts),f(npts),fp(npts),fpp(npts),y(npts),u(npts),v(npts),&
!   w(npts),t(npts),p(npts))


  do n = 1 , n_station + 1
    istat = n - 1

    write(infile,'(A,I4.4)') prefix , n - 1
```
131

```
open(unit=inunit,file=infile,form='formatted',status='old')

read (inunit,*) ! npar
read (inunit,*) x
read (inunit,*) delta
read (inunit,*) dol !, phi

read (inunit,*) npts

if(.not.allocated) then
  allocate(y(npts),u(npts),v(npts),w(npts),p(npts),t(npts))
  allocated = .true.
end if

do k = 1 , npts
   read (inunit,*) y(k) !, q(k), v(k)
   read (inunit,*) t(k), u(k), w(k), v(k)
   read (inunit,*) !t1y(k), f1y(k), g1y(k), v1y(k),
   read (inunit,*) !t2y(k), f2y(k), g2y(k), v2y(k)
end do

read (inunit,*) !npar
read (inunit,*) !zeta
read (inunit,*) drdx
read (inunit,*) yy
read (inunit,*) !angled
read (inunit,*) !disp
read (inunit,*) !dol
read (inunit,*) !tmach
read (inunit,*) !umach
read (inunit,*) !wmach
read (inunit,*) !re1
read (inunit,*) !rex
read (inunit,*) Rel
read (inunit,*) !red
read (inunit,*) u_e
read (inunit,*) !vw
read (inunit,*) w_e
read (inunit,*) p_e
read (inunit,*) !redge
read (inunit,*) t_e
read (inunit,*) !tw
read (inunit,*) !evisc
read (inunit,*) !gamma
read (inunit,*) !pr
read (inunit,*) !sc1
read (inunit,*) !sc2
read (inunit,*) !rgas
read (inunit,*) !alpha
read (inunit,*) !beta
```

```
      read (inunit,*) !psid
      read (inunit,*) !rmax
      read (inunit,*) xcurvt

      close(inunit)

      ! reverse x/c if yy < 0
      ! if (yy<0) then
      !   drdx = -drdx
      ! end if

      rl = delta / dol
      rho_e = p_e / ( rgas * t_e )
      mu_e = sc1 * t_e*sqrt(t_e) / (t_e + sc2)
      sweep = sweepd * 3.14159265_8 / 180._8

      ! calculate leading-edge momentum thickness reynolds number
      muinf = sc1 * t_e*sqrt(tinf) / (tinf + sc2)
      rhoinf = pfs / ( rgas * tinf)

      if ( istat .eq. 0 ) then
        s = x
        ! method 1, pfenninger/potential

        qinf = minf * sqrt( gamma*rgas*tinf )
        reth1 = 0.404 * sqrt(qinf * sin(sweep) * tan(sweep) * rhoinf &
                           / ( xcurvt * muinf ))
        ! print * , qinf , sweep, rhoinf , xcurvt , muinf
        ! method 2: full-on integration
        disp = 0.
        mome = 0.
        do k = 1 , npts-1
          h = (y(k+1)-y(k))*rl
f0 = 1._8-t(k)**(-1._8) * w(k)
f1 = 1._8-t(k+1)**(-1._8) * w(k+1)
disp = disp + h/2._8 * (f0+f1)
f0 = t(k)**(-1._8) * w(k) * (1._8 - w(k))
f1 = t(k+1)**(-1._8) * w(k+1) * (1._8 - w(k+1))
mome = mome + h/2._8 * (f0+f1)
        end do
        reth2 = rhoinf * qinf * sin(sweep) * mome / muinf
      else if (istat .eq. 1 ) then
        s = x - s
        ! method 3: use "incompressible" definition from rosenhead
        mome = 0.404 * sqrt( mu_e * s / ( rho_e * u_e ))
        reth3 = rhoinf * qinf * sin(sweep) * mome / muinf
        write (*,'(A,4F12.4)') ' Re_theta ' , reth1 , reth2 , reth3 , 1/xcurvt
      end if

      if (istat .gt. 0) then
        w = w * w_e / u_e
```

```
    ! tv_e = tmach * sqrt(gamma * rgas * t_e)
    tv_e = sqrt(u(npts)**2._8+v(npts)**2._8+w(npts)**2._8) * u_e
    tmach_e = tv_e / sqrt(gamma * rgas * t_e)

    p0 = ( 1._8 + (gamma-1._8)/2._8 * tmach_e**2._8)**(gamma/(gamma-1._8)) &
         * p_e / (rho_e * u_e**2._8)
    do k = 1 , npts
      ! The pressure is constant in the BL approximation
      p(k) = p_e / (rho_e * u_e **2._8)
    end do

    write(outunit) istat, npts, x, rl, Rel, xcurvt, radius, drdx
    write(outunit) t_e, u_e, rho_e
    write(outunit) (y(k), k = 1, npts)
    write(outunit) (u(k), k = 1, npts)
    write(outunit) (v(k), k = 1, npts)
    write(outunit) (w(k), k = 1, npts)
    write(outunit) (t(k), k = 1, npts)
    write(outunit) (p(k), k = 1, npts)
    !print * , drdx , tmach_e
  end if
 end do

 close(outunit)

end program w2l
```

C.3. p3dtopoi.f90: Plot3D to TRANAIR POI format

```
! p3dtopoi: Converts Plot3D ASCII grid (.x) TRANAIR $POI file (.poi)
!           Reads from standard input and writes to standard output

! Note: Assumes BC condition = 1 and names networks using the sequence NET000

program p3dtopoi

  implicit none

  integer :: nmax, n , i , j , k

  integer, dimension(:), allocatable :: ni, nj, nk
  real, dimension(:,:,:), allocatable :: x , y , z

  integer , parameter :: bc = 1 ! assumes wall BC

  write(*,'(A4)') '$POI'

  read * , nmax
  write(*,'(F10.0)') float(nmax)
```

```
  write(*,'(F10.0)') float(bc)

  allocate(ni(nmax),nj(nmax),nk(nmax))

  read * , ( ( ni(n), nj(n), nk(n) ), n=1,nmax )

  do n = 1 , nmax

    allocate (x(ni(n),nj(n),nk(n)),y(ni(n),nj(n),nk(n)),z(ni(n),nj(n),nk(n)))

    read * , ( ( ( x(i,j,k), i=1,ni(n) ), j=1,nj(n) ), k=1,nk(n) ), &
             ( ( ( y(i,j,k), i=1,ni(n) ), j=1,nj(n) ), k=1,nk(n) ), &
             ( ( ( z(i,j,k), i=1,ni(n) ), j=1,nj(n) ), k=1,nk(n) )

    write(*,'(2F10.0,50X,A3,I0.3)') float(ni(n)), float(nj(n)), 'NET' , n

    do j = 1 , nj(n)
      write(*,'(6F10.4)') ((x(i,j,1),y(i,j,1),z(i,j,1)),i=1,ni(n))
    end do
    deallocate(x,y,z)

  end do

end program
```

C.4. poitop3d.f90: TRANAIR POI to Plot3D format

```
! poitop3d: Converts TRANAIR $POI file (.poi) to Plot3D ASCII grid (.x)
!           Reads from standard input and writes to standard output
!
! Note: This only works on a single $POI block; successive blocks are ignored
!       Comments or blank lines anywhere in the input are not supported
!       BCs and network names are discarded

program poitop3d

  implicit none

  interface
    subroutine resize3( a , ni , nj , nk)
      integer, intent(in) :: ni , nj , nk
      real , dimension(:,:,:) , allocatable , intent(inout) :: a
    end subroutine
  end interface

  integer :: nmax, n , i , j , k , bc
  real, dimension(8) :: tmp
  integer , dimension(:), allocatable :: ni , nj
  real, dimension(:,:,:), allocatable :: x , y , z
```

```fortran
    character(len=4) :: keyword
    character(len=10) :: netname

    read (*,'(A4)') keyword

    if(keyword /= '$POI') then
      write(0,*) 'error: first line of input missing $POI keyword'
      call exit(1)
    end if

    read (*,'(F10.0)') tmp(1)
    nmax = tmp(1)
    write(*,'(I10)') nmax

    allocate(ni(nmax),nj(nmax))

    read (*,'(F10.0)') tmp(1)
    bc = tmp(1)

    do n = 1 , nmax

      read (*,'(2F10.0,60X,A10)') , tmp(1), tmp(2) , netname
      ni(n) = int(tmp(1))
      nj(n) = int(tmp(2))
      write (*,'(3I10)') ni(n) , nj(n) , 1

      call resize3(x,ni(n),nj(n),nmax)
      call resize3(y,ni(n),nj(n),nmax)
      call resize3(z,ni(n),nj(n),nmax)

      do j = 1 , nj(n)
        read(*,'(6F10.0)') ((x(i,j,n),y(i,j,n),z(i,j,n)),i=1,ni(n))
      end do

    end do

    do n = 1 , nmax
      write(*,'(6F10.4)') ( ( x(i,j,n), i=1,ni(n) ), j=1,nj(n) ), &
                          ( ( y(i,j,n), i=1,ni(n) ), j=1,nj(n) ), &
                          ( ( z(i,j,n), i=1,ni(n) ), j=1,nj(n) )
    end do

end program

! resize3: allocates or reallocates array a(ni,nj,nl), preserving contents
subroutine resize3( a , ni , nj , nk)

  implicit none

  integer, intent(in) :: ni , nj , nk
  real , dimension(:,:,:) , allocatable , intent(inout) :: a
```

```
    integer :: i , j , k , ni0 , nj0 , nk0
    real , dimension(:,:,:) , allocatable :: b

    if (.not.allocated(a)) then
      allocate(a(ni,nj,nk))
    else
      ni0 = size(a,1)
      nj0 = size(a,2)
      nk0 = size(a,3)
      if(ni.gt.ni0 .or. nj.gt.nj0 .or. nk.gt.nk0) then
        allocate(b(ni0,nj0,nk0))
        b = a
        deallocate(a)
        allocate(a(max(ni,ni0),max(nj,nj0),max(nk,nk0)))
        a(1:ni0,1:nj0,1:nk0) = b
        deallocate(b)
        endif
    endif

    return

end subroutine
```